

UNIVERSITÀ DEGLI STUDI DI PADOVA

DIPARTIMENTO DI FISICA E ASTRONOMIA “G.GALILEI”
MASTER DEGREE IN ASTROPHYSICS AND COSMOLOGY

FINAL DISSERTATION

THE ORBITAL GEOMETRY OF THE HOT JUPITER HD 189733B: NEW RESULTS FROM THE ROSSITER-McLAUGHLIN REVOLUTIONS

THESIS SUPERVISOR
PROF. LUCA MALAVOLTA

MASTER CANDIDATE
DAVIDE SAVIO

ACADEMIC YEAR
2022-2023

“À MIA MADRE,
CHE DA SEMPRE CREDE IN ME.”

Abstract

Among the increasing number of discovered exoplanets, the ones that transit their host star are of great interest, because they can be analysed with both photometric and spectroscopic methods. The combination of the information obtained from the light curve, which is related to the planet radius, and from the radial velocity curve, which instead is related to the mass of the planet, allows the determination of the bulk density of the exoplanet. Another important aspect in analysing a transiting planet with the spectroscopic technique is the possibility to observe the Rossiter-McLaughlin (RM) effect, i.e., the radial velocity anomaly caused by the planet as it transits across the disc of its host star. The RM waveform is sensitive to the local properties of the star occulted by the transit chord, as a consequence it allows the measurement of the star-planet orbital alignment. In particular, the angle ψ between the orbital axis of a planet and the spin axis of its host star is of fundamental importance to constrain theories on planet formation, orbital migration and tidal evolution. As an example, planets in aligned orbits are the result of dynamically gentle migrations, while misaligned planets could have experienced violent migration processes such as planet-planet or star-planet scattering through the Kozai-Lidov mechanism. It is therefore of great importance to measure this angle as a function of stellar parameters, age, and planetary multiplicity. The classical RM effect allows the measurement of the sky projections of the stellar spin and the orbital plane, called λ , and the true obliquity ψ can be determined only through strong assumptions. In this Master Thesis I present a new implementation of the revolutionary method proposed by Cegla et al. 2016 in which the geometry of the planetary system is derived by modelling the occulted regions of the star through cross-correlation analysis of the spectra rather than the apparent radial velocity change due to the spectral deformation. With the so-called Reloaded Rossiter-McLaughlin (RRM) technique, I am able to measure the true 3D spin-orbit geometry of the star-planet system although the $v_{eq} \sin i_*$ degeneracy is still present. In the modelling, I have also included differential stellar rotation and centre-to-limb convective variations, while making no assumptions on the shape of the intrinsic stellar photospheric lines. I have also implemented the recent improvement proposed by Bourrier et al. 2021, dubbed Rossiter-McLaughlin effect Revolutions (RMR), so that I can now exploit the full extent of information contained in spectral transit time series by modelling simultaneously all the in-transit cross correlation functions through a Bayesian approach, enabling the measurement of the spin-orbit angle of small exoplanets even when the classical RM signal is not detectable. I have then focused my attention to HD189733b, a Jupiter-like exoplanet with a period of 2.2 days orbiting a K2 star. Due to the brightness of its host star (magnitude $V=7.6$) and the extreme conditions undergoing on its outer layer, this exoplanet is a golden target for exoplanetary atmosphere studies, which in turn relies on accurate characterization of the planetary and orbital characteristics. After validating

the mathematical framework and the data analysis steps of my implementation of the RRM and the RMR techniques by comparing my results with those already published on publicly available HARPS data, I have performed a combined modelling of photometric data spanning over fifteen years, high precision radial velocity data from the literature, and eight in-transit spectroscopic time series, in a robust and reliable Bayesian framework. Most notably, I have used data coming from two sectors of TESS to obtain the most precise radius measurement of this planet so far, and unpublished spectroscopic time series over four nights of observations obtained in the context of the Global Architecture for Planetary Systems (GAPS) program using the ultra-stable HARPS-N spectrograph at the Telescopio Nazionale Galileo.

The work I performed has produced the most accurate self-consistent set of planetary parameters among those reported in the literature for HD189733b, including a new determination of the spin-orbit angle for this planetary system. With the code publicly available, I have now the possibility to extend this kind of analysis to many other exoplanets with in-transit spectroscopic observations but still lacking a characterization of the 3D spin-orbit geometry of the star-planet system, making this thesis on HD189733b the first of a long series of groundbreaking works.

Sommario

Tra il crescente numero di esopianeti scoperti, quelli che transitano la loro stella ospite sono di grande interesse, in quanto possono essere analizzati sia tramite il metodo fotometrico che tramite quello spettroscopico. Combinando l'informazione ottenuta dalla curva di luce, legata al raggio del pianeta, con quella ottenuta dalla curva di velocità, che dipende invece alla massa del pianeta, è possibile determinare la densità apparente del pianeta. Un altro importante aspetto nell'analizzare con la tecnica spettroscopica un pianeta che transita risiede nella possibilità di osservare l'effetto di Rossiter-McLaughlin (RM), ovvero, l'anomalia nella velocità radiale causata dal pianeta mentre transita da una parte all'altra del disco della sua stella ospite. La forma d'onda dell'effetto RM è sensibile alle proprietà locali della stella che viene occultata della corda del transito e di conseguenza permette di misurare l'allineamento stella-pianeta. Nello specifico, l'angolo ψ compreso tra l'asse del piano orbitale del pianeta e l'asse di rotazione della sua stella ospite è di fondamentale importanza per poter imporre dei vincoli alle teorie di formazione planetaria, migrazione delle orbite ed evoluzione mareale. A titolo d'esempio, i pianeti in orbite allineate sono il risultato di migrazioni dinamicamente tranquille, mentre i pianeti disallineati potrebbero aver subito processi di migrazione turbolenti come nel caso dello sparpagliamento pianeta-pianeta o pianeta-stella tramite il meccanismo di Kozai-Lidov. E' dunque di fondamentale importanza misurare quest'angolo in funzione dei parametri stellari, dell'età e della molteplicità planetaria. L'effetto RM classico permette di misurare la proiezione in cielo degli assi di rotazione stellare e del piano orbitale, chiamata λ , mentre l'obliquità vera ψ può essere determinata solo tramite forti assunzioni. In questa Tesi Magistrale presento una nuova implementazione del metodo rivoluzionario proposto da Cegla et al. 2016 in cui la geometria del sistema planetario è derivata modellando le regioni della stella occultate dal pianeta tramite l'analisi di correlazione incrociata degli spettri, anziché il cambiamento apparente in velocità radiale a causa della deformazione dello spettro. Con la tecnica chiamata Reloaded Rossiter-McLaughlin (RRM), sono in grado di misurare la vera geometria 3D spin-orbita del sistema stella-pianeta sebbene rimanga la degenerazione $v_{eq} \sin i_*$. Nel modello ho incluso anche la rotazione differenziale della stella e la variazione convettiva dal centro al bordo, senza fare assunzioni sulla forma delle linee fotosferiche stellari intrinseche. Ho anche implementato il recente miglioramento proposto da Bourrier et al. 2021, soprannominato effetto Rossiter-McLaughlin Revolutions (RMR), così che possa ora sfruttare nella loro interezza le informazioni contenute nella serie temporale di spettri del transito, modellando simultaneamente tutte le funzioni di correlazione incrociata durante il transito con un approccio Bayesiano, rendendo possibile la misura dell'angolo di spin-orbita degli esopianeti piccoli, anche nei casi in cui il segnale RM classico non sia rilevabile. Ho concentrato la mia attenzione su HD189733b, un esopianeta simile a Giove con un periodo di rivoluzione di 2.2 giorni in orbita attorno ad una

stella K2. A causa della luminosità della sua stella ospite (magnitudine $V=7.6$) e le condizioni estreme in atto nel suo strato più esterno, questo pianeta è un obiettivo d'oro per gli studi sulle atmosfere planetarie, che a loro volta fanno affidamento su di una accurata caratterizzazione delle caratteristiche planetarie e orbitali. Dopo aver validato il quadro matematico e gli step di analisi dei dati della mia implementazione delle tecniche del RRM e del RMR, facendo un confronto dei miei risultati con quelli già pubblicati relativi ai dati HARPS ad accesso pubblico, ho eseguito un modello combinato di dati fotometrici che ricoprono un arco di tempo di oltre 15 anni, misure ad alta precisione di velocità radiale prese dalla letteratura ed 8 serie temporali spettroscopiche in transito, in un contesto Bayesiano robusto ed affidabile. In particolare, ho utilizzato dati provenienti da due settori di TESS, per ottenere la misura ad oggi più precisa del raggio di questo pianeta e serie temporali spettroscopiche non pubblicate, divise in quattro notti di osservazioni ottenute nel contesto del programma dell'Architettura Globale per i Sistemi Planetari (GASP) utilizzando lo spettrografo ultra-stabile HARPS-N al Telescopio Nazionale Galileo.

Il lavoro che ho eseguito ha prodotto il set di parametri planetari più accurato ed auto-consistente tra tutti quelli riportati in letteratura per HD189733b, inclusa una nuova determinazione dell'angolo spin-orbita per questo sistema planetario. Con il codice pubblicamente disponibile, ho adesso la possibilità di estendere questo tipo di analisi a molti altri esopianeti con osservazioni spettroscopiche in transito, ma ancora privi di una caratterizzazione della geometria 3D spin-orbita del sistema stella-pianeta, così che questa tesi relativa ad HD189733b risulti il primo di una lunga serie di lavori innovativi.

Contents

ABSTRACT	v
SOMMARIO	vi
1 INTRODUCTION	1
1.1 The effect explained	3
1.2 The classical Rossiter-McLaughlin effect	3
1.3 The Reloaded Rossiter-McLaughlin effect	4
1.4 The Rossiter-McLaughlin effect Revolutions	5
2 THE RELOADED ROSSITER-McLAUGHLIN TECHNIQUE	7
2.1 The code for the RRM	8
3 THE ROSSITER-McLAUGHLIN EFFECT REVOLUTIONS TECHNIQUE	25
3.1 The code for the RMR	25
3.1.1 Individual exposures fitting	27
3.1.2 Global Transit analysis	32
4 DATASET	39
4.1 HARPS observational data	39
4.2 New HARPS-N data	40
4.3 TESS data	41
4.3.1 TESS analysis	42
4.4 Literature radial velocity data	46
4.4.1 Literature radial velocity analysis	47
4.5 Literature light curve data	50
4.5.1 Literature light curve analysis	51
4.6 Limb Darkening coefficients	55
4.7 Modelling with PyORBIT	56
5 RESULTS	59
5.1 Standard Rossiter-McLaughlin	59
5.2 Reloaded and Revolutions first analysis	61
5.3 Reloaded and Revolutions second analysis	66
5.4 Comparison of the results	71

6 CONCLUSION	75
REFERENCES	79

1

Introduction

After the discovery of 51 Peg-b by Mayor & Queloz in 1995, the Exoplanetary Science has entered a still going flourishing age, during which, thanks also to the interest of the public, many efforts and investments have been dedicated to this research, and different astrophysical fields have also been involved in making Exoplanetary Astrophysics the prolific science it is nowadays. In a time span of almost three decades since the discovery of the first exoplanet, many other planets orbiting around a star different from the Sun have been detected, so that it is now possible to study a significant number of exoplanets and systems of exoplanets. This has been made possible thanks to the improvement of the multiple techniques of detection as well as the development of new space and ground based telescopes intended for this kind of research. Among the different detection methods, the photometric technique of the transit has proven to be the most rewarding one, contributing with about 4000 discovered planets to the total of 5438 confirmed exoplanets, followed by the spectroscopic technique of the radial velocity (RV), which led to the discovery of more than 1000 planets.¹ These two techniques are complementary to each other, since from the light curve of the transits it is possible to measure the radius and from the radial velocity curve the mass of the planet; once these two physical quantities are both known for a given planet, as it happens in the cases in which the host star is bright, so that the spectroscopic analysis can be applied, than it is also possible to determine its bulk density. A planet that transits a bright rotating star, obscures regions of the stellar sur-

¹<https://exoplanetarchive.ipac.caltech.edu/>

face from the view causing a deviation from the Doppler reflex motion that it imparts on the host. As a consequence, during the transit across the stellar disc, the spectral lines are distorted and the result is an anomalous deviation of their line-of-sight (LOS) velocities centroid from the Keplerian curve. This anomalous spectroscopic signal is known as Rossiter-McLaughlin (RM) effect² and it has a shape that contains information about the ratio of the sizes between the planet and its host star, the impact parameter, the rotational speed of the star and the angle λ which is the sky-projected spin-orbit angle i.e., the projection onto the plane of the sky of the angle between the normal to the orbital plane of the planet and the rotation axis of the star. The first reported Rossiter-McLaughlin effect for an exoplanet was that of HD209458 b, by Queloz and collaborators in 2000 and after that, determining λ has become one of the steps to characterise the orbital geometry of planetary systems.[1] Measuring the spin-orbit angle is fundamental to improving theories on the planetary formation, evolution and migration for a variety of systems. According to the model of disk-driven migration, the alignment between angular momentum of proto-planetary disk and planetary orbits should be conserved. Nonetheless, exoplanets show a large diversity in value of λ as for the other physical quantities. There are many formation and migration mechanisms that can lead to a misalignment between the spin of the star and the axis of the planetary orbit: a primordial tilt of the star or the disk, a tidal torque on the disk from a close star, a tidal torque on the inner planets from an outer companion and scattering or secular interactions between inner planets and outer planetary or stellar companion.[2] Therefore, determining the mutual inclinations between the planets and with the host star, and analyzing the distribution of λ with other parameters can allow to distinguish among the different scenarios.[2] For the cases in which the RV precision is too poor to measure the mass, the RM effect can be used to confirm that an object is a planet, excluding companion stars and brown dwarfs.[1] It can also be applied in other cases, to measure the orbital inclination of eclipsing binaries, or to determine the direction of the rotational spin of the exoplanets, and it can provide information about the atmospheric composition of the planets and also about exo-moons.[1] In all of these cases, a correct modelling of the RM waveform is necessary.

²The name of this effect comes from the papers published jointly by Rossiter and McLaughlin in 1924, although it had already been theorised much earlier by Holt in 1893 and Schlesinger had correctly interpreted in 1910 the discrepant radial-velocities obtained during an eclipse.[1]

1.1 THE EFFECT EXPLAINED

When a star rotates, one of its hemispheres moves toward the observer and the other hemisphere moves away from the observer. Considering the LOS component of the stellar rotation, the approaching hemisphere appears blue-shifted, while the receding one appears red-shifted. If a planet transits this star, then it will sequentially cover different portions of the stellar disc during its transit. While the planet obscures the blue-shifted side of the star, the average value of the flux received by the observer appears offset toward the red, so that the net result is a positive shift in the measured RV of the star; the opposite happens when the red-shifted hemisphere is obscured, but in both cases there is a deviation from the Doppler reflex motion.[3] Considering the stellar velocity profile, the star appears to be rapidly changing its rotation speed while the planet moves in front of its disc: this is the Rossiter–McLaughlin effect. From the shape of the RM effect is possible to obtain several information, like the time the planet has spent crossing one hemisphere and the other, from which is possible to get the projected angle between the path of the planet and the equator of the star. To a first order, the semi-amplitude of the RM effect scales with the planet’s size and the stellar rotational velocity:

$$A_{RM} \simeq \frac{2}{3} D v \sin i_* \sqrt{1 - b^2} \quad (1.1)$$

where b is the impact parameter, $\sin i_*$ is the sky projected inclination of the stellar spin axis, v is the equatorial rotational velocity of the star and $D = (R_p/R_*)^2$ is the transit depth, relating the radius of the planet to that of the host star.[1] The event has the same duration as the transit, which is 2-3 hours in the case of an Hot Jupiter. In order to detect the RM signal, the requirements are high-cadence RV measurements obtained with stable spectrographs able to guarantee high precision and high resolution.

1.2 THE CLASSICAL ROSSITER-McLAUGHLIN EFFECT

The first attempts to model the RM effect were made by Petrie back in 1938, who referred to it as rotation effect and by Kopal in 1942, who gave formulations which were only valid in the case of coplanar systems.[1] Hosokawa generalized these calculations in 1953, introducing the sky-projected spin–orbit angle and Kopal compiled a complete description between 1959 and 1979 using α -functions, based on Legendre polynomials to integrate over the visible surface of the stars.[1] Adjustment to the model were made by Queloz and collaborators on the first

RM effect detection in 2000, by drawing a grid over the star and reconstructing the cross correlation function of its spectrum from which the radial-velocity was extracted.[1] This approach based on the grid has been adopted by other authors, because it allows to treat various stellar effect, such as variability due to the motion of the spots and the overlap of spots by transiting planets. The most used notation for the spin-orbit angle is λ and has been introduced by Ohta and collaborators in 2005 in a paper where they presented an analytical expression for the RM effect.[1] This formalism has been improved in 2011 by Hirano and in 2013 by Boué, by solving the issues related to the different methods of RV extraction from the stellar spectra that could affect amplitude and shape of the RM effect.[1] Another correction that can be applied is that proposed in 2011 by Shporer and Brown, that takes into account the small bias that is introduced in the angle λ if the stellar convective blue-shift is ignored.[3]

The traditional way of modelling the RM effect is through a radial-velocity time-series. The information contained in the RV comes from distorted stellar absorption lines, that are caused by a reduction on the flux coming from the blue or red-shifted hemisphere. Detecting temporal variations in the shape of a single line by a transiting planet is complicated, yet Albrecht and collaborators were able to do it for some eclipsing binaries in 2007.[1]

1.3 THE RELOADED ROSSITER–MCLAUGHLIN EFFECT

In the contest of a planetary transit, different points of the stellar disc are sequentially obscured by the planet causing the anomalous signal in the stellar RV curve that is known as RM effect. The classical method to study this effect is that of modelling the apparent radial velocity change due to the spectral deformation, but this can be challenging. An alternative and more efficient method is that of the Reloaded Rossiter-McLaughlin effect (RRM), proposed by Cegla and collaborators in 2016[3], according to which the RM effect is studied over thousands of stellar lines, through cross-correlation analysis. The RRM method relies on the reconstruction of the velocity field that the planet obscures during the transit, using the cross correlation functions (CCF). This technique allows to isolate the starlight from the obscured regions by subtracting in-transit spectroscopic observations from those taken out-of-transit, similarly to what is done in line profile tomography, but it analyses directly the local CCF occulted by the planet without the assumption of a particular function in order to model its impact on the disc-integrated CCF.[3] The RVs of the planet-occulted regions are then obtained from the centroids of the average stellar line contained in each CCF_{loc} .

A correct modelling of the RM waveform is extremely important, still many of the classical ap-

proaches ignore any velocity source emanating from the surface of the star and simply assume a rigid body rotation, in contrast to the models of stellar photospheres. The RRM approach accounts for the convective blue-shift and its centre to limb variation and takes into account the latitudinal differential rotation α . According to Cegla and collaborators, accounting for α allows to lift the degeneracy between the equatorial velocity v_{eq} and the stellar inclination i_* , because the transit is then sensitive to the stellar latitudes that are covered by the planet and this allows to directly measure the stellar inclination [3]. If the $v_{eq} \sin i_*$ degeneracy can be lifted, it is possible to measure the true spin-orbit angle ψ , which describes the three-dimensional geometry of the star-planet system and removes the biases introduced by using its projection on the sky λ .

1.4 THE ROSSITER–MCLAUGHLIN EFFECT REVOLUTIONS

The reloaded RM technique isolates the local CCFs (CCF_{loc}) from the regions of the stellar photosphere that are occulted by a planet during its transit. The RVs are obtained from the CCF_{loc} and are then fitted with a realistic model that gives constraints on the stellar surface velocity field and orbital architecture of the system. [2] This approach is based on the possibility to detect and fit with a χ^2 minimization method the average stellar line of individual CCF_{loc} . In many cases in which the host star is too faint, the stellar line is too shallow, or the transit depth is too small, and in the low-flux CCF_{loc} at the limbs of the star, which are darker at optical wavelengths and only partially occulted by the planet, the RRM method can not be applied. [2] This restricts the range of small planets for which the RRM technique can determine the orbital geometry to the cases in which they transit bright stars only. A new approach to analyze the RM effect has been proposed by Bourrier and collaborators in 2021 [2] with the purpose to overcome these limitations: the RM effect Revolutions (RMR) method. As in the traditional RRM approach, the starting point is the extraction of CCFs that are occulted by the planet, but rather than working with CCF_{loc} , in the RMR method the flux of the continuum of the CCF is normalized to unity, rather than to the flux value of the occulted regions. The intrinsic CCF obtained in this way are independent of planetary occultation and of limb-darkening effect and trace the variation in the profiles of the local stellar line, thus allowing for a more direct comparison. In the RRM method, each CCF_{loc} is fitted with a Gaussian line model using a Levenberg-Marquardt least-squares minimization. This approach is limited by the possibility to detect the stellar line and it depends on an arbitrary threshold, calculated using the fit properties, to establish if the local stellar line is detected and the values obtained from the best-fit can

be used for the analysis. If systematic errors are present in the data, with the χ^2 minimization it is difficult to determine whether the model has been fitted to a stellar line or to a spurious feature. Moreover, if the stellar line model properties are not following a Gaussian distribution, the χ^2 minimization can introduce a bias in the best-fit values and errors. In the RMR method, the analysis of the planet-occulted CCFs is improved thanks to the Bayesian approach. In each exposure, a model of the stellar line is fitted to the intrinsic CCF sampling the posterior distributions of the parameters with a Markov Chain Monte Carlo (MCMC) method and permitting a variety of priors. The targets for which this method has been introduced have a small S/N and this implies that the stellar line properties are poorly constrained in individual exposures. To get over this problem, the main novelty of the RMR approach is that of fitting all the intrinsic CCFs together with a joint model, where the shape parameters of the CCF are shared among the observations, instead of fitting them one by one, with independent sets of parameters.[2] There are different analytical models that can be used to describe the stellar line profile with properties that can be kept constant in all exposures or be set by parametric models as a function of time. The RV centroids of the theoretical lines are set by a surface RV model that takes into account for the projected rotation velocity field of the star and for its blur over the region covered by the planet at a given epoch, evaluating also the contribution of the convective blueshift and of the differential rotation. The time series of the theoretical stellar lines is convolved with the response of the instrument and fitted to all the intrinsic CCFs together using the MCMC. If the stellar line is modelled before convolution, it is possible to have a more direct comparison between different instruments.[2] The RMR technique allows to amplify the S/N of the occulted stellar line, at first order by the number of in-transit exposures and this increases the possibility of determining the path of the planet even in the cases in which the line can not be detected in individual exposures. Differently from the traditional RRM method, the RMR approach exploits all the temporal and spectral information contained in the data, in order to derive the properties of the stellar surface and the orbital architecture with a higher precision, as it fits the stellar line profiles and not just their centroids.[2]

2

The Reloaded Rossiter-McLaughlin technique

In this chapter I provide a complete description of the Reloaded Rossiter-McLaughlin (RRM) technique. For this part of my work I had to build the mathematical framework and the various steps required for the data handling and the data analysis, with the specific purpose of reproducing the results of Cegla et al. 2016 on HD189733[3] using HARPS data reported in Table 2.1.

Table 2.1: HARPS data on HD189733

Night	Spectra	In-transit	Pre/post	Mask	t_{exp} [s]	Airmass
2006-07-29	12	6	0/6	K5	~ 600	1.62 – 1.86
2006-09-07	20	11	3/6	K5	$\sim 600^1$	1.62 – 2.05
2007-07-19	39	19	0/20	G2	~ 300	1.62 – 2.49
2007-08-28	40	20	7/13	G2	~ 300	1.62 – 2.28

¹During this night of observations, two longer exposures of 900 s have been carried out, one before and one after the transit, due to the poor weather conditions.

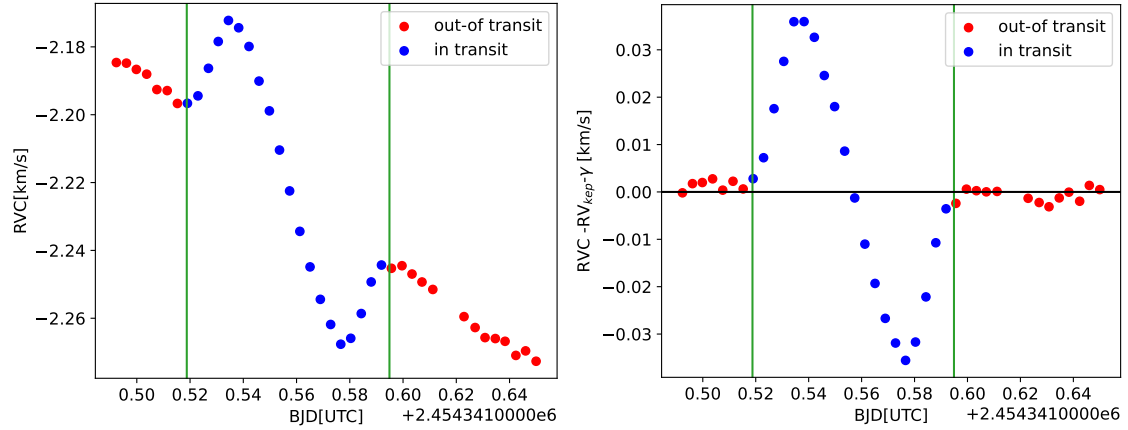
Table 2.2: Literature values for HD189733 taken from Cegla et al. 2016[3]

Parameter	Value
T_0	$2454279.436714 \pm 0.000015$ d
P	$2.21857567 \pm 0.00000015$ d
i_p	$85.710 \pm 0.024^\circ$
R_\star	$0.805 \pm 0.016 R_\odot$
R_p	$0.15667 \pm 0.00012 R_\star$
a/R_\star	8.863 ± 0.020
T_{tr}	1.827 h
K	200.56 ± 0.88 m s ⁻¹
e	0
ω	90°
u_1	0.816 ± 0.019
u_2	0

2.1 THE CODE FOR THE RRM

Since Cegla and collaborators have not released their code to compute the Reloaded Rossiter-McLaughlin effect, in order to reproduce the results reported in their paper I had to follow the description that they have provided in the method’s section and write a code that performs the same kind of calculations and analysis. In its very first part, my code selects the cross correlation functions (hereafter CCFs), as computed by the Data Reduction Software provided by the builder of the instrument.² In the case of HARPS, the CCF as stored as file `.fits`, with the identifier suffix `_ccf_[template_name]`, where `template_name` is the file name of the correlation mask used to compute it. Each of them is a matrix made of n_{order} CCF spectrum that corresponds to the CCF computed for each order.² Among the multiple information that are reported in the header of the CCFs, I took the values of the time of the observation in BJD, the total exposure time in seconds, the barycenter drift corrected RV in km/s, the value of the reference pixel, the Full Width at Half Maximum (FWHM) of the CCF, reported in km/s, and the data of each of the CCFs and stores them keeping the separation based on the night of the observation. Starting from the literature values of the time of conjunction and orbital period, reported in Table 2.2, my code computes the time of ingress, conjunction and egress for each night of observation and uses these values to distinguish between in-transit and out-of-transit CCFs. An example of the output of this analysis is visualized in Figure 2.1a, where

²<https://www.eso.org/sci/facilities/lasilla/instruments/harps/doc.html>



(a) Example of how the raw data of one night are visualized (b) Residual of the keplerian and system velocities subtraction.

Figure 2.1: This plots show how data are visualized before and after the subtraction of the keplerian and system velocity. In particular, in Figure 2.1a the drift corrected radial velocities are plotted as a function of the time of the observation and different colors are used to identify in-transit CCFs (blue) and out-of-transit CCFs (red). The vertical lines correspond to the time of ingress (also called first contact, or T1) and egress (fourth contact, T4) and they temporally collocate the transit during that specific night. The trend that the blue points follow is due to the RM effect. Figure 2.1b shows for the same night the residual signal left after the modelled keplerian velocity and the system velocity γ have been subtracted from the drift corrected RV. The horizontal black line indicates where the point should dispose in absence of the RM effect (no transit).

I plotted the drift corrected RV (RVC) as a function of the time of the observation for one of the nights, using different colors for the in-transit and out-of-transit CCFs. From this plot is already possible to recognise the signal of the RM effect.

After this selection, I performed a modelling of the RV curve with a sinusoidal function defined as:

$$RV_{kepler} = -K \sin(2\pi\varphi), \quad (2.1)$$

where K is the semi-amplitude in km/s which value, taken from literature, is reported in Table 2.2, and φ is the orbital phase, computed as:

$$\varphi = \frac{(T - T_C)}{P}, \quad (2.2)$$

where T is the time of the observation, T_C is the time of conjunction of that night and P is the orbital period of the planet, also taken from literature and reported in Table 2.2. This model describes the RV curve of a star that is performing a keplerian motion around the barycentric position due to the presence of a planet, hence the name RV_{kepler} . When the observed RV curve is compared with the modelled RV_{kepler} , there is no difference between them out of the transit,

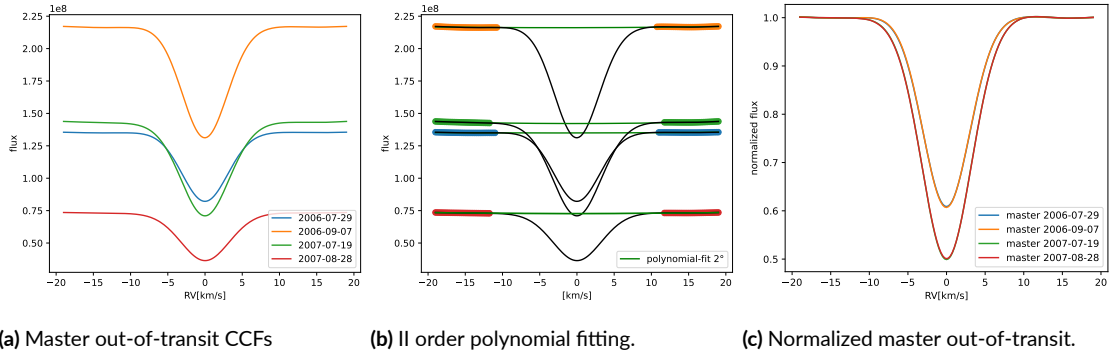


Figure 2.2: These plots display the steps that are performed by the program. Figure 2.2a shows the master-out-of-transit CCFs, obtained by co-adding the out-of-transit CCFs of each night. Figure 2.2b shows the selection of the flat part, excluding the points in the interval $\pm 1.5 \cdot \overline{FWHM}$ from the center and the fitting with a second order polynomial on it. Figure 2.2c shows the normalized master-out-of-transit; they have different contrast depths because they are obtained with the two different masks K5 and G2.

while there is a clear residual RV signal during the transit, that corresponds to the RM effect. The plot of Figure 2.1b displays an example of this residual RM signal. Practically speaking, in the out-of-transit CCFs the drift corrected radial velocity signal (RVC) is given by the sum of the keplerian and system velocity, while in the in-transit CCFs a third component is also present, which is the RM anomaly. To obtain the value of the system velocity γ , I computed the mean of the difference between the observed out-of-transit RVC and the modelled RV_{kepler} . The computed values of γ and the RV_{kepler} are then used to perform a rebinning, so that each CCF is now aligned in the stellar reference frame (central position of CCF with a RV value of 0 km/s). For the rebinning, my code takes a subroutine dedicated to this purpose, that works with a cubic interpolation and conserves the flux inside of each bin. This is a fundamental step that I had to do before to proceed any other analysis, because I then computed the master-out-of-transit CCFs (see Figure 2.2a), by co-adding the out-of-transit CCFs of each night, which must be aligned in the stellar reference frame to be sure that the signal that enters the sum comes from the same region of the surface of the star for each of them. At this point, I selected the flat part of the master-out-of-transit CCFs. In order to use the same interval of points in all of them, I have determined first the mean values of the FWHM of each night, then the mean of these values, \overline{FWHM} , and selected the flat part by excluding all the points that are closer than $\pm 1.5 \cdot \overline{FWHM}$ to the center. I then fitted the flat part using a second order polynomial (see Figure 2.2b). Finally, I have normalized the master-out-of-transit CCFs, dividing them by the values obtained from the fitting (see Figure 2.2c). I note that some observation have been taken with different masks, as the data was gathered by independent research groups using different

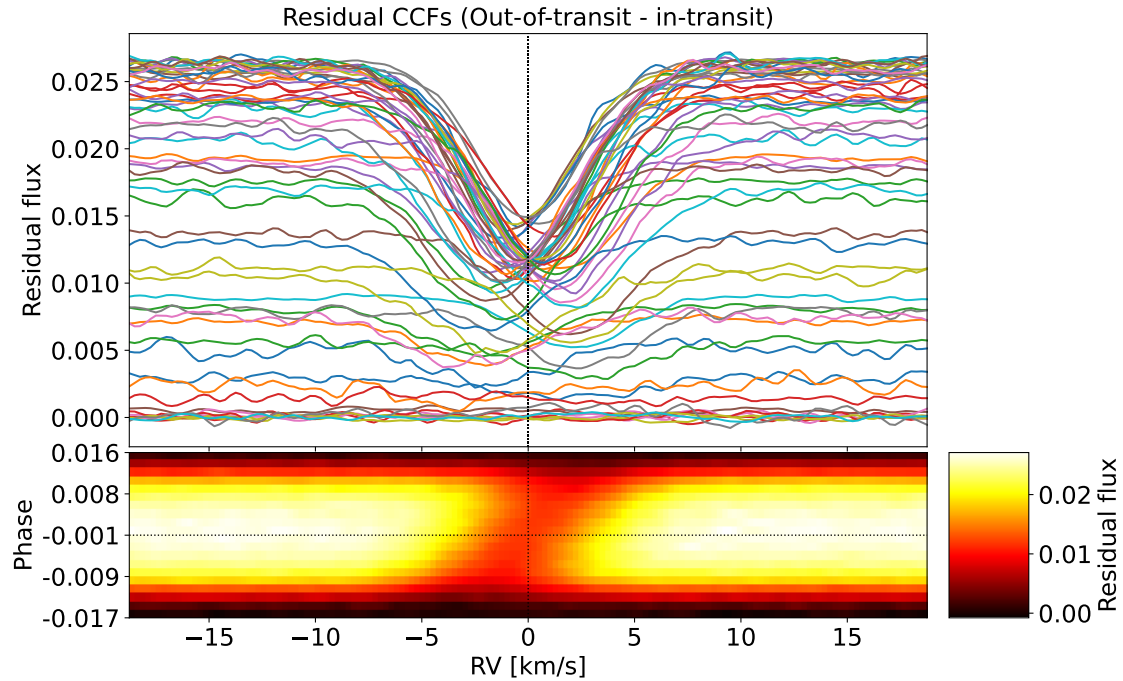


Figure 2.3: **Top:** this plot shows the residual of the CCFs obtained by subtracting the in-transit from the master out-of-transit CCFs. Different colours are used here for visualization purpose. **Bottom:** this is the residual map of a subset of the time series CCFs colourcoded by residual flux. The travelling bump in the in transit CCF profiles is recognizable as an orangish streak, as the planet moves in front of the disc of the star. Both plots are centered on a RV of 0 km s^{-1} , because the orbital motion and the systemic RVs have been removed.

setup for the DRS. For this reason, each night must be analyzed independently. The plots in Figure 2.2 display these steps. I have applied this procedure of flat part selection and normalization also to the in-transit CCFs. In this case the flux needed also to be scaled in order to keep into account for the limb darkening (LD) effect during the transit. To do that, my code uses the `batman`³ package to produce light curves modelled with a quadratic limb darkening law, with the LD coefficients u_1 and u_2 that are reported in Table 2.1. I have then multiplied the values of the flux obtained from the model by the corresponding observed ones and in this way I scaled the flux of the in-transit CCFs. Once the scaling is done, I could easily obtain the residuals by directly subtracting the in-transit from the master out-of-transit CCFs without having to assume any shape for them. The residuals are shown in Figure 2.3 using different colours for an easier visualization. Since the system velocities of the master out-of-transit CCFs have been removed, these residuals are set in the stellar rest frame where the velocity of rotation of the star

³Basic Transit Model cAlculationN in Python, by Laura Kreidberg <https://github.com/lkreidberg/batman>.

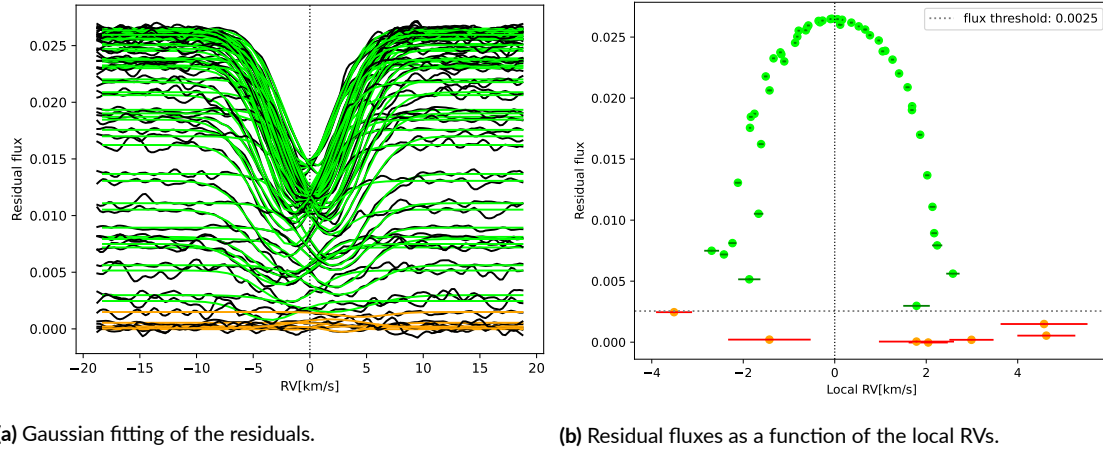


Figure 2.4: The result of the Gaussian fitting of the residuals is shown in Figure 2.4a with different colors for the cases in which the fit worked properly (lime) and the cases in which it didn't due to the small level of S/N (orange). The residual fluxes are plotted as a function of the local RVs in Figure 2.4b to see their trend. In particular, from this plot is possible to see how the orange points are the ones affected by the larger error and are located in different positions with respect to the general trend followed by the lime points. The horizontal dashed gray line representing the threshold in terms of flux and the vertical dashed black line showing that the lime points are symmetric with respect to the central RV of 0 km/s are also shown.

is evident. The residual CCFs that are closer to the stellar limb are the ones having a lower continuum flux level due to the LD effect and higher velocity shifts caused by the rotation of the star. In order to determine the values of the radial-velocities and flux from the residual CCFs, I performed a fitting with a Gaussian function on one in four points, to take into account also for the over-sampling of the CCF output by the HARPS pipeline, using a Levenberg-Marquardt least-squares minimisation. Figure 2.4a gives a visual feedback of the fitting using different colors to indicate whether the fit worked properly (lime) or not (orange). I computed the errors associated to the RV and to the flux as the square root of the diagonal elements of the covariance matrix obtained with the `curve_fit` function of the `scipy.optimize` package. By plotting the local RVs as a function of the fluxes values it is possible to visualise that points corresponding to values of the flux below a certain threshold are deviating from the general RV trend and are also affected by larger errors (see Figure 2.4b). These outlier points are the residual CCFs closer to the limb of the star that are affected by the LD effect, by the rotation of the star and include also the cases in which the planet is only partially covering the star during the transit ingress and egress. Still, the mean of the values of the RVs of the outlier points is 2.995 km s^{-1} , in agreement with the result of Cegla et al. 2016[3].

Since they are measured directly, the total RVs of the CCFs also include contributions from

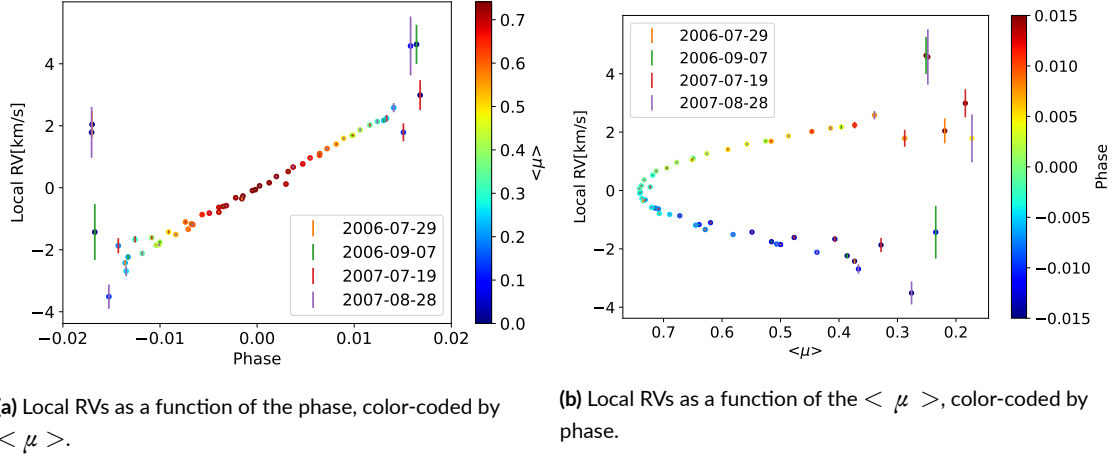


Figure 2.5: These are the plots showing the trend of the RVs as a function of the phase (Figure 2.5a) and as a function of the $\langle \mu \rangle$ (Figure 2.5b).

stellar rotation and the net convective velocities. In the Figure 2.5a I plotted the RVs of the in-transit residual CCFs as a function of the phase. The general trend shows a linear dependence of the RVs from the phase and the outlier points in this plot correspond to those mentioned before. In the Figure 2.5b I plotted the same RVs as a function of the brightness-weighted $\langle \mu \rangle$ behind the planet, (see Equation 2.12), and also in this case the outlier points can easily be recognized.

The value of the total velocity that I have obtained for the CCFs includes the Doppler-shifts of the residual CCF profiles caused by the stellar rotation behind the planet and the large scale centre-to-limb convective variation caused by the corrugated nature of granulation. In order to model the contribution of the stellar rotation to the residual CCF velocities, my code computes the brightness-weighted average differential rotation behind the planet, $v_{\langle \text{stel} \rangle}$, per each time of the observation. The position of the centre of the planet at any given orbital phase, φ is described as

$$x_p = \frac{a}{R_\star} \sin(2\pi\varphi), \quad (2.3)$$

$$y_p = -\frac{a}{R_\star} \cos(2\pi\varphi) \cos(i_p), \quad (2.4)$$

for a circular orbit, where a is the semi-major axis, R_\star is the radius of the host star and i_p is the inclination of the planetary orbit. The differential rotation requires the value of the orthogonal distance from the stellar spin-axis, x_\perp , which is obtained by rotating the coordinate system in

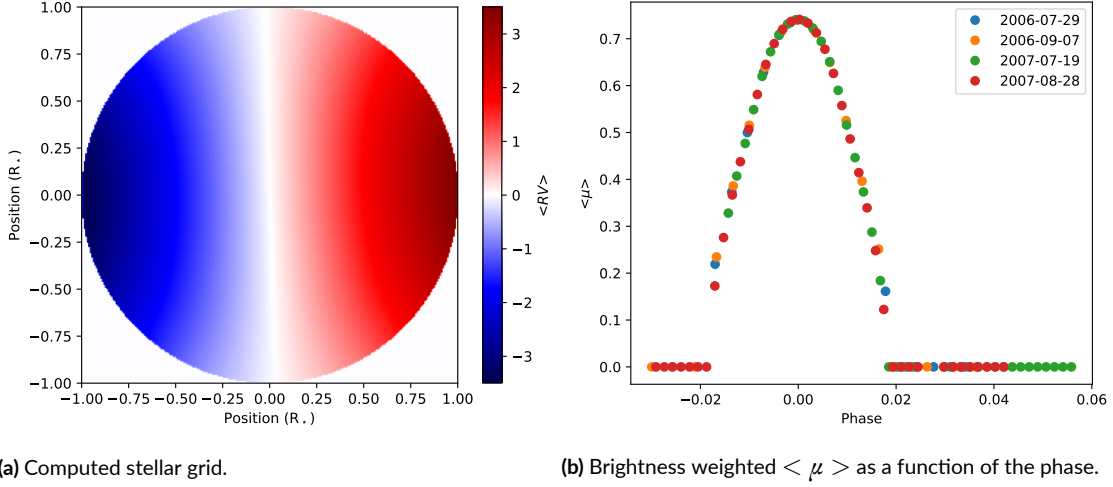


Figure 2.6: These are the plots showing the star grid obtained from the numerical computation on a square grid of 251 equal steps in x and y directions, colorcoded by the radial velocity, Figure 2.6, and the brightness weighted behind the planet obtained from the numerical computation of Equation 2.12, Figure 2.6b. The stellar grid is here computed on 251 instead of 51 steps only for visualization purpose.

the sky plane by the projected obliquity λ ,

$$x_{\perp} = x_p \cos(\lambda) - y_p \sin(\lambda), \quad (2.5)$$

$$y_{\perp} = x_p \sin(\lambda) + y_p \cos(\lambda). \quad (2.6)$$

Apart from the specific case in which $i_{\star} = 90^{\circ}$, this rotation is not sufficient to guarantee that the equator of the reference coordinate system and the equator of the star are aligned. For this reason, in order to calculate the differential rotation it is necessary to know also the orthogonal distance from the stellar equator, y'_{\perp} . To obtain it, the coordinate system is rotated again about the x_{\perp} axis by an angle $\beta = \pi/2 - i_{\star}$:

$$z'_{\perp} = z_{\perp} \cos(\beta) - y_{\perp} \sin(\beta), \quad (2.7)$$

$$y'_{\perp} = z_{\perp} \sin(\beta) + y_{\perp} \cos(\beta), \quad (2.8)$$

where $z_{\perp} = \sqrt{1 - x_{\perp}^2 - y_{\perp}^2}$, in units of R_{\star} .

Assuming a differential rotation law derived from the Sun, $\Omega = \Omega_{eq}(1 - \alpha \sin^2 \theta)$ [3], the

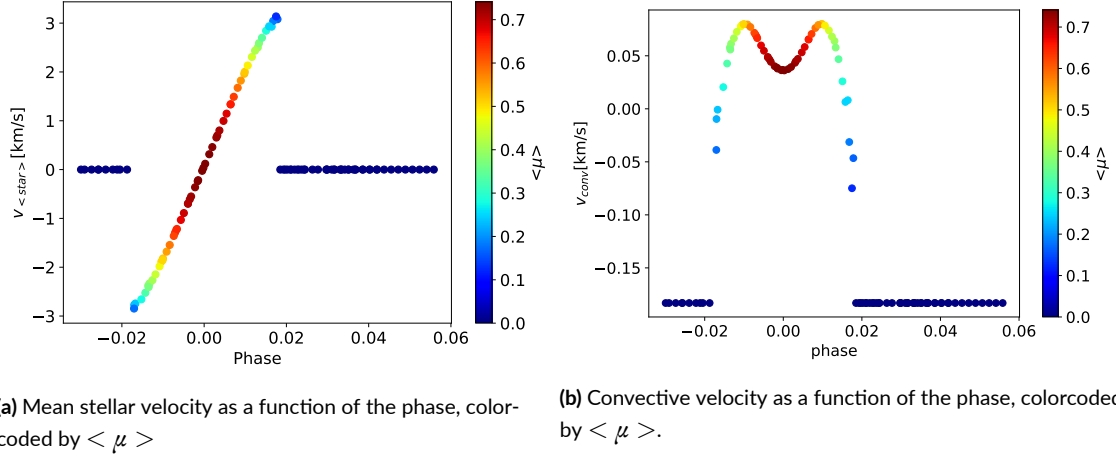


Figure 2.7: These are the plots showing the mean stellar velocity numerically computed according to the Equation 2.10 and the convective velocity obtained from Equation 2.11 plotted as a function of the phase. Non-zero values for the convective velocity outside the transit are a numerical artifact of the proposed approximation, and are ignored in the modelling of the measured RVs.

rotation velocity of the star for a given position is defined as

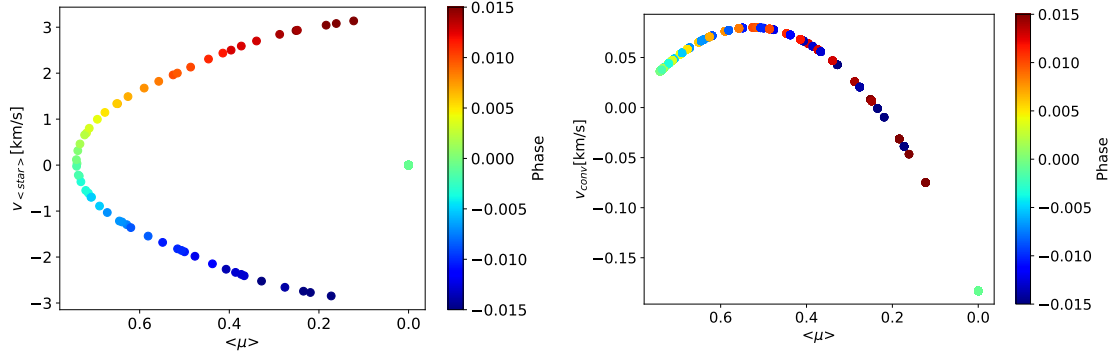
$$v_{stel} = x_{\perp} v_{eq} \sin i_{\star} (1 - \alpha y_{\perp}^2), \quad (2.9)$$

since $y'_{\perp} = \sin(\theta_{lat})$, where θ_{lat} is the latitude relative to the equator of the star and α is the differential rotation rate. The x_{\perp} and y'_{\perp} values are computed also for any x,y position inside the stellar disc and behind the planet. The $v_{\langle stel \rangle}$ is then numerically calculated as

$$v_{\langle stel \rangle} = \frac{\sum I v_{stel}}{\sum I}, \quad (2.10)$$

where I is the intensity determined using the limb darkening law. To compute $v_{\langle stel \rangle}$ numerically, my program constructs a stellar grid that is transited by the planet and performs the summation of the v_{stel} behind the planet over a square grid of 51 equal steps in the vertical and horizontal direction, which origin is defined at the planet center. I have excluded any contribution from the steps that do not lie beneath the planet and/or on the stellar disc, by setting the value of them to 0. I have also excluded the CCFs that are close to the limb, since they have very noisy profiles. My program also excludes the ones whose brightness-weighted $\langle \mu \rangle$ behind the planet has a value smaller than 0.25.

In my modelling I can also take account of the net convective shift v_{conv} . Since there is not an exact formulation for the contribution of v_{conv} , I have approximated it using a polynomial.



(a) Mean stellar velocity as a function of the $\langle \mu \rangle$, color-coded by phase. (b) Convective velocity as a function of the $\langle \mu \rangle$, color-coded by phase.

Figure 2.8: These are the plots showing the mean stellar velocity numerically computed according to the Equation 2.10 and the convective velocity obtained from Equation 2.11 plotted as a function of the $\langle \mu \rangle$.

The convective velocity has a radial symmetry about the disc centre, due to the fact that the granulation on the spherical host star has a corrugate nature. So the contribution of the centre-to-limb convective velocity has this expression

$$v_{conv} = \sum_{i=1}^{i=n} c_i \langle \mu \rangle^i \quad (2.11)$$

where n is the order of the polynomial and $\langle \mu \rangle$ is the brightness-weighted behind the planet, which is given by

$$\langle \mu \rangle = \frac{\sum I \mu}{\sum I}, \quad (2.12)$$

with $\mu = \cos \theta$ (θ centre-to-limb angle), and is also computed numerically by the program, summing over a stellar grid of 51 equal steps in x and y , centered on x_p, y_p as before. In the previous steps, while removing the RVs from the master out-of-transit CCFs, I have also removed the brightness-weighted v_{conv} of the whole stellar disc from the in-transit CCFs. For this reason, the condition that I impose on the coefficients of the polynomial during the v_{conv} polynomial fitting to the in-transit data is that the brightness-weighted net convective blueshift integrated over the stellar disc is zero

$$\frac{\int_0^\pi 2 \int_0^{\frac{\pi}{2}} I(\theta) v_{conv}(\theta) R_\star^2 \sin(\theta) d\theta d\varphi}{\int_0^\pi \int_0^{\frac{\pi}{2}} I(\theta) R_\star^2 \sin(\theta) d\theta d\varphi} = 0, \quad (2.13)$$

where $R_\star^2 \sin(\theta) d\theta d\varphi$ is the surface element dS_{R_\star} . To take into account only the half sphere facing the observer, the integration over φ is performed from 0 to π , while the integration over θ is written as twice the integral from 0 to $\pi/2$, because the two halves of the stellar disc are considered equal, since the center-to-limb variation is radially symmetric. Writing Equation 2.13 as a function of μ and solving for the constant offset c_0 in v_{conv} , the result is:

$$c_0 = -\frac{\sum_{i=1}^{i=n} c_i \int_0^1 I(\mu) \mu^{i+1} d\mu}{\int_0^1 I(\mu) \mu d\mu}. \quad (2.14)$$

This is the condition to be imposed when computing any v_{conv} polynomial. Finally the value of the total velocity of the occulted stellar region is:

$$v_{tot} = v_{\langle stel \rangle} + v_{conv}. \quad (2.15)$$

Table 2.3: Priors and boundaries values of the parameters used in the MCMC simulation.

Parameter	Prior	min	Max	units
$conv_{c_1}$	Uniform	-5.0	5.0	km/s
$conv_{c_2}$	Uniform	-5.0	5.0	km/s
v_{eq}	Uniform	0.0	10.0	km/s
i_\star	Uniform	0.0	180.0	deg
P_\star	Gaussian	1.0	1000.0	d
α	Uniform	0.0	1.0	
R/R_\star	Gaussian	0.10	0.20	
i_p	Gaussian	80.0	90.0	deg
λ	Uniform	-90.0	90.0	deg
a/R_\star	Gaussian	0.00	20.00	
T_C	Gaussian	2454279.3	2454279.5	d
P_p	Gaussian	2.10	2.30	d
jitter	Uniform	0.0002	29.0337	
ld_{C_1}	Gaussian	0.796	0.836	
ld_{C_2}	Gaussian	0.00	0.02	

Any transiting planet to which this analysis can be applied has also high precision light curves from which a/R_\star , i_p and R_p/R_\star can be measured in a more accurate and precise way than from the RM alone. In the case of HD189733, the values that I used to compute x_p and y_p for each in-transit epoch are taken from literature and are the ones that I have reported in Table 2.2.

The computation of $v_{\langle stel \rangle}$ also requires v_{eq} , i_* , λ and α . In order to obtain these quantities, I performed a fit with the Markov chain Monte Carlo (MCMC) algorithm, using the `emcee`[†] package. The MCMC fits also for each of the coefficients of Equation 2.11, since the v_{conv} is allowed to assume non-zero values. I provided none a priori knowledge of v_{conv} to the program, except for the condition that it must satisfy, which is given by Equation 2.14 and the order of the polynomial, which I set to 2. I set uniform priors on α , which value has to be in the $[0, 1]$ interval, since values outside this region are forbidden, on the equatorial velocity v_{eq} and on the stellar inclination i_* , while for the rotation period of the star P_* I set a Gaussian prior. Following the description that I found in the paper of Hathaway et al. 2015[4], in which the authors present a model for the convective blueshift velocity of the Sun with the corresponding coefficients, I fixed the boundaries on the convective coefficients $conv_{c_1}$ and $conv_{c_2}$ in a way to reproduce the model of this paper, i.e., I imposed that $conv_{c_1}$ has a positive value and that $conv_{c_2}$ has a negative value. I have constrained Gaussian priors also for the planetary parameters such as the orbital period P_p , the time of conjunction T_C , the ratio of planet radius to stellar radius R/R_* , the inclination i_p and the ratio of semi-major axis to stellar radius a/R_* and a uniform prior to the value of the sky-projected spin-orbit angle λ . I also set Gaussian priors to the coefficients of the quadratic limb darkening law ld_{c_1} and ld_{c_2} . In my analysis I have also included a jitter parameter, i.e., a constant to be added in quadrature to the error associated to the RV measurements in order to take into account possible under-estimation of the errors. For the jitter, I used a uniform prior. All these parameters with related information on the priors and boundaries used in the MCMC simulation are reported in Table 2.3. For the first analysis, I have randomly initialised 60 walkers over the range of the priors to make sure that they explore exhaustively the parameter space. The number of walkers is set to 4 times the number of parameters of the model, and the length of the chain is set to 10^5 steps, with a burn-in phase of 55, 000 steps. For the second analysis I decided to remove the contribution of the convective velocity, hence reducing the number of the parameters to 13, to see if and how much the result of the simulation changes. Also in this case I have randomly initialised the walkers over the range of the priors and I made them explore the parameter space with a chain of 10^5 steps with a burn-in phase which in this case is set to a value of 61, 000 steps. Both the MCMC analysis properly worked and all the parameters that I have fitted converged before the end of the chain. The results of these two analysis are reported in Table 2.4.

By combining the obtained values of i_* and λ , with the orbital inclination i_p , which value in

[†]emcee: The MCMC Hammer, by Daniel Foreman-Mackey, David W. Hogg, Dustin Lang and Jonathan Goodman <https://github.com/dfm/emcee>

both cases has a median value of 85.71° , I have determined the true 3D obliquity ψ using the following equation:

$$\psi = \arccos(\sin i_\star \cos \lambda \sin i_p + \cos i_\star \cos i_p). \quad (2.16)$$

In particular, in performing this calculation I did not simply use the median values of the three angles, but the sampled posteriors one by one, thus obtaining a distribution of values also for ψ . The resulting best fit values obtained as median of the values of ψ for the 2 simulations are reported in Table 2.4. In Figure 2.9 I displayed the corner plot of the quantities that I have

Table 2.4: MCMC observational results for HD189733 and the derived 3D spin-orbit obliquity.

v_{eq} (km s ⁻¹)	i_\star (°)	α	λ (°)	c_1^5 (km s ⁻¹)	c_2^5 (km s ⁻¹)	ψ (°)
$4.11^{+0.46}_{-0.44}$	$99.5^{+12.0}_{-9.6}$	$0.36^{+0.24}_{-0.17}$	$-2.7^{+1.0}_{-1.2}$	$0.21^{+0.32}_{-0.15}$	$-0.66^{+0.25}_{-0.37}$	$14.41^{+11.12}_{-8.08}$
$3.81^{+0.41}_{-0.35}$	$99.90^{+12.95}_{-14.28}$	$0.23^{+0.17}_{-0.14}$	$-0.15^{+0.54}_{-0.56}$	/	/	$15.38^{+12.15}_{-9.97}$

obtained from the two separate analysis using different colors. The most interesting fact that is highlighted in this corner plot is the existence of a degeneracy between the parameters i_\star and ψ that is not present in the corresponding corner plot obtained by Cegla and collaborators[3]. This degeneracy is recognisable as a V-shaped diverging linear trend in the marginalised two dimensional distribution panel of i_\star vs ψ , where it is clear that two distinct values of i_\star are associated to the same value of ψ . What I noticed is that, in this panel, the two distributions of i_\star converge to a point that has a value of 85.71° , which corresponds to the orbital inclination i_p . I checked the original paper for a visual feedback and I found that, even if in the corner plot of Cegla et al. 2016 there is a single distribution of values of i_\star , the point at which it encounters the x-axis of the corresponding panel is the same. This can not be just a coincidence. As a matter of fact, in this model the stellar spin angle is determined starting from the value of the differential rotation and of the equatorial rotation velocity. By definition, the differential rotation expresses how the rotation velocity of the star changes as a function of the stellar latitude, so the situation is symmetric with respect to the stellar equator. As a consequence, if I fix the value of i_p , then there are two possible geometric configurations, obtained by changing the inclination of the stellar spin axis with respect to the line of sight, for which all the other parameters are identical. This is because the transit chord can be both in the northern or in the southern hemisphere of the star, and the results that are obtained by modeling the CCFs of the planet-occulted stellar

⁵These are the convective coefficients of order 1 and 2.

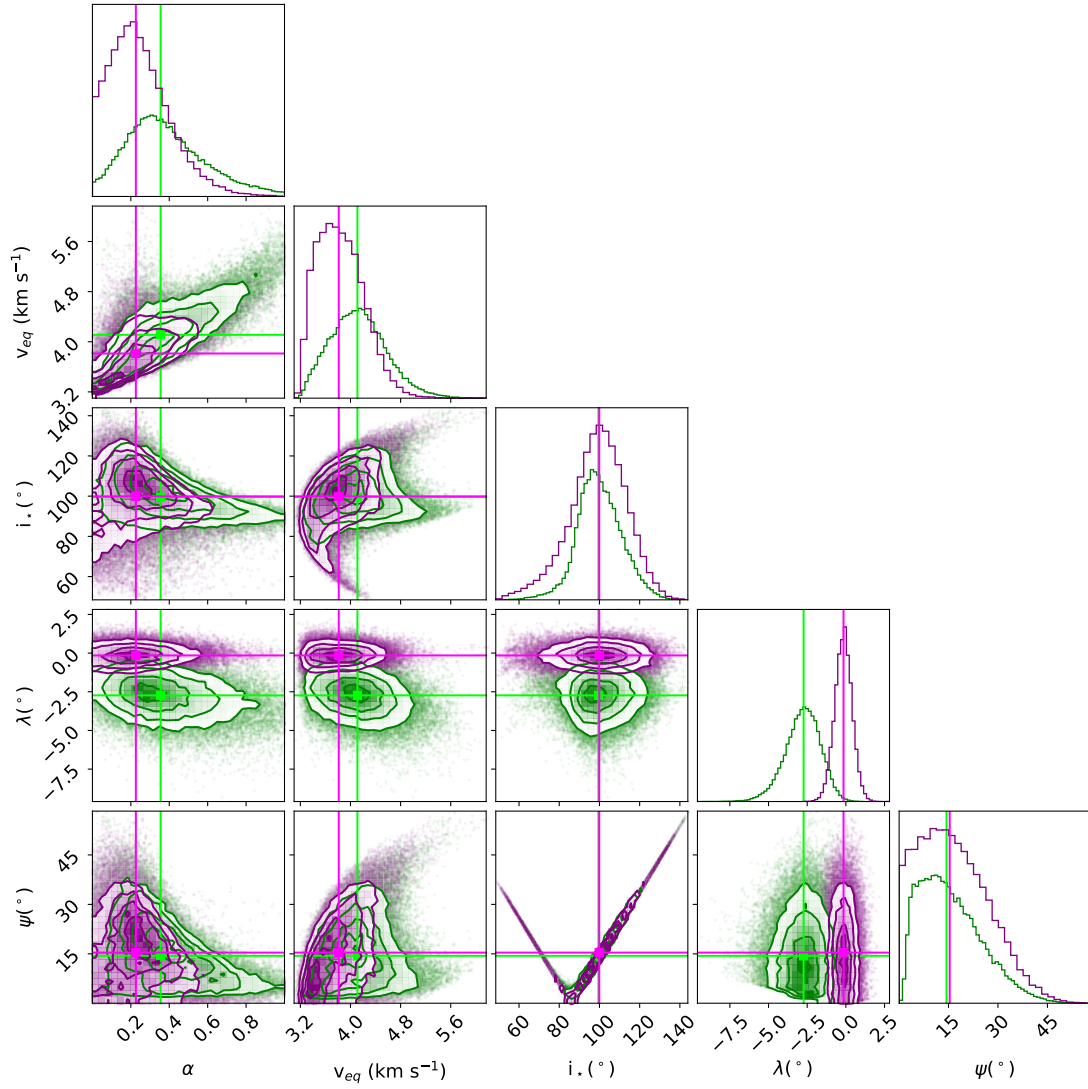


Figure 2.9: This is the corner plot of the parameters analysed with the MCMC simulation. Different colors are used here to better distinguish the distributions obtained from the two analysis. In particular, the green points are those corresponding to the first analysis, which also included the convective contribution to the velocity, while the purple points correspond to the second analysis, which did not include the convection. No big differences are observed in terms of distribution in the two cases a part from the λ parameter which changes from -2.7° for the convective to -0.15° for the non-convective case. Median values are also displayed.

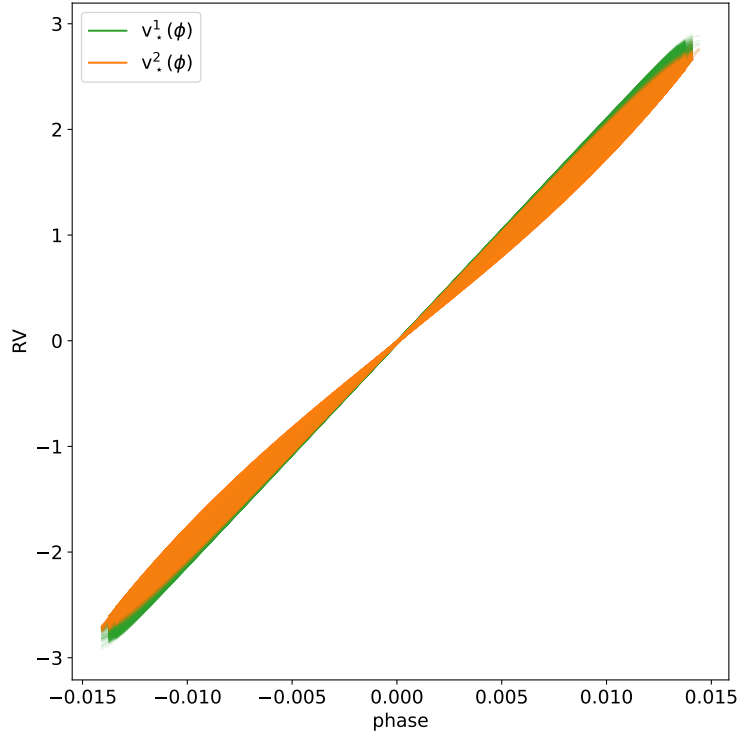


Figure 2.10: This is an example of the backwards reconstructed RV as a function of the phase angle. The RV here shown are obtained from simulated data, giving the values of i_* as input and not extracted from the residual CCFs as done before. Notice that even if the two fixed angles have a difference of 28° , the RV associated to them are still overlapping.

regions during the transit are exactly the same. Starting from this empirical evidence, I wanted to prove that this is the cause of the degeneracy on my results. As first, I double checked my script to make sure that no typo or wrong input values were present, and to exclude any other possible cause of the degeneracy. Then I decided to write a program with simulated data, to study the behaviour of the system in different geometric configurations. For this analysis I fixed the values of ω , e , P , T_0 , T_{tr} and a/R_* to the ones from the literature, which are reported in Table 2.2 and I also fixed the value of the stellar differential rotation α to 0.25 and that of $v \sin i_*$ to 3.8 km s^{-1} . I took advantage of the functions of Python to generate 10^2 values of time, centered on the literature value of T_0 , and I used them to determine the orbital phase. I have randomly generated a normal distribution for the value of the inclination of the planet centered on the literature value i_p , and for the value of λ , centered on the value of -0.4 , using in both cases 10^4 random points. The idea is that, since the degeneracy is related to the stellar spin angle, than there are two different values of i_* giving the same value of ψ . To prove my idea, instead of computing the value of i_* starting from the values of the equatorial velocity v_{eq} and

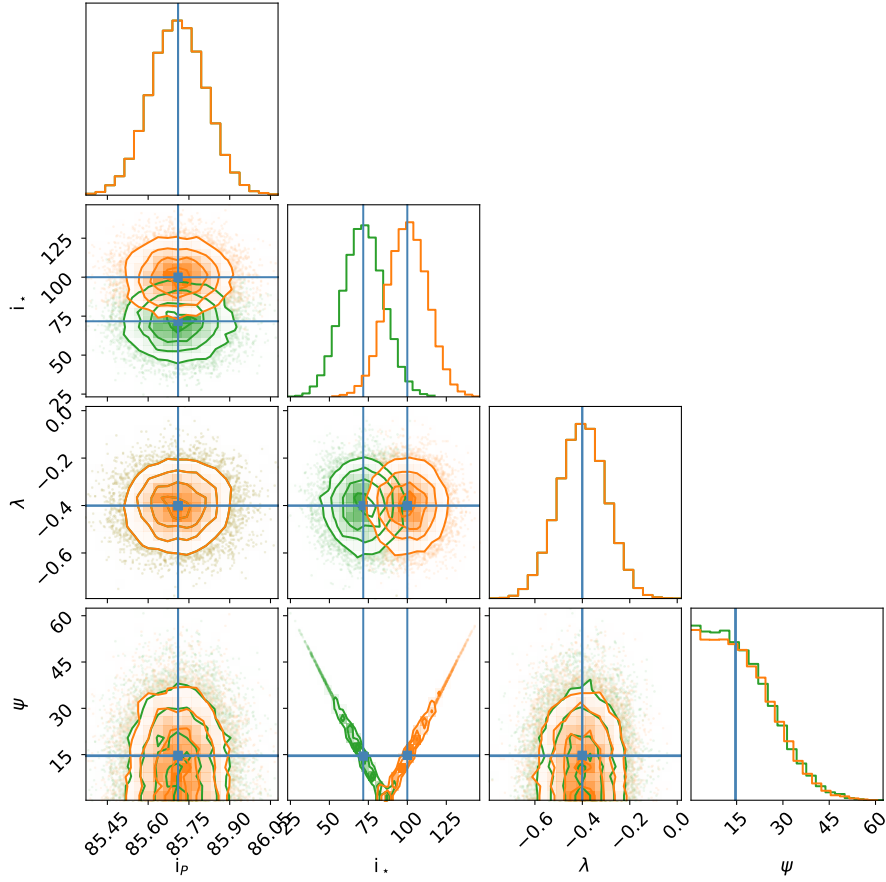


Figure 2.11: This is an example corner plot obtained starting from the simulated data. In the marginalised two dimensional distribution panel of i_* vs ψ is clearly recognizable the V-shaped diverging linear trend, that is expected in this case due to the fact of having assumed two distinct distribution of values for i_* . No major differences are instead spotted in the histogram of the marginalised distribution of ψ , confirming that it is nonetheless possible to constrain its value.

of the stellar differential rotation α , I assigned it as an input parameter to my program trying different couple of values. In Figure 2.10 I plotted with different colors the RVs as a function of the phase, to provide an example of how it is possible to reconstruct almost identical RV values starting from different stellar spin angles, proving indeed that the degeneracy is present. For the specific case in example, I used the couple $i_*^1 = 71.71^\circ$ and $i_*^2 = 99.71^\circ$, fixed as $i_p \pm 14^\circ$, to generate two normal distributions of stellar spin angles with a standard deviation of 13° . In this way the distribution related to the larger value falls between the two that I have obtained as a result of the MCMC simulations. I have then also obtained the corner plot associated to the same parameters of this analysis, which is shown in Figure 2.11. In the marginalised two dimensional distribution panel of i_* vs ψ , I obtained the V-shaped diverging linear trend as I

was expecting, due to the fact of having assigned as input two different values for the stellar spin angle. This degeneracy is also present in the other cases that I have considered, where I have changed the input values of i_* in a way to obtain two distributions which are symmetric with respect to the value of i_p , for which I do not provide the plots. Thanks to these results I can confirm that my analysis on the HARPS data has worked properly and rather Cegla and collaborators[3] have made some assumptions on the stellar spin angle value for which they did not provide any information, or the code they used for the MCMC simulation did not properly explore the values of i_* inside the interval of $[0, 180]^\circ$, as they claim, since from their corner plot it seems that there is a threshold on this parameter, apparently at the same value of the orbital inclination of the planet, which is indeed the value at which the posterior of the stellar inclination is specularly reflected.

From the analysis that I performed with my RRM code, I have also obtained new estimates for the value of $v_{eq} \sin i_*$, which I reported in Table 2.5 specifying if I have included the convective term or not in the analysis. The value obtained by including also the convection is slightly larger than the one obtained excluding it, in accordance with the trend found also by Cegla et al. 2016.

Table 2.5: $v_{eq} \sin i_*$ values obtained from the analysis.

Analysis	$v_{eq} \sin i_*$ (km s ⁻¹)
convection	$3.93^{+0.49}_{-0.39}$
no-convection	$3.63^{+0.36}_{-0.29}$

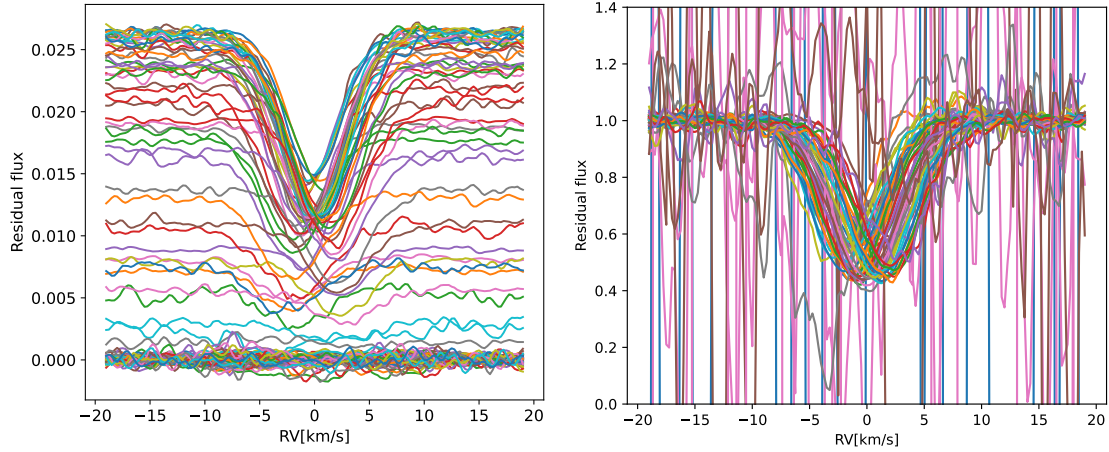
3

The Rossiter-McLaughlin effect Revolutions technique

In this chapter I provide a description of the Rossiter-McLaughlin effect Revolutions (RMR) technique. Also in this case, I had to build the mathematical framework and the various steps required for the data handling and the data analysis, taking advantage of those already implemented in the code that I wrote for the RRM technique, with the purpose of reproducing the improved technique presented by Bourrier et al.2021[2]. In this case, instead of reproducing their results on the HD3167 system, I worked with the same HARPS data on HD189733 that I used in the previous technique, reported in Table 2.1.

3.1 THE CODE FOR THE RMR

Bourrier and collaborators have not released their code to compute the Rossiter-McLaughlin effect Revolutions[2] yet. For this reason, I had to write my own code for the RMR, following the steps that are described in their paper, but using instead the same HARPS data on HD189733 on which I worked with the code for the Reloaded RM effect, that are reported in Table 2.1. The first step of this analysis, which consists in the extraction of the planet-occulted CCFs, is the same of that for the traditional RRM. Therefore I here just summarize the operations that I performed, since I have already provided a description for them in the previous chapter Sec-



(a) Residuals before the scaling, same as the RRM.

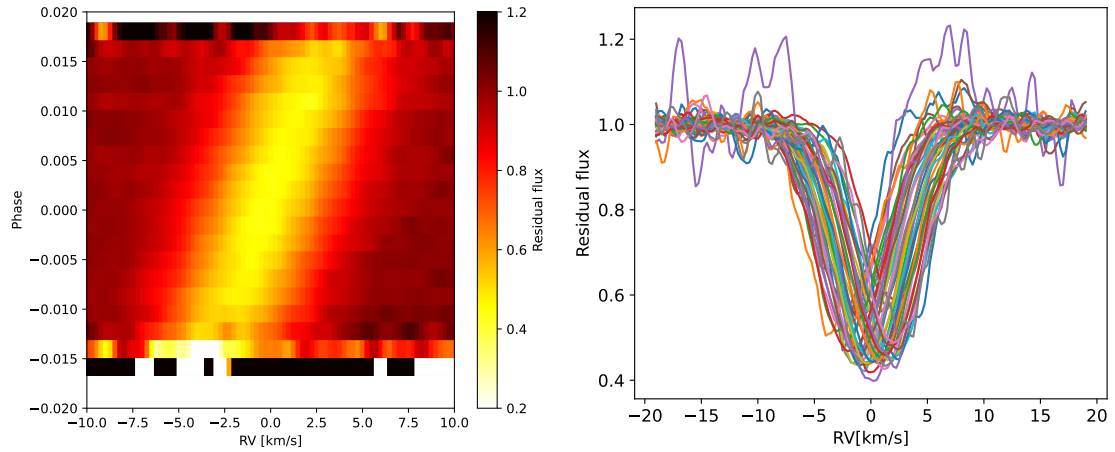
(b) Residuals after the scaling, same continuum value.

Figure 3.1: These plots show the difference between the residuals obtained with the RRM and with the RMR. Notice that in Figure 3.1b the vertical axis has been limited to a small range for visualization purpose and thus part of the residuals are cut. This is because the scaling of the residuals that have a flux close to zero encounters division by number that are almost zero, hence producing very large values.

tion 2.1. After selecting the CCFs, I have aligned them by correcting for the keplerian motion and the system velocity. Using the batman package, my code computed the light curves with the assumption of a quadratic limb darkening law. I then have scaled the fluxes of the CCFs using the corresponding values of the light curves as reference. I co-added the CCFs outside of the transit in order to get the master-out of transit and I have obtained the residual CCFs by subtracting the in-transit CCFs from the master-out of transit CCFs. Up to this operation, the two codes are identical, but in this case, instead of working with the CCF_{loc} as in the RRM, I reset the residual CCFs to a common flux level. To do that, I divided their continuum by the flux scaling obtained from the light curve modeled with batman, so that the residuals are given as

$$CCF_{residuals} = \frac{CCF_{master} - CCF_{in-transit} \cdot flux_{batman}^{LD}}{1 - flux_{batman}^{LD}}. \quad (3.1)$$

These resulting CCFs are independent from the occultation of the planet and from the effect of the LD on the continuum flux, hence they are intrinsic CCFs and they allow for a more direct comparison since they only display variations in the local stellar line profiles. In Figure 3.1 I visualise the difference between the residuals obtained with the traditional RRM approach and the ones obtained with the RMR technique, by showing the two plots one next to the other. In Figure 3.2a I display the map of the intrinsic CCFs during the transit, which is obtained



(a) Intrinsic CCF map during the transit.

(b) Clear scaled residual CCFs.

Figure 3.2: These plots show in Figure 3.2a an example of the map of the intrinsic CCF during the transit of HD 189733b, where values of the phase are plotted as a function of the RV in the stellar rest frame and are coloured as a function of their normalised flux, and in Figure 3.2 the clear scaled residual CCFs, which are a sub-set of the ones in Figure 3.1b, obtained by restricting the phase to the $[-0.015, 0.015]$ interval.

by plotting the scaled residual CCFs as a function of RV along the horizontal axis, and as a function of orbital phase along the vertical axis, and color-coded according to their value. The interval of phase inside which the signal to noise has an acceptable value is $[-0.015, 0.015]$, so I decided to plot again the residual CCFs limiting them to this phase interval, obtaining the plot of Figure 3.2b, which results much more clear than the one of Figure 3.1b thanks to the restriction that I have applied.

3.1.1 INDIVIDUAL EXPOSURES FITTING

The next step is that of analysing the individual exposures, in order to identify the variation of FWHM and contrast as a function of the limb angle μ . In the RRM approach, I fitted each CCF_{loc} with a stellar line model using the Levenberg-Marquardt least-squares minimization method. In order to determine if the local stellar line are to be considered detected and if the best fit properties can be used for the analysis, I applied a single arbitrary threshold, calculated using the properties of the fit. When data are affected by systematic errors, with the χ^2 minimization is difficult to understand if the model has been fitted to a stellar line or to a spurious feature. Furthermore, the χ^2 can bias the best-fit estimates and errors of the stellar line model if the parameters to be estimated are correlated within each others.

To improve this step, in the RMR technique I took advantage of the Bayesian approach. In

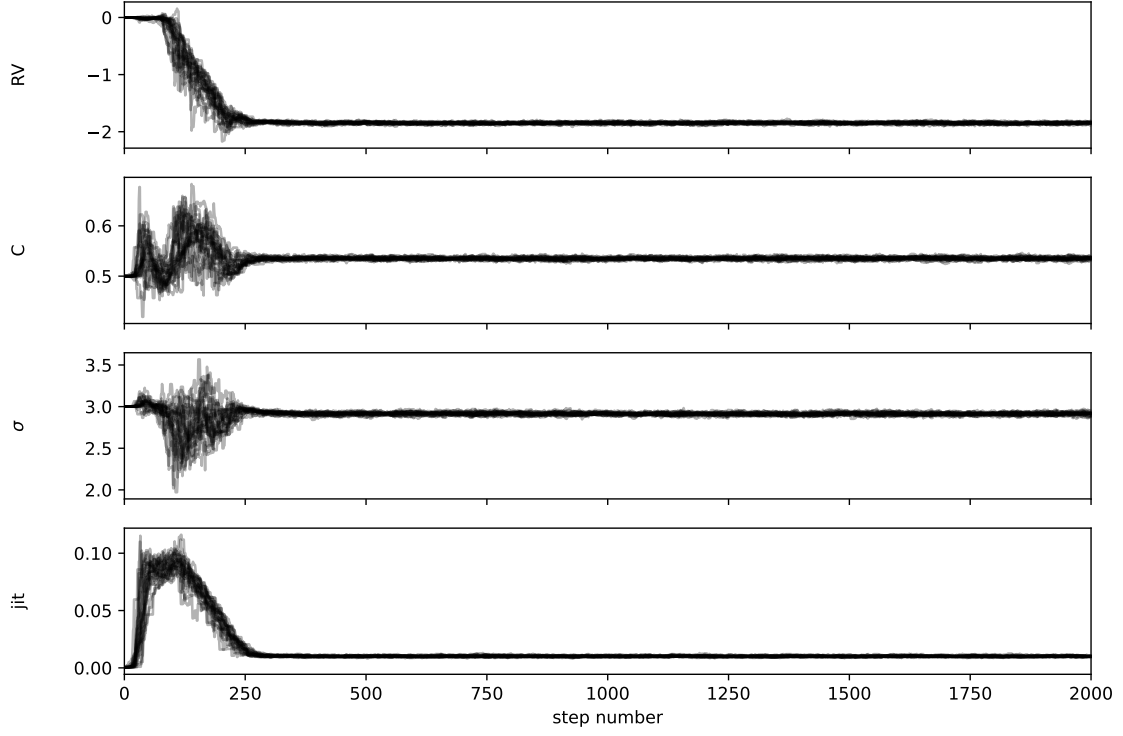


Figure 3.3: This is an example of the result of the single CCF fit, obtained from the MCMC simulation. Each of the MCMC chains for the RV centroid, for the contrast, for sigma and for the jitter, that are displayed in the plot, are related to the same CCF taken in example. The convergence is reached in about 300 steps and is kept up to the end of the chain, telling that the values have been properly found even if the chain is only 2000 steps long.

particular, I fitted each of the intrinsic CCFs with a stellar line model using emcee MCMC[5]. The model that I implemented in the code is that of a simple Gaussian defined as

$$1 - \frac{b}{\sqrt{2\pi\sigma^2}} e^{-\frac{(x-x_0)^2}{2\sigma^2}}, \quad (3.2)$$

where 1 corresponds to the value of the continuum of the flux, fixed by the scaling that I have applied to the CCFs and b is a term of normalization that enters in the contrast C , defined as

$$C = \frac{b}{\sqrt{2\pi\sigma^2}}, \quad (3.3)$$

so that the Equation 3.2 can be written as

$$1 - Ce^{-\frac{(x-x_0)^2}{2\sigma^2}}. \quad (3.4)$$

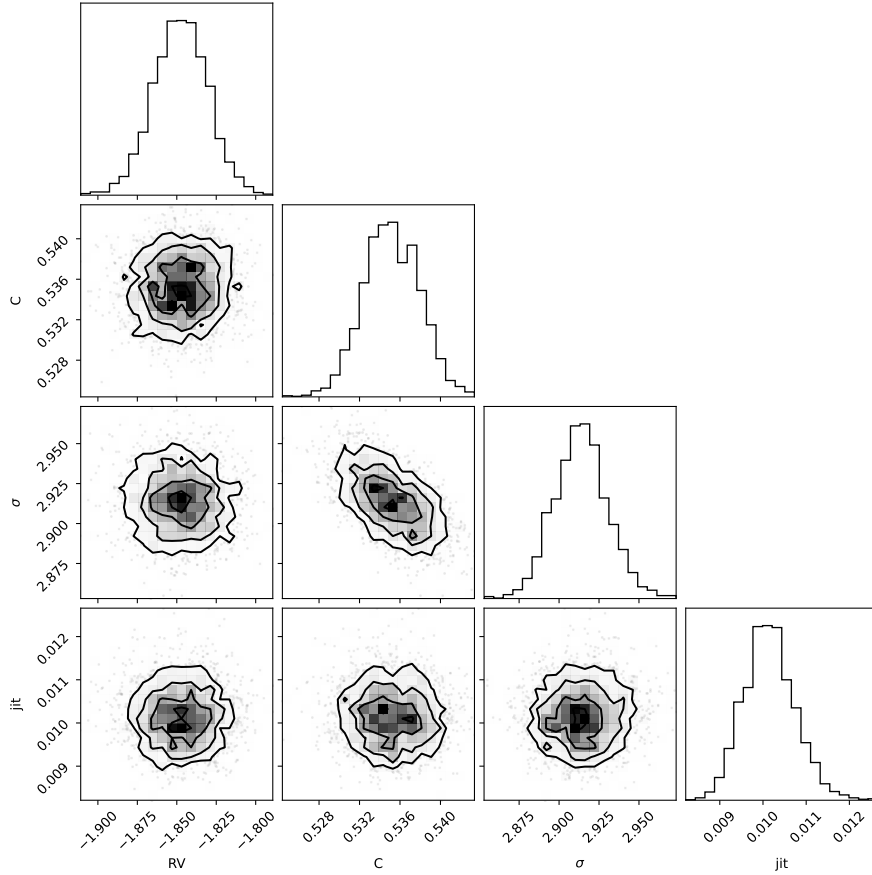
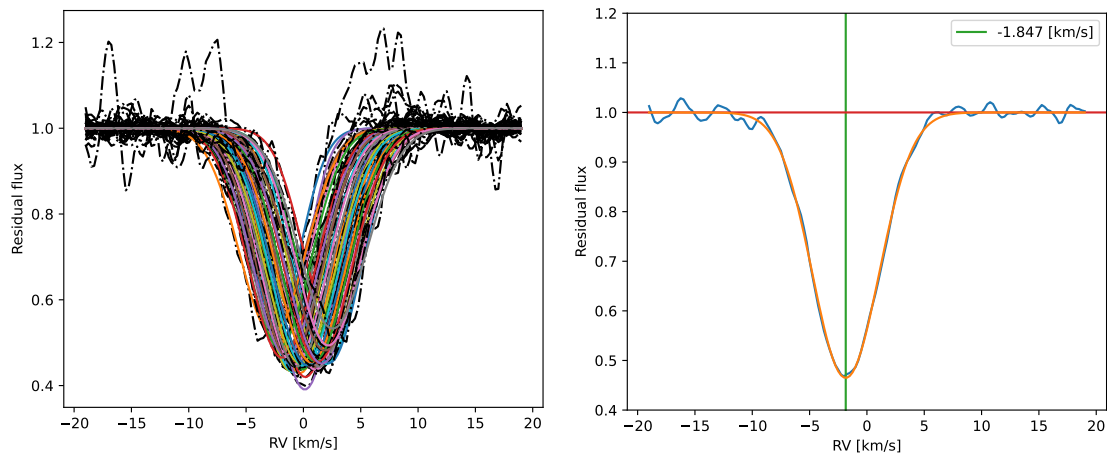


Figure 3.4: This is an example of corner plot obtained as a result of the MCMC simulation. The parameters here displayed are the ones taken in example in Figure 3.3.

I have set jump parameters to the RV centroid x_0 , to the contrast C , to σ and to the jitter, which is a constant that I added in quadrature to the error associated to the measures in order to take into account possible under-estimation of the errors. Taking as reference the results obtained from the previous RRM analysis, I have set a uniform prior distribution on the RV centroid in the interval $[-5, 5]$ km/s. According to the scaling that I have applied, the value of the flux at the center of the stellar absorption lines ranges between 0 and the local continuum of 1, but in order to evaluate the impact of noise on the line detection, I have set an uniform prior distribution on the line contrast over a larger range of $[-0.5, 1.5]$. I have set another uniform prior distribution between $[0, 20]$ km/s on σ , an interval of almost 3 times the average value of σ , while I decided to set a logarithmic prior distribution on the jitter term in an interval of $[-8, 0]$, since the value I expected was small. I have randomly initialised the walkers over the range of the priors to make sure that they explored exhaustively the parameter space. I have fixed the number



(a) Best-fit of all the residuals.

(b) Example of a single best-fit residual.

Figure 3.5: These plots show the best-fit of the residuals obtained as a result of the MCMC simulation. In Figure 3.5a all the CCFs are plotted together, using a dashed-dotted black line for the residuals and continuous lines of different colours for the modeled best-fit values. In Figure 3.5b, an example of a single residual CCF is selected in order to better visualise the result of the fit. The orange curve is the result of the fit of the gaussian model, the red horizontal line corresponds to the common flux value (fixed at 1) and the green vertical line is centered on the value of the RV of this specific CCF.

of walkers for the first analysis to 24, which corresponds to 6 times the number of the parameters, and the length of the chain to 2000 steps, with a burn-in phase of 500 steps. Once the test was done, I have taken the median of the posterior probability distributions as best-fit values for the model parameters and assigned errors as the discrete difference between the median and the 16 and 84 percentile. In Figure 3.3 I show an example of the chains obtained as a result of the MCMC simulation. From this plot is possible to see that the chains have very quickly converged in about 300 steps, stably staying there up to the end of the chains. This is telling that the simulation has properly worked even if the chains were only 2000 steps long. In Figure 3.4, I show an example of all the one and two dimensional projections of the posterior probability distributions of my parameters. This corner plot is useful because it demonstrates quickly the co-variances between parameters. In fact, the diagonal of the plot shows with histograms the marginalised distribution independently for each parameter, while the other panels show the marginalised two dimensional distributions. I decided to also plot the values of the best-fit, obtained from the emcee test as the median value of the posterior probability distribution. In particular in Figure 3.5a I plotted the residual CCFs all together with their corresponding fitted gaussian model, and in Figure 3.5b I plotted a single CCF, chosen as example, to have a better visualisation of the fitting. With the results obtained from the fit I have also realised the three plots in Figure 3.6, considering the entire set of data from the four night of observation. The

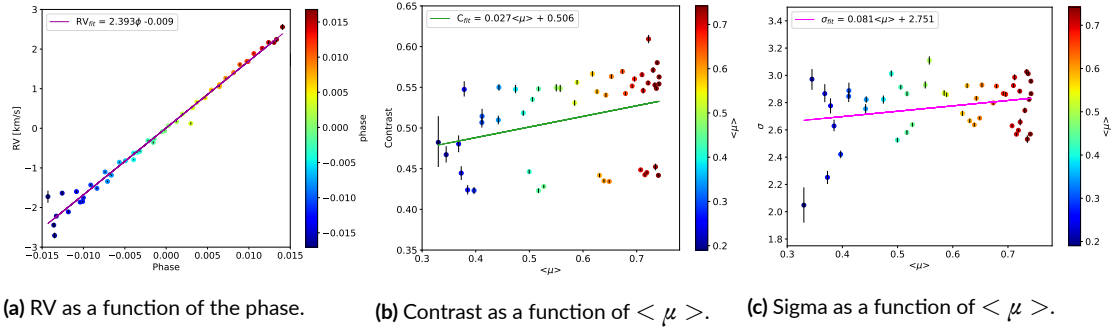
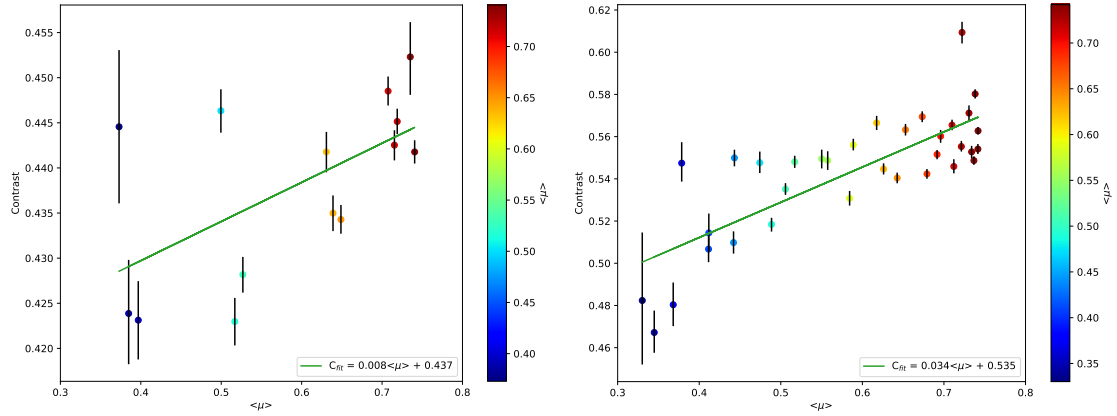


Figure 3.6: **Left:** In this figure the RVs are plotted as a function of the orbital phase restricted to the interval $\varphi = [-0.015, 0.015]$, and the points are color-coded by phase. The purple line representing the linear fit is also displayed. **Middle:** the values of the contrast are plotted as a function of the brightness-weighted behind the planet $\langle \mu \rangle$. **Right:** the values of the sigma are plotted as a function of $\langle \mu \rangle$. In both cases the points are color-coded by $\langle \mu \rangle$. Also in these plots the points are following a general linear trend, with an increase in the value of contrast and sigma as a function of $\langle \mu \rangle$. The green and magenta lines represent the result of the linear fit to the data.

first in Figure 3.6a is that of the radial velocity as a function of the orbital phase, which shows that RV depends linearly by φ as $RV(\varphi) = 2.393\varphi - 0.009$. The second in Figure 3.6b is that of the contrast as a function of the brightness-weighted behind the planet, which also appears to follow a linear trend, with a fitted value of $C(\mu) = 0.027\mu + 0.506$. Actually, in this plot it is possible to distinguish two different linear trends characterised by different slopes. This is related to the fact that the data that I have combined in the plot come from observations carried out using different filtering masks, the ones indicated in Table 2.1. This difference in terms of contrast is the same that I have explained in Section 2.1, where I discussed the normalised master out-of-transit CCFs, displayed in Figure 2.2c. Hence, to better visualise this difference in terms of slope, I have plotted again in Figure 3.7 the contrast as a function of $\langle \mu \rangle$, this time separating the values according to the filtering mask used to obtain them and I got $C_{K5}(\mu) = 0.008\mu + 0.437$ and $C_{G2}(\mu) = 0.034\mu + 0.535$ as a result of the fit. The third in Figure 3.6c is the plot of σ as a function of $\langle \mu \rangle$, which again shows a linear dependence between these two quantities, fitted as $\sigma(\mu) = 0.081\mu + 2.751$. Following the same strategy that I have adopted in Chapter 3, in order to plot a clearer version of the residual CCFs, (Figure 3.2b), I have conveniently decided to show also in these three plots only the points within the interval of φ and $\langle \mu \rangle$ where the fit have properly worked. In this way I have excluded the outlier points, which correspond to the measurements obtained outside the interval $\varphi = [-0.015, 0.015]$, close to the edges of the stellar disk, where the level of S/N is almost zero and for which the scaling that I have applied emphasises the noise, as shown in Figure 3.1b. Even if in the original work of Bourrier et al. 2021[2], the authors say that they did not apply any arbitrary threshold,



(a) Contrast as a function of $\langle \mu \rangle$ for the K5 mask only. (b) Contrast as a function of $\langle \mu \rangle$ for the G2 mask only.

Figure 3.7: These plots display a zoom of the Figure 3.6b, obtained by excluding again the values with $\langle \mu \rangle$ below 0.3 and separating them according to the mask that has been used to carry out the observations. From these plots is possible to see the different slopes of the linear fit.

I decided to apply it anyway, for visualisation purpose.

3.1.2 GLOBAL TRANSIT ANALYSIS

Up to here, the RMR approach has much in common with the RRM technique, a part for the scaling that is applied to the residual CCFs and for the Bayesian approach used in the modelling of the individual exposures. The next step, which represents the main novelty of the RMR approach, is that that of fitting all the intrinsic CCFs together with a joint model, instead of fitting them individually.

Keeping into account the results that I found during the analysis of the individual exposures, I decided to separate the data of the different nights according to the filtering mask that had been used to carry out the observations. This produced two distinct sets of data, that I labeled as K5 and G2 with clear reference to the mask. Working separately on each dataset I prepared the parameters with priors and boundaries to be given as inputs for the modelling. Also in this case, to perform the fit I used the MCMC algorithm implemented in the emcee package. Many analytical models can be applied to describe the stellar line profile, both keeping constant the properties in all exposures, or setting them by parametric models as a function of a given coordinate parameter. In my implementation I have decided to set the RV centroids of the theoretical lines by the same surface RV model, described in Cegla et al. 2016[6], that I have used to implement the RRM method. As I have reported in Section 2.1, this model ac-

counts for the projected stellar rotational velocity field, and its blur over the region occulted by the planet for a given exposure, including also the differential rotation of the star and the convective blue-shift. To quantify the contribution of the stellar rotation, my code computes the brightness-weighted average differential rotation behind the planet, $v_{\langle stel \rangle}$ according to Equation 2.10. The computation of $v_{\langle stel \rangle}$ requires the quantities v_{eq} , i_* , λ and α , which values are also fitted by emcee. The convective contribution v_{conv} , defined in Equation 2.11, is allowed to assume non-zero values. I did not provide any a priori knowledge of v_{conv} to the program, but I imposed the condition that it must satisfy, expressed by Equation 2.14, and the order of the polynomial to be used, which I set to 2. As a consequence of this choice, I required emcee to fit the 2 coefficients of the second order polynomial expression for v_{conv} . I have then set uniform priors on α , on the equatorial velocity v_{eq} and on the stellar inclination i_* , while for the rotation period of the star P_* I set a Gaussian prior. Also in this case I have fixed the boundaries on the convective coefficients $conv_{c_1}$ and $conv_{c_2}$ in a way to reproduce the model presented in the paper of Hathaway et al. 2015[4], by imposing that $conv_{c_1}$ has a positive value and that $conv_{c_2}$ has a negative value. I have constrained Gaussian priors for the planetary parameters such as the orbital period P_p , the time of conjunction T_C , the ratio of planet radius to stellar radius R/R_* , the inclination i_p and the ratio of semi-major axis to stellar radius a/R_* and a uniform prior to the value of the sky-projected spin-orbit angle λ . To be consistent with the model of the RRM technique, I used also in this case a quadratic limb darkening law, setting Gaussian priors to its coefficients ld_{c_1} and ld_{c_2} . In order to exploit the full extent of information contained in the data, I fitted the profiles of the local stellar lines occulted by the planet, rather than just their centroids as in the traditional RRM technique, using a Gaussian profile for the modelling. This allowed me to boost the S/N of the occulted stellar lines by a factor which is proportional to the number of in-transit exposures, thus increasing the possibility of constraining the planet path even when the line was not detectable in individual exposures. Given that the analysis of individual exposures allowed me to find a linear dependency of both the contrast and the FWHM with $\langle \mu \rangle$, I decided to explore this trend with emcee, fitting them with a first order polynomial. In particular, for both of them I fitted the slope, C_m and $FWHM_m$, and the intercept, C_q and $FWHM_q$, and I also included a jitter parameter, using uniform priors with the same boundaries for the G2 and the K5 dataset.

All these parameters with related information on the priors and boundaries used in the MCMC simulation are reported in Table 3.1.

For the first analysis, I have randomly initialised 96 walkers over the range of the priors to make sure that they explore exhaustively the parameter space. The number of walkers is set

Table 3.1: Priors and boundaries values of the parameters used in the MCMC simulation.

Parameter	Prior	min	Max	units
conv_{c_1}	Uniform	0	5.0	km/s
conv_{c_2}	Uniform	-5.0	0	km/s
v_{eq}	Uniform	0.0	10.0	km/s
i_*	Uniform	0.0	180.0	deg
P_*	Gaussian	1.0	1000.0	d
$\text{vsin } i_*$	Uniform	0.0	200.0	km/s
R_*	Gaussian	0.75	0.85	km
α	Uniform	0.0	1.0	
R/R_*	Gaussian	0.10	0.20	
i_p	Gaussian	80.0	90.0	deg
λ	Uniform	-90.0	90.0	deg
a/R_*	Gaussian	0.00	20.00	
T_C	Gaussian	2454279.3	2454279.5	d
P_p	Gaussian	2.10	2.30	d
C_m	Uniform	-10.0	10.0	
C_q	Uniform	0.0	1.0	
σ_m	Uniform	-10.0	10.0	
σ_q	Uniform	0.0	70.0	
jitter	Uniform	0.0002	29.0337	
ld_{C_1}	Gaussian	0.796	0.836	
ld_{C_2}	Gaussian	0.00	0.02	

to 4 times the number of parameters of the model, and the length of the chain is set to 10^5 steps, with a burn-in phase of 28,000 steps. For the second analysis I decided to remove the contribution of the convective velocity, hence reducing the number of the parameters to 22, to see if and how much the result of the simulation changes. Also in this case I have randomly initialised the walkers over the range of the priors and I made them explore the parameter space with a chain of 10^5 steps with a burn-in phase which in this case is set to a value of 69,800 steps. Then I also have performed a third analysis, in which I have excluded the stellar differential rotation from the parameters, fitting $\text{vsin } i_*$ and the stellar radius R_* instead, and including the contribution of the convection. The MCMC analysis properly worked in the three cases, and all the parameters that I have fitted converged before the end of the chain. The results of these three analysis are reported in Table 3.2 and in Table 3.3. The values and error associated to them are defined also in this case using the median and its discrete difference with the 16 and

the 84 percentile.

By combining the obtained values of i_* and λ , with the orbital inclination i_p , which median value is 85.71° , I have determined the true 3D obliquity ψ using the following equation:

$$\psi = \arccos(\sin i_* \cos \lambda \sin i_p + \cos i_* \cos i_p). \quad (3.5)$$

In particular, in performing this calculation I did not simply use the median values of the three angles, but the sampled posteriors one by one, thus obtaining a distribution of values also for ψ . In the specific case of the third analysis, before to compute ψ I had to compute also i_* , starting from the values of $v \sin i_*$, and v_{eq} using the values of R_* and P_* obtained from the fit. To compute v_{eq} I applied the simple equation of the circular motion

$$v_{eq} = \frac{2\pi R_*}{P_*}, \quad (3.6)$$

and I used these computed values to extract i_* from $v \sin i_*$ simply as

$$i_* = \arcsin \left(v \sin i_* \cdot \frac{P_*}{2\pi R_*} \right). \quad (3.7)$$

The resulting best fit values obtained as median of the values of ψ for the three simulations are reported in Table 3.2.

Table 3.2: MCMC observational results for HD189733 and the derived 3D spin-orbit obliquity.

v_{eq} (km s ⁻¹)	i_* (°)	α	λ (°)	c_1 (km s ⁻¹)	c_2 (km s ⁻¹)	ψ (°)
$4.47^{+0.15}_{-0.11}$	$108.4^{+8.2}_{-6.7}$	$0.34^{+0.12}_{-0.08}$	$-0.98^{+0.15}_{-0.16}$	$0.45^{+0.07}_{-0.03}$	$-0.53^{+0.05}_{-0.07}$	$22.71^{+8.21}_{-6.66}$
$5.45^{+0.09}_{-0.11}$	$90.83^{+0.69}_{-0.68}$	$0.98^{+0.02}_{-0.04}$	$0.93^{+0.10}_{-0.10}$	/	/	$5.21^{+0.68}_{-0.66}$
$3.56^{+0.32}_{-0.17}$	$69.27^{+9.73}_{-10.26}$	/	$-0.84^{+0.16}_{-0.16}$	$0.06^{+0.09}_{-0.04}$	$-0.46^{+0.04}_{-0.07}$	$16.46^{+10.26}_{-9.69}$

Table 3.3: Slopes and intercepts of contrast and of FWHM for the three analysis.

Analysis Parameter	1 st G2 Value	1 st K5 Value	2 nd G2 Value	2 nd K5 Value	3 rd G2 Value	3 rd K5 Value
C_m	$0.125^{+0.007}_{-0.007}$	$0.063^{+0.007}_{-0.007}$	$0.127^{+0.007}_{-0.007}$	$0.063^{+0.007}_{-0.007}$	$0.126^{+0.007}_{-0.007}$	$0.063^{+0.007}_{-0.007}$
C_q	$0.466^{+0.005}_{-0.005}$	$0.395^{+0.005}_{-0.004}$	$0.464^{+0.005}_{-0.005}$	$0.395^{+0.004}_{-0.005}$	$0.465^{+0.004}_{-0.005}$	$0.395^{+0.004}_{-0.005}$
$fwbm_m$	$0.39^{+0.10}_{-0.10}$	$0.39^{+0.10}_{-0.10}$	$0.38^{+0.10}_{-0.10}$	$0.36^{+0.11}_{-0.11}$	$0.38^{+0.10}_{-0.10}$	$0.40^{+0.11}_{-0.11}$
$fwbm_q$	$6.52^{+0.07}_{-0.07}$	$5.85^{+0.07}_{-0.07}$	$6.52^{+0.07}_{-0.07}$	$5.87^{+0.07}_{-0.07}$	$6.53^{+0.07}_{-0.07}$	$5.85^{+0.07}_{-0.07}$

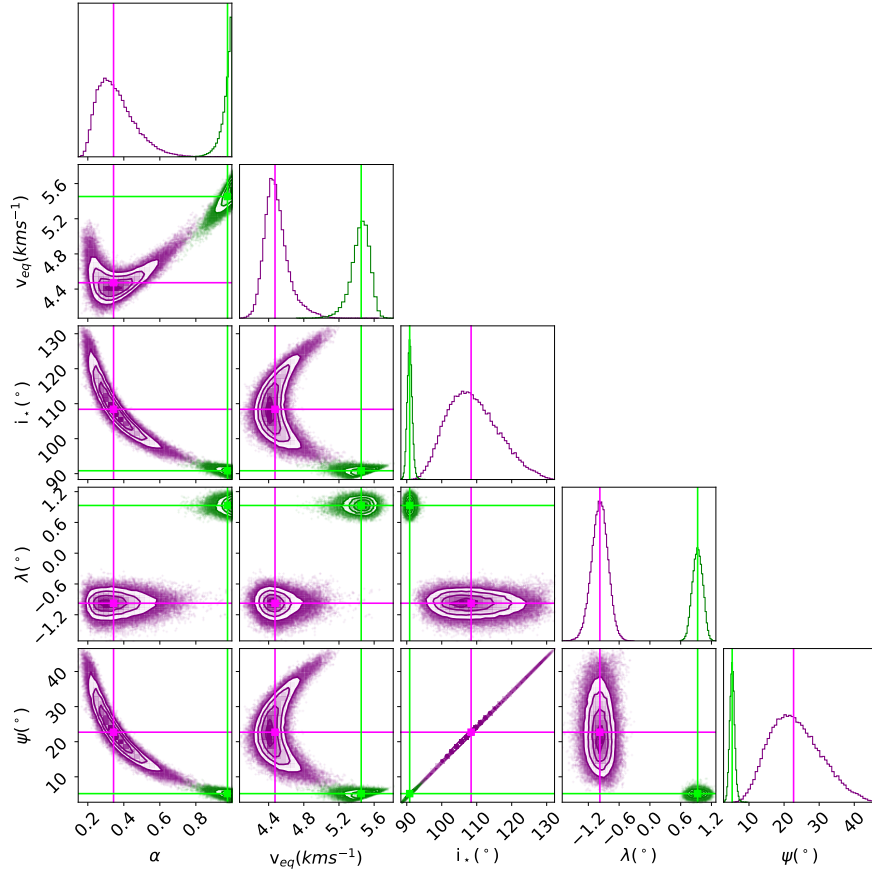


Figure 3.8: This is the corner plot that visualises the results of the first and second analysis. It is clear the difference in the parameters obtained in the convective case (purple) and in the non convective case (green).

The results that I have reported in Table 3.2 are very different in the three analysis. Considering for example the α parameter, the values that I have obtained including the convective contribution and not including it are not even compatible the one with the other. I decided to display in Figure 3.8 a corner plot with the results of these two analysis, using different colors to better show all the differences between them. From the corner plot is easy to see that, differently from what I found with the RRM technique (compare with Figure 2.9), none of the parameters obtained in one analysis has a compatible counterpart in the other.

In the third RMR analysis, that I performed including the convective contribution, but excluding the differential rotation, I got a smaller value for the stellar inclination with respect to the ones that I have obtained from all the previous analysis. I have computed i_* by combining the distributions for P_* and R_* with that for $v \sin i_*$, which are quantities that have been fitted independently, but I can not exclude that the distribution for i_* is affected by a possible system-

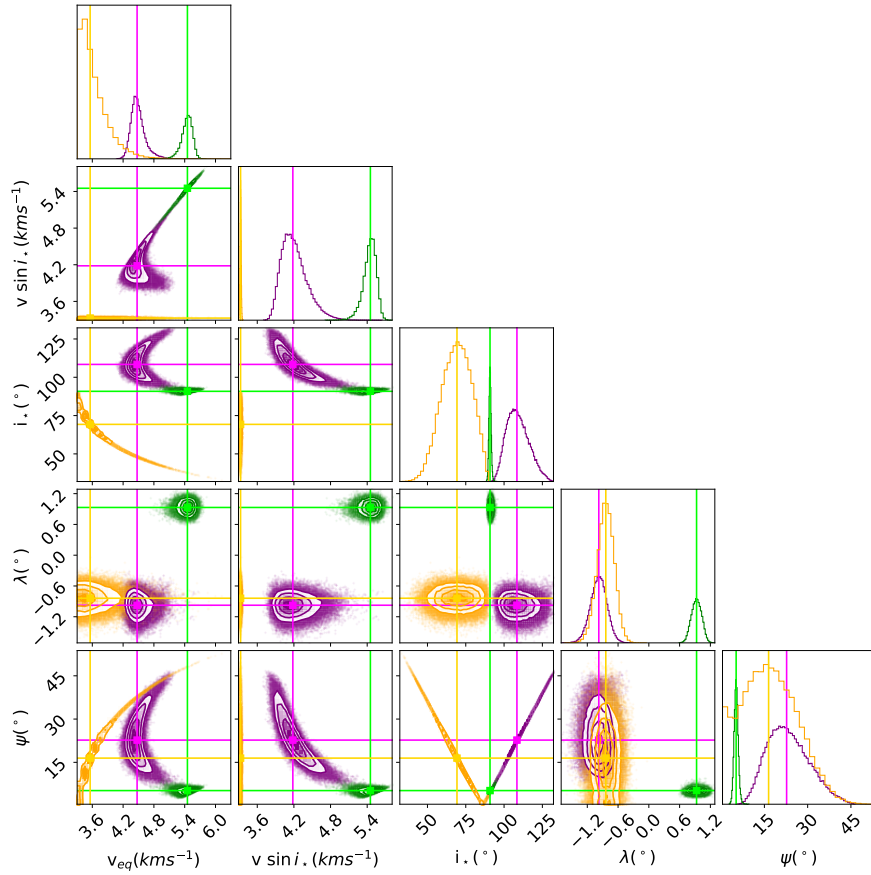


Figure 3.9: This is the corner plot that visualises the results of the three analysis. Colors are indicative of the analysis, in particular purple is for the convective with differential velocity, or orange for the convective without differential velocity and green is for the non convective analysis.

atic error caused by the inter-dependency of these quantities. In the Figure 3.9 I displayed in a corner plot the distributions of the parameters that I have obtained as a result of the three analysis using different colors in order to better distinguish them. It is clear from Figure 3.9 that the i_* degeneracy, that I discovered in the RRM analysis, is still present. This because the values of ψ obtained from the first and third analysis are compatible, despite the fact of having used two very different distributions of i_* values to compute them. In this plot I have also shown the distributions of the $v \sin i_*$ values that I have obtained. Taking the median of the distributions as best fit value and the discrete difference between the median and the 16 and 84 percentile as error associated to it, I got the new estimates also for the $v \sin i_*$, that I reported in Table 3.4 specifying the number of the analysis from which they come from. The results that I have obtained for the slopes and intercepts of the contrast and of the FWHM of the spectral lines,

Table 3.4: $v_{eq} \sin i_*$ values obtained from the analysis.

Parameter	1 st analysis	2 st analysis	3 rd analysis
$v_{eq} \sin i_*$ (km s ⁻¹)	4.18 ^{+0.24} _{-0.18}	5.45 ^{+0.09} _{-0.11}	3.33 ^{+0.01} _{-0.01}

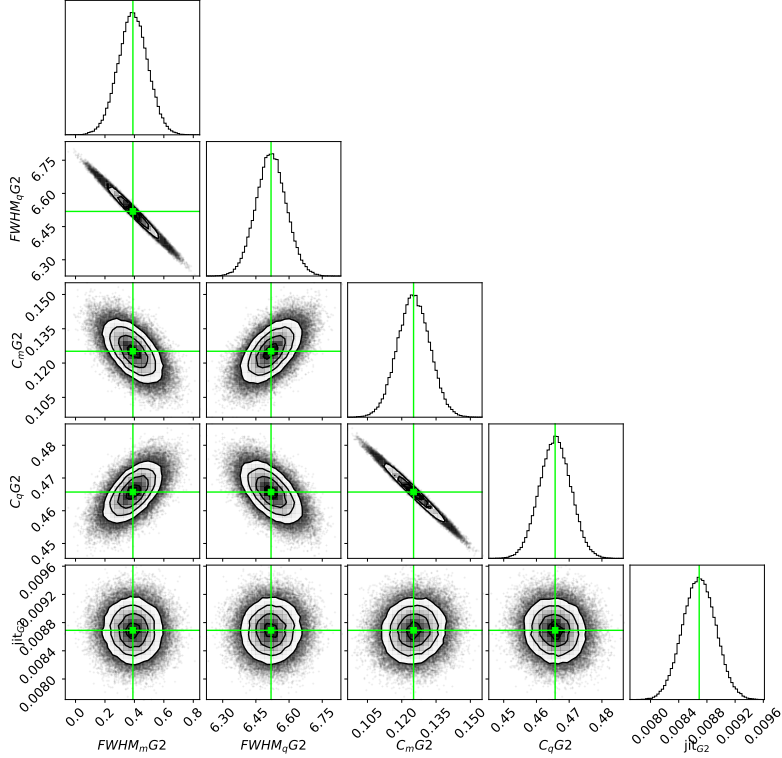


Figure 3.10: This figure shows an example of the corner plot obtained using the results of the MCMC fit on the slope and intercept of the contrast and of the FWHM of the stellar lines obtained with the G2 filtering mask.

which are reported in Table 3.3, are instead well constrained and show almost no differences in the three analysis. This is telling that the information of the stellar profile is mostly contained in the value of the centroid, which is expression of the radial velocity, and few information is extracted from the depth (Contrast) and the width (FWHM) of the stellar spectral line. I display in Figure 3.10 an example of the corner plot that I have obtained using these values. From the diagonal, is clear that the fitted parameters follow a Gaussian distribution, and in the other panels is also possible to see the linear correlation between the slope and the intercept of both the quantities.

4

Dataset

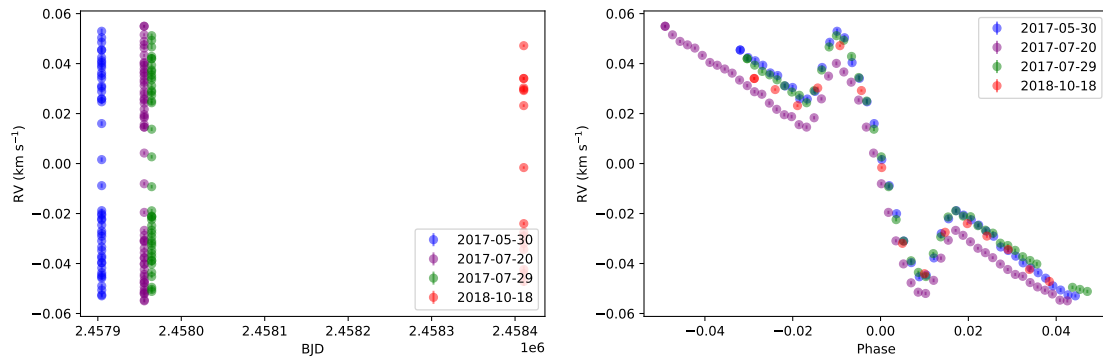
In this chapter I present all the dataset that I used to perform my analysis. In particular, in the modelling I included eight in-transit spectroscopic time series (Section 4.1 and Section 4.2), photometric data spanning over fifteen years, taken both from TESS archive (Section 4.3) and from literature (Section 4.5), and high precision radial velocity data from the literature (Section 4.4), in a robust and reliable Bayesian framework. In each of the following section I provide a description on how I obtained the data and how I prepared them to be used for the modelling, of which I provide more information in Section 4.7. Section 4.6 is instead dedicated to the Limb Darkening coefficients.

4.1 HARPS OBSERVATIONAL DATA

In order to resolve the stellar surface using the transiting planet, my target needed to be bright, with an high value of signal-to-noise (S/N), and the observation must be carried out with an highly stabilised spectrograph. The star HD189733 was a good choice for this purpose, since there were available archival observations from the High-Accuracy Radial-velocity Planet Searcher (HARPS) echelle spectrograph mounted on the ESO 3.6m telescope in La Silla, Chile. The dataset is composed by four nights of data collected in 2006, during the observations of July 29/30 and September 7/8, and in 2007 during the observation of July 19/20 and August 28/29. I have already provided information about these data at the beginning of Chapter 2, where I have reported Table 2.1 with the details.

4.2 NEW HARPS-N DATA

In my analysis I have also included **unpublished** spectroscopic time series over four nights of observations obtained in the context of the Global Architecture for Planetary Systems (GAPS) program, using the High Accuracy Radial velocity Planet Searcher for the Northern hemisphere (HARPS-N). HARPS-N is an high-resolution optical spectrograph dedicated to exoplanet search and optimized for high-precision radial-velocity measurement, installed at the Italian Telescopio Nazionale Galileo (TNG), which is a 3.58m telescope located at the Roque de los Muchachos Observatory on the island of La Palma in Canary Islands. A description of



(a) Radial velocities values as a function of time.

(b) Radial velocities values as a function of phase.

Figure 4.1: These plots display the HARPS-N dataset. Figure 4.1a is the plot of the RV in km/s, as a function of the time stamps in BJD, while Figure 4.1b is the plot of the same RV as a function of the orbital phase, computed starting from the time in BJD.

the HARPS-N spectroscopic dataset related to my target star HD189733 can be found in Table 4.1, where I have provided information on the night of the observations, on the number of spectra collected, on the mask that have been used and on the exposure time. Since these are

Table 4.1: HARPS-N data on HD189733

Night	Spectra	Mask	t_{exp} [s]
2017-05-30	46	K5	300
2017-07-20	55	K5	300
2017-07-29	43	K5	300
2018-10-18	15	K5	900

private data that belong to the GAPS team, which used them in the study of the exoplanetary

atmosphere, my work on them to study the RM effect and the results that I have obtained applying also the RRM and the RMR methods are the first of their kind. In Figure 4.1 I provided two plots where I have visualised the 4 radial velocity curves related to the HARPS-N dataset. To obtain these plots I displayed the RV values both as a function of the time stamps in BJD, in Figure 4.1a, and as a function of the orbital phase, in Figure 4.1b.

4.3 TESS DATA

The Transiting Exoplanet Survey Satellite (TESS) was launched in April 2018. It is a NASA mission that was designed to spend two years discovering transiting exoplanets through an all-sky survey. The mission duration has been extended by other two years and probably it will go on searching for exoplanets also in the next years. TESS has four identical, highly optimized, red-sensitive, wide-field cameras that together can monitor a $24^\circ \times 96^\circ$ strip of the sky (called *sector*). The field-of-view is oriented along a line of ecliptic longitude with the instrument generally pointing at $\pm 54^\circ$ of ecliptic latitude, which makes Camera 4 being centered on an ecliptic pole. In this way sectors overlap near the ecliptic pole and so a given star may be observed by several sectors. By monitoring each sector for 27 days and nights, TESS covered the southern hemisphere sky during the first year of the mission and the northern hemisphere in the second year. Then, since the mission got extended, it started re-observing both the southern (already completed) and the northern hemisphere sky. The set of TESS data products is made of 30/10-min cadence Full-Frame Images (FFI) and 2-min cadence postage stamps for about 200,000 pre-selected targets. Indeed the team prepared the TESS Input Catalogue (TIC) of over 1 billion objects and a special subset Candidate Target List (CTL) of 200,000 objects for the short-cadence observations. This was done because taking images every 30 or 10 min is not a good choice for the light curve sampling, since we can have the so called *binning effect*¹. Given

Table 4.2: ExoFOP information on HD189733.

TIC ID	256364928
Sectors	41, 54
T_{tr} (d)	2459770.4104(21 \pm 34)
P (d)	2.218574(80 \pm 18)

the fact that they only have a limited amount of data that can be downloaded from the satellite,

¹When a light curve is observed, the variation of the transit have timescales of a few minutes, thus integrating an image over half an hour can smooth out all the features of the light curve itself.

the TESS team selected a special sample of targets (usually bright stars or stars which are already known to have some planets) and they decided to download only a small portion of the image around the target (these are the so called Target Pixel Files) measuring the flux of the observed star every 2 min, to better determine the shape of the transit. To download the data related to my target HD189733, I initially retrieved its TESS Input Catalogue number and the sector in which it has been observed, from the ExoFOP website². I got information on the TIC ID, the sectors of TESS, the reference time of the first transit (detected in the TESS light curve) and the period of the planet, which I reported in the Table 4.2. I then used the official archive for NASA missions data products, that is the Mikulski Archive for Space Telescopes (MAST³), in order to download the TESS Target Pixel File (TPF) related to my star. Once I entered the TIC number and selected the TESS mission data products, I got many results. Since HD189733 has been observed in 2021 in sector 41 and in 2022 in sector 54, I found two sets of science data, each containing five files. Among these files I used only the ones with suffix `_lc.fits`, containing the light curves as extracted by the TESS team. More information on these TESS data are reported in Table 4.3.

Table 4.3: TESS data on HD189733

Sector	Data points	Start time	End time	Filter	Waveband
s41	19149	2021-07-24	2021-08-20	TESS	Optical
s54	18890	2022-07-09	2022-08-04	TESS	Optical

4.3.1 TESS ANALYSIS

Since the TESS team have already reduced the data, I did not perform the aperture photometry on the TPF, but I used the light curves provided by them. In particular, they not only have provided all the data, but they have also performed the data reduction with both a Simple Aperture Photometry (SAP), and a Pre-search Data Conditioned Simple Aperture Photometry (PDCSAP), which is the SAP after correcting for instrumental systematics as possible changes in the detector efficiency and any other long term trends. As first step I wrote a Python script to load the light curve `.fits` files and to open their Header/Data Units (HDU). The HDU contained three entries: `PRIMARY`, `LIGHTCURVE` and `APERTURE`. I extracted the data from the `LIGHTCURVE` HDU and found the keywords contained in it. In particular I was interested

²<https://exofop.ipac.caltech.edu/tess/>

³<https://mast.stsci.edu/portal/Mashup/Clients/Mast/Portal.html>

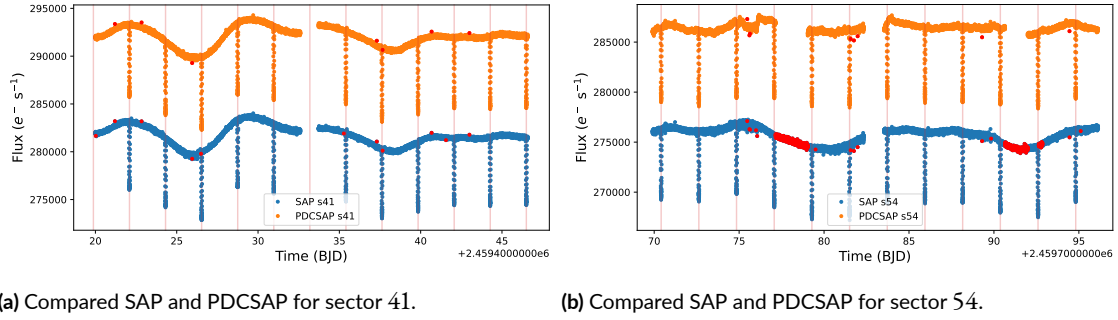
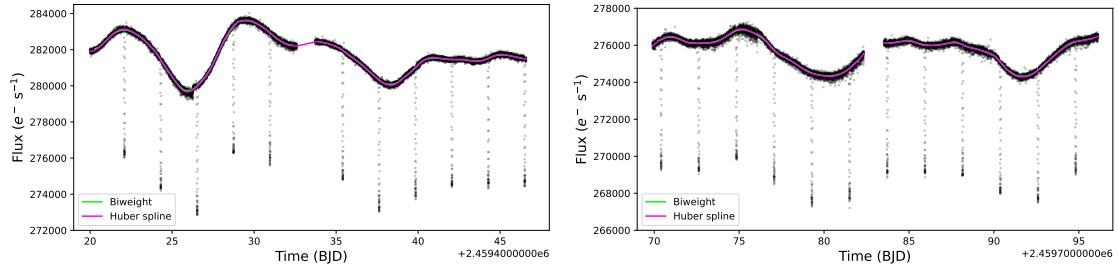


Figure 4.2: These plots display the comparison between the SAP (cyan points) and PDCSAP (orange points) analysis performed by the TESS team with the data corresponding to sector 41 (left) and data corresponding to sector 54 (right).

in the flux of the SAP, the flux of the PDCSAP and the error associated to them, so I selected them using the correct keyword. The PDCSAP fluxes should be in principle best estimate of the intrinsic variability of the target, since they are obtained after correcting for systematics that are usually quantified studying common trends relative to all the stars that fall in the surroundings of the considered target. This is a general approach to correct the data for systematics, but it may not work in some specific cases. In order to check if the applied correction has been successful or not, I decided to compare the PDCSAP with the SAP analysis. For this aim, together with the SAP, PDCSAP flux and associated errors, I also extracted the time stamps and the quality flag of the data, as determined by the TESS team. For my analysis, I have decided to keep only the points with quality flag equal to zero, i.e., data points that are not affected by any instrumental anomalies or astrophysical effects. To provide a visual feedback of the comparison, in Figure 4.2 I plotted the flux values of the two analysis as a function of time, using different color in the two cases and highlighting the bad data in red. The two analysis are almost identical in the case of sector 41, while they show some differences in sector 54, where the PDCSAP algorithm seems to have encountered some problem. For this reason I decided to consider the SAP as best analysis in both sectors and I saved in a file only the values that I flagged as very good data for the time stamps, for the flux of the SAP and for its corresponding error. From the plots in Figure 4.2 it is easy to see that the flux is not normalised and that the light curves have some trends. These trends can be caused by some residual instrumental systematic error or by any other source of spurious signal different from the one of the planetary transit, like stellar activity. Indeed, the presence of a star spot can mimic the transit signal by causing a reduction on the measured flux, while the presence of a flare causes an increase of the flux and the modulation of these different signals is part of the observed trend in the light curve. For this reason, if I want to fit the actual transit signal, I need to remove these trends



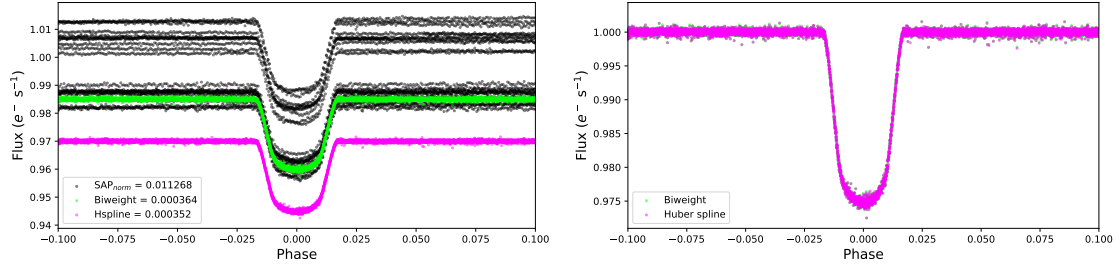
(a) Fit on the SAP data of sector 41.

(b) Fit on the SAP data of sector 54.

Figure 4.3: These plots display, with different colors, the results of the fit performed by `wotan` on the SAP flux data with both the biweight (lime) and the `hspline` (magenta) averaging methods.

and normalise the light curve in a way that the flux is equal to 1 outside the transit and assumes a value smaller than 1 only during the transit. To perform this operation, which is called *light curve flattening*, I followed a quite empirical approach with no assumption on the cause of the signal modulation, by modelling the light curve outside of the transit in order to get the normalised flux. To perform this operation I took advantage of the already implemented and tested code `wotan`⁴, developed by Hippke et al. in 2019[7], in order to get a proper correction of the light curve preserving the shape of the transit itself. This code selects the data using two windows, one along the x-axis, called temporal window, and one along the y-axis, which selects only those points that are located within a given vertical distance from the average of the points previously computed, within the temporal window. In practice, `wotan` takes a chunk of the light curve, computes the average, and then re-computes its value inside the temporal window by weighting the selected points according to the distance in flux with respect to the average value previously calculated. In this way, during the operation of flattening of the light curve I give much less weight to the points that are associated to the transit signal, hence preserving the characteristics of the transit itself. I gave as input to `wotan` the file associated to the SAP data flagged as very good, that I previously saved, and I decided to test two different algorithms to compute the average: the so called *Tukey's biweight* and the *Huber's spline*. Both of these algorithms required the assignment of a value for several parameters, which are: `WINDOWS LENGHT`, the length of the filter window in units of time; `EDGE CUTOFF`, since trends near the edges are less robust, depending on the data, it may be beneficial to remove the edges; `BREAK TOLERANCE`, if there are large gaps in time, especially with corresponding flux level offsets, the flattening is much improved when splitting the data into several sub-light curves and applying the filter to each individually; `RETURN TREND`, if `True`, the method will return a tuple of two el-

⁴This code can be retrieved from the github repository <https://github.com/hippke/wotan>



(a) Comparison of all the folded light curves. (b) Compared biweight and hspline methods.

Figure 4.4: Right: Plot of the folded light curves obtained by slightly shifting the value of the flux, for visualisation purpose. Here are compared all the SAP light curves, coloured in black, with the biweight (lime) and the hspline (magenta). Left: This plot shows how the two flattened light curves, obtained with the biweight and with the hspline methods, are practically overlapping, even if $\sigma_{Biweight}$ is slightly larger than $\sigma_{Hspline}$.

ements (flattened flux, trend flux), where trend flux is the removed trend, otherwise it will only return flattened flux; `CVAL`, tuning parameter for the robust estimators. In Table 4.4 I reported the values of each of the parameters that I used to run the two algorithms and to provide also a visual feedback of the results obtained with `wotan`, in Figure 4.4 I plotted the trends identified by both the biweight and the hspline methods onto my SAP flux data. Since I wanted to display

Table 4.4: Parameters for the two algorithms used in the `wotan` code.

Method	biweight	spline
window length (d)	1.0	0.5
edge cutoff	0.3	/
break tolerance	0.5	0.5
return trend	True	True
cval	0.5	1.5

the light curve as a function of the orbital phase, I had to perform the *folding* of the light curve, a process in which all the points that correspond to the same moment of the transit are overlapped, a planetary orbit after the other, in order to superimpose all the recurring transits. First I computed the phase, using the reference time of the first transit and the period of the planet, reported in Table 4.2, in a way that the transit is centered in zero. Then I divided the SAP flux values by an average value computed on the out-of transit points, in order to normalise the light curve. Finally, to compare the normalised SAP curves with the biweight and the hspline flattened light curves, I plotted them together in Figure 4.4a. In order to quantitatively compare the light curves, I selected a range of the orbital phase outside of the transit not too far from

it, and I computed the standard deviation of the points inside that range, finding that: $\sigma_{SAP} = 0.011268$, $\sigma_{Biweight} = 0.000364$ and $\sigma_{Hspline} = 0.000352$. The largest standard deviation is that produced by the SAP light curve, while both the flattened ones produce a small σ , which is comparable between them two, as can be seen in the plot of Figure 4.4b, but is slightly smaller in the case of the Huber spline method. As a consequence, I decided to retain the Huber spline flattened light curve and saved it into a file, after computing the error associated to these data, as the ratio between the error associated to the input light curve and the modelled trend derived with the Huber spline method, which I assumed to be error-less.

4.4 LITERATURE RADIAL VELOCITY DATA

Aiming to get a new estimate of the mass of HD189733b, I also performed a spectroscopic analysis of radial velocities, as is usually done in the RV technique. The concept on which this technique is based is very simple. A star and a planet which form a system are both orbiting around the common center of mass, which is the barycenter of the system. Since the planet is too faint, what is detected with the RV method is the motion of the star induced by the presence of the planet. In particular, during its orbit around the barycenter, the velocity of the star has a radial component which is oriented along the line of sight. This radial component causes a Doppler effect in the emitted light of the star, which appears bluer as the star is moving toward the observer and redder as it moves in the opposite direction. Due to the Doppler effect, the spectral line of the star are periodically shifting from their rest position of an amount which, if quantified, allows to detect the presence of a planet. This indeed was the technique that led Bouchy and his collaborators to discover the exoplanet HD189733b in 2005 [8]. From the observation of the orbital motion of the star around the barycenter it is possible to obtain the characteristics of the planet. In particular, if the eccentricity of the planet is zero, the star describes a perfect sinusoidal motion and it is possible to determine the value K of the semi-amplitude of the RV curve fitting the data even with few points. The mass of the planet (M_p) can then be derived from the value of K , given that the mass of the star is known. What is actually derived is not M_p , but the lower limit mass $M_p \sin i_p$, but since HD189733b is also transiting in front of its host star, than the value of the orbital inclination is known, hence the true mass of the planet can be determined.

In order to perform this kind of analysis I did not get any new RV measurements, but I used literature data taken from previous analysis of this kind. To search for these data, I used the

NASA Exoplanet Archive website⁵ and I found two papers cited in the ancillary information section related to the RV curves. Checking these papers, I found that in one of them the authors were using data taken from the discovery paper, and the same HARPS data on which I performed my analysis. Then I decided to take the RV data directly from the discovery paper. In Table 4.5 I have summarised the sample of RV data that I have used to perform my analysis, which are literature data taken from the discovery paper of Bouchy et al. 2005[8], from the paper of Winn and collaborators published in 2006[9], and from the paper of 2009 by Boisse and collaborators[10]. In both the cases of Bouchy[8] and Winn[9], data also contain RV measurements taken during the transit, which the authors used to performed an analysis of the RM effect with the classical method.

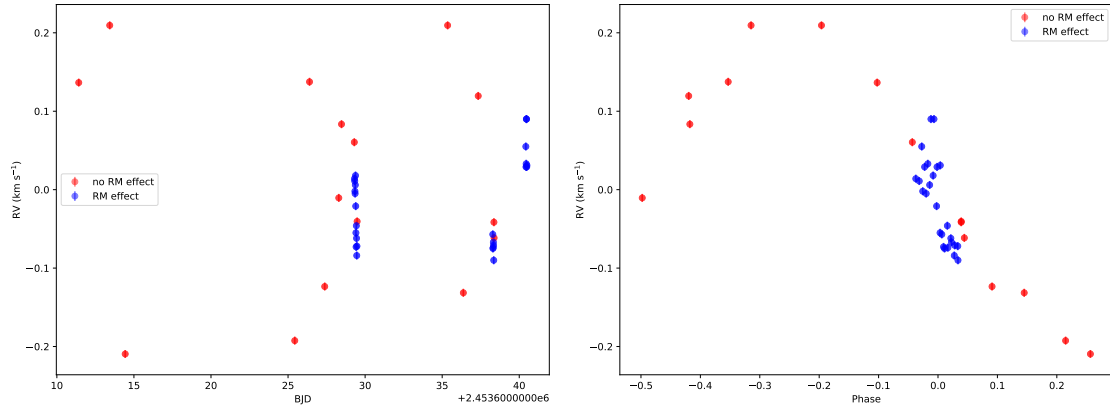
Table 4.5: Literature RV data on HD189733

Paper	Data points	Excluding RM	Including RM	Mask
Bouchy 2005	47	15	26	R37000K0
Winn 2006	86	26	58	Optical Spectra
Boisse 2009	33	33	/	G2

4.4.1 LITERATURE RADIAL VELOCITY ANALYSIS

From the discovery paper of Bouchy et al. 2005[8] I found the information that the spectroscopic observations of HD189733 have been carried out in March 2004 with the ELODIE spectrograph mounted on the 1.93 m telescope at the Haute-Provence Observatory (OHP) in France. Using this information, I searched in the online available archive of ELODIE and found the same spectroscopic data on which the authors performed their analysis. After saving them, I wrote a Python script to see their content. In particular, since they were file `.fits`, I opened them with `astropy` and checked the information reported in the header. Among the information, I found five different values associated to the keyword `TIME`, numbered from 1 to 5, of which `TIME4` corresponded to the time of mid exposure, and `TIME5` to the exposure time in seconds. I noticed that in writing this files the science team had used the UTC time scale. For this reason I had to convert them to the appropriate scale, which is the Barycentric Julian Date (BJD), which takes also into account of the time required to the light to travel the distance between the heliocentric and the barycentric position of the Solar System. To perform

⁵<https://exoplanetarchive.ipac.caltech.edu/>



(a) Bouchy's RVs as function of time.

(b) Bouchy's RVs as function of phase.

Figure 4.5: In these plots are displayed the RVs values taken from Bouchy et al. 2005[8] as a function of the time in BJD in Figure 4.5a and as a function of the orbital phase in Figure 4.5b. Different colors are used in both cases to distinguish where the RM effect is present.

the conversion between the two time scales I took advantage of the functions already implemented in the `astropy` module, to which I gave as input the UTC time, together with the sky coordinates of my target star, and the Earth location of the observatory. After this operation, I computed the orbital phase starting from the time values in BJD, and I used it to define the interval inside of which the RV measures were including the RM effect. I then saved the RVs in two distinct files, one for those with the RM effect and one for those not including it. In Figure 4.5a I have displayed with different colors the RVs as a function of the time stamps in BJD and in Figure 4.5b as a function of the orbital phase. From my selection I found that among the 47 total RV data points of this set, 26 were also including the RM effect, 15 were excluding it and the remaining 6 were bad data, that I decided not to include in the further steps of my analysis. This information is reported in Table 4.5.

In the paper of Winn et al. 2006[9] the authors explain that the observations were carried out during the predicted transit of 21 August 2006, using the High Resolution Echelle Spectrometer (HIRES) mounted on the 10m telescope Keck I. They obtained 70 spectra in an interval of time of 7.5 hours, getting measurements also before and after the transit. To these they added other 16 spectra that had been obtained by the California-Carnegie group at random orbital phases. The entire dataset on which they performed their analysis was reported in a table, so in this case I did not need to search for the data. The values of time they reported are expressed in the Heliocentric Julian Date (HJD) scale, so before I could use them to compute the orbital phase I had to convert them into the BJD, using again the functions implemented in `astropy`.

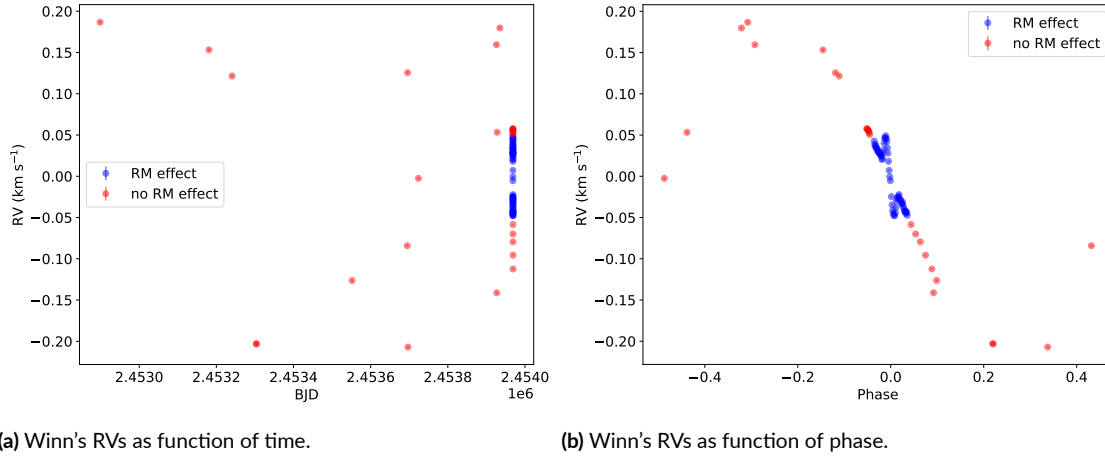
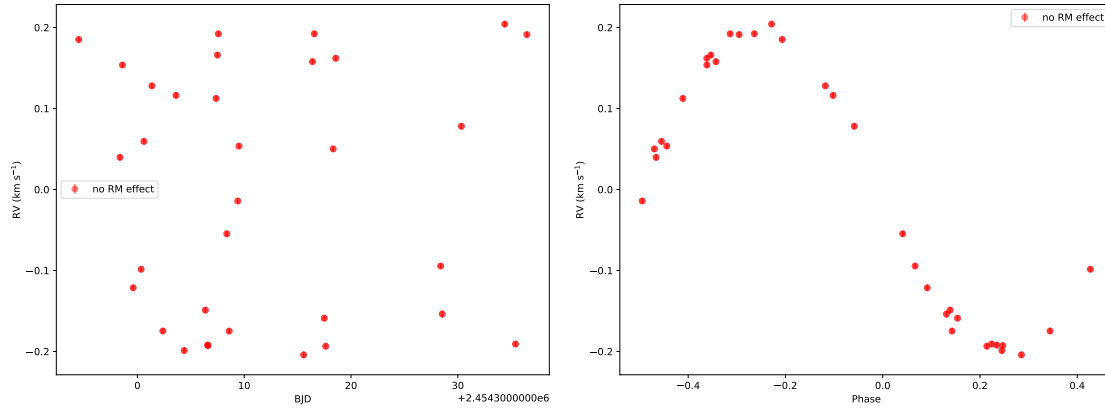


Figure 4.6: In these plots are displayed the RVs values taken from Winn et al. 2006[9] as a function of the time in BJD in Figure 4.6a and as a function of the orbital phase in Figure 4.6b. Different colors are used in both cases to distinguish where the RM effect is present.

Using the properly computed orbital phase, I selected the RVs on the basis of including or not the RM effect and then I plotted them both as a function of time and as a function of the phase as shown in Figure 4.6. In particular, in Figure 4.6a is possible to distinguish also the 16 points corresponding to the spectra added to the dataset. Among the 86 total RVs data points, 2 were bad points that I had to discard, while the remaining, that I saved in two separate files to be used for the analysis, were divided in 58 which included the RM effect, and 26 not including it. I reported this information also in Table 4.5.

From the paper of Boisse et al. 2009[10] I found the information that the authors had obtained the RV measurements on which they performed the analysis, between 12 July 2007 and 23 August 2007. They carried out the observations with the high-resolution SOPHIE spectrograph, mounted on the 1.93 m telescope at the OHP in France. Also in this case I have been able to get the spectroscopic data from the online available archive of SOPHIE, using the information provided by the authors of the paper to search for them. I wrote a Python script to open the data after saving them, as I did for the RVs of ELODIE. These were files `.fits`, so I opened the header to check the information contained in them and found that the values of time were reported in the UTC TBD scale. In order to convert the values of time to the BJD scale I used `astropy` and then I proceeded as before in computing the orbital phase and separating the RVs values on the basis of containing the RM effect or not. This time all of the 33 RV data points were not including the RM effect, as I also showed in the two plots of Figure 4.7, so I saved all of them in a single file, ready to be used for the analysis, as reported in Table 4.5.



(a) Boisse's RVs as function of time.

(b) Boisse's RVs as function of phase.

Figure 4.7: In these plots are displayed the RVs values taken from Boisse et al. 2009[10] as a function of the time in BJD in Figure 4.7a and as a function of the orbital phase in Figure 4.7b. No points associated to the RM effect are present.

4.5 LITERATURE LIGHT CURVE DATA

Soon after the discovery in 2005 of the exoplanet HD189733b through the RV technique, this planetary system has been analysed also with the photometric method, given that the planet has been proven to transit its host star. The idea behind this technique, also called transit photometry, is to detect the drop of the observed brightness of a star, caused by a planet transiting in front of it, through photometric observations. The fractional drop in the stellar flux (δ) is proportional to the ratio of the surfaces of the two bodies (R_p^2/R_\star^2), therefore it is easier to detect it when the planet has a larger radius and the star is a dwarf. The main advantage of this technique is that it allows to get an estimate of the radius of the planet. The problem is that a planet can be observed transiting its host star only if its orbit is almost aligned with the line of sight of the observer on Earth, so it is necessary to observe a very large number of stars in order to increase the probability to detect it. This method has also an high rate of false detection, since many stellar effects can mimic the effect of a planetary transit. This fortunately is not the case of HD189733b, which presence has been well confirmed by multiple observations with both spectroscopy and photometry. By modelling a theoretical light curve of a star with a transiting exoplanet it is possible to retrieve many information about the planetary system as the transit duration, the orbital period of the planet and the ratio between the radius of the two bodies. In addition, by monitoring for a sufficiently long time span the orbit of the same planet with photometry, it is also possible to calculate new ephemerides, and estimate the timing offsets of the distinct transits with respect to the predictions of a constant orbital period, which can be

used to reveal the eventual presence of additional planets in the system.

In order to perform this kind of analysis I did not get new photometric observations, but I used literature data taken from previous analysis of this kind. To search for these data, I have consulted the NASA Exoplanet Archive website⁵, where in the ancillary information section related to the photometric light curves I found many results. I decided not to include in my analysis amateur light curves, since no information were provided on the method adopted to obtain them. I also excluded light curves obtained through observations carried out with other space telescopes, because treating those data would have required specific programs, making the analysis become more complicated. So the only light curves that I included in my sample, which I reported in Table 4.6, are those taken from the papers of Bakos et al. 2006[11], and Winn et al. 2007[12].

Table 4.6: Literature light curve data on HD189733

Paper	Light Curves	Used ⁶ .
Bakos 2006	15	11
Winn 2007	8	8

4.5.1 LITERATURE LIGHT CURVE ANALYSIS

Bakos et al. 2006[11] have organized an extensive observing campaign with the goal of acquiring multi-band photometric measurements of the transit of HD189733b. In the paper they have reported a table with all the information regarding the instruments used to carry out the observations, which in this case are seven telescopes on four different sites spread in geographic longitude. This was done in order to collect a large number of individual data points in a time span of two months. The telescopes which were involved in the photometric monitoring are the 1.0m telescope at the Wise Observatory in Israel; the 1.2m telescope at OHP; the 1.2m telescope at the Fred Lawrence Whipple Observatory (FLWO) of the Smithsonian Astrophysical Observatory (SAO); the 0.11m HAT-5 and HAT-6 wide-field telescopes plus the 0.26m TopHAT telescope, also at FLWO; and the 0.11m HAT-9 telescope at the Submillimeter Array site at Mauna Kea in Hawaii. Following the indication provided by the authors, I searched online and found all the data of their analysis. Since data were collected with different instruments, at different locations and using also different filters, I had to treat each of the light curves

⁶Since not all of the light curves that are reported in the paper contain a sufficient portion of the transit, I decided to use only the ones containing at least half of it. I explain this in Subsection 4.5.1

separately. I wrote a Python script to open the files containing the header information and I found that the photometric measurements were expressed in magnitudes and that the time stamps were reported in the Heliocentric Julian Date (HJD) scale. The first thing that I had to do was to convert the values of time in the BJD scale and to do that I used the `astropy` functions, to which I give as input the HJD values and also the keyword of the observatory location, which was reported in the header of the files as `OBSERVATORY_SITE`. Then I had to convert the magnitude values in flux. To do this I used the simple equation

$$F = 10^{-0.4m}, \quad (4.1)$$

where F is the flux and m the value of magnitude that was reported in the files. Obviously, together with the magnitudes I also had to convert in flux units the errors associated to them. To do that, I first defined an upper (ε_{up}) and a lower (ε_{low}) value of the error, respectively as $\varepsilon_{up} = F \cdot (10^{0.4\sigma_m} - 1)$ and $\varepsilon_{low} = F \cdot (1 - 10^{-0.4\sigma_m})$. I have computed then the average of them, and used the resulting value as error associated to the measures of flux:

$$\sigma_F = \frac{\varepsilon_{up} + \varepsilon_{low}}{2}. \quad (4.2)$$

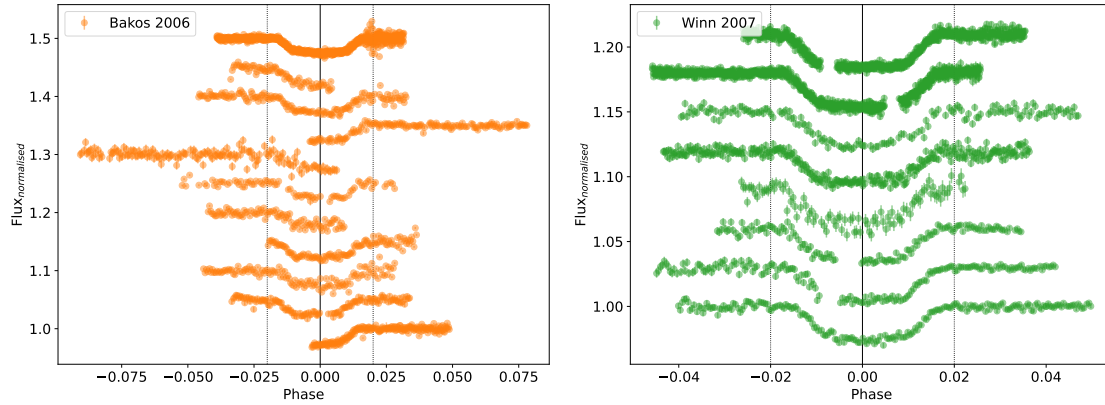
With the data converted in convenient units, I displayed each light curve by plotting the nor-

Table 4.7: Light curve taken from the dataset of Bakos et al. 2006[11].

Night	Telescope	Filter ⁷	Cadence (s)	Data points
2005-09-15	OHP 1.2m	B	86	128
2005-09-24	Wise 1.0m	B	42	201
2005-09-24	OHP 1.2m	R _C	95	159
2005-09-26	OHP 1.2m	R _C	95	142
2005-09-29	HAT-6	I _C	108	126
2005-09-29	FLWO 1.2m	r _{Sloan}	17	810
2005-09-29	HAT-5	I _C	135	83
2005-09-29	TopHAT	V	70	79
2005-10-01	HAT-9	I _C	99	96
2005-10-28	TopHAT	V	106	159
2005-11-19	HAT-9	I _C	90	115

malised flux as a function of the time stamps. To better compare the different light curves I have

⁷The B and V filters are those of the Johnson system, I_C and R_C filters belong to the Cousins system, while the r_{Sloan} is a filter from the Sloan Digital Sky Survey (SDSS) photometric system.



(a) Light curves from Bakos et al. 2006.

(b) Light curves from Winn et al. 2007.

Figure 4.8: Light curves taken from literature on which the photometric analysis has been conducted. In both cases, the values of the normalised fluxes are plotted as a function of the orbital phase, in a way that the center of the transit corresponds to $\varphi=0$. The vertical black line gives the position of the center of the transit, while the two vertical dashed lines provide a visual indication of the interval of phase inside of which the transit is observed.

normalised the flux values, by computing the ratio between the measured flux and the average of the continuum, which I selected in the flat part of the light curves. What I observed in these plots was that not all the light curves included a sufficient portion of the transit, that could be used in the next steps of the analysis, and in the majority of them the transit was only partially detected. For this reason I decided to keep only the light curves that were including at least half of the transit, hence restricting my dataset to 11 of the original 15 light curves. I reported in Table 4.7 the information related to the dataset on which I conducted my analysis and I displayed the corresponding light curves all together in Figure 4.8a, to give also a visual feedback. In particular, to produce this plot I computed the orbital phase, starting from the values of time in BJD, and I added a small offset to the values of the flux of the different light curves, for visualisation purpose, in order to avoid any overlapping. I then saved each of them in a file `.dat` reporting in columns the values of time in BJD, the normalised flux in electrons per second, and the associated error.

On the footsteps of Bakos and collaborators, Winn et al. performed another photometric analysis of HD109733b in 2007[12]. To do that, they used observation collected in 2005 and 2006 by telescopes at four different observatories. They collected photometric measurements with the 1.2m telescope at the Fred L. Whipple Observatory (FLWO) on Mount Hopkins in Arizona; they used the T10 0.8m automated photometric telescope (APT) at Fairborn Observatory, in Arizona; with the 2m telescope at the Multicolor Active Galactic Nuclei Monitoring

(MAGNUM) observatory on Haleakala, in Hawaii, they photometrically observed the same transit that was observed spectroscopically by Winn et al. in 2006[9]; and they used also the 1.0m telescope at Wise Observatory, in Israel. In total, they gathered photometric observations of 8 different transits of which they provided a clear description in the paper. Following their description, I have been able to find the complete dataset on which they performed their analysis. After saving them, I opened the header of these data and found the information that the

Table 4.8: Light curve taken from the dataset of Winn et al. 2007[12].

Night	Telescope	Filter ⁸	Cadence (s)	Data points
2005-09-28	T10 APT 0.8m	(b + y)/2	86.4	202
2006-05-02	T10 APT 0.8m	(b + y)/2	86.4	178
2006-05-22	T10 APT 0.8m	(b + y)/2	86.4	134
2006-06-11	T10 APT 0.8m	(b + y)/2	78.0	97
2006-07-21	FLWO 1.2m	z_{Sloan}	13.8	910
2006-08-21	MAGNUM 2.0m	V	82.8	168
2006-09-05	Wise 1.0m	I_C	43.8	344
2006-09-10	FLWO 1.2m	z_{Sloan}	13.8	752

photometric measurements were reported in flux units and the values of time were expressed in the HJD scale. Also in this case I had to treat each of the file separately, so I wrote a Python script and used `astropy` functions to convert the time in BJD, taking into account the information on the location of the observatory which I found in the header, reported with the keyword `OBSERVATORY_SITE`. Then, as I did with the light curves of Bakos et al. 2006, I displayed each of them by plotting the flux as a function of the time stamps. In this case, as the authors said in the paper, all the 8 light curves contained a complete transit, so I saved each of them in a file, after having normalised the flux values. To perform the normalisation, I computed the ratio between the measured flux and the average value of the continuum, determined from the flat part of the light curve, as before. In Table 4.8 I reported the information on the dataset on which I conducted my analysis, which is the same as the one in literature. To visualise the light curves, I first computed the orbital phase using the values of time in BJD, and then I plotted the normalised flux values as a function of it. In Figure 4.8b I displayed the light curves of Winn et al. 2007 all together in the same plot, adding an increasing offset to the values of the flux for visualisation purpose only, to avoid any overlapping.

⁸The (b+y)/2 filter is a special combination of two separate differential magnitudes from the Stromgren system, used to improve the photometric precision. The V and I_C filters belong to the Johnson and Cousins photometric system, while z_{Sloan} is taken from the SDSS system.

4.6 LIMB DARKENING COEFFICIENTS

One of the aspect that I needed to keep into account, before to perform the modelling of the data, was the Limb Darkening (LD). Considering that my dataset is composed by both photometric and spectroscopic measurements obtained with different instruments, using different filters, I had to compute the correct coefficients for the LD. In particular, to be consistent with the previous analysis that I described in Chapter 2 and Chapter 3, I decided to use a quadratic law for the LD, for which I needed to determine the two coefficients to be used. To do this I took advantage of PyLDTk⁹, the Python toolkit for calculating the stellar LD profiles and model specific coefficients for arbitrary pass-bands using the stellar spectrum model library by Husser et al. 2013[13], implemented by Hannu Parviainen in 2015⁹. I reported in Table 4.9 the results obtained with PyLDTk, providing for each filter both LD c_1 and LD c_2 , which are the coefficients for the quadratic LD law. In Figure 4.9 I plotted the filters that I used in

Table 4.9: Stellar Limb Darkening coefficients obtained with PyLDTk.

Filter	LD c_1	LD c_2
r_{Sloan}	0.5825 ± 0.0178	0.1230 ± 0.0438
z_{Sloan}	0.4015 ± 0.0113	0.1268 ± 0.0310
V	0.6608 ± 0.0203	0.0972 ± 0.0458
B	0.8460 ± 0.0269	0.0032 ± 0.0489
I_C	0.4548 ± 0.0132	0.1270 ± 0.0363
R_C	0.5584 ± 0.0172	0.1249 ± 0.0431
TESS	0.4657 ± 0.0134	0.1273 ± 0.0356
HARPS-N	0.6746 ± 0.0198	0.0854 ± 0.0438

PyLDTk to determine the LD coefficients, using different colors for visualisation purpose only. I note that the errors are brutally underestimated, as they do not take into account possible differences between filters at different telescope, and error in the theoretical model atmospheres. For this reason, in the model I decided to arbitrarily assign an error of ± 0.05 to the derived values and use a Gaussian prior for these parameters. I also note that in Table 4.9 I did not include the filter (b+y)/2 of the Stromgren photometric system, since it is a composed filter, and the estimates of the LD coefficients for this kind of filter were not reliable. Therefore, I gave its coefficients as free parameters to the model, using a Uniform prior for them. Even if from

⁹ldtk: Limb Darkening Toolkit

<http://mnras.oxfordjournals.org/lookup/doi/10.1093/mnras/stv1857>

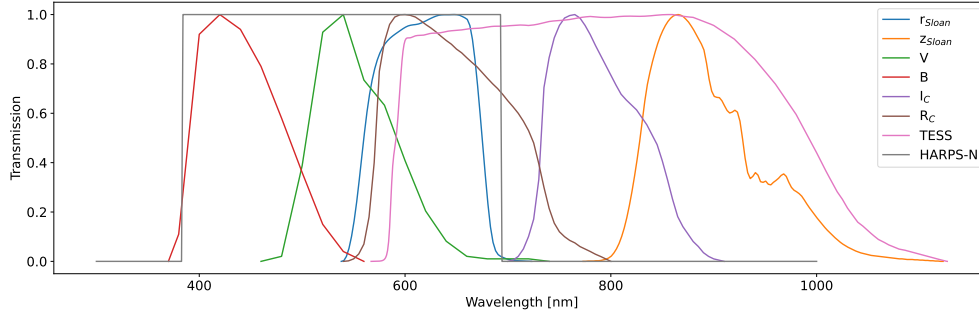


Figure 4.9: This figure represents the filters used in PyLDTk. The plot shows the transmission of each filter as a function of the wavelength.

PyLDTk I got an estimate for both the LD c_1 and the LD c_2 , for the TESS filter I decided to also use a Uniform prior, defined in the same intervals of those used for the Stromgren filters. In Table 4.10 I reported the LD coefficients and their prior.

Table 4.10: Stellar Limb Darkening coefficients given as priors to the model.

Filter	LD c_1	LD c_2	Prior
r_{Sloan}	0.58 ± 0.05	0.12 ± 0.05	Gaussian
z_{Sloan}	0.40 ± 0.05	0.13 ± 0.05	Gaussian
V	0.66 ± 0.05	0.10 ± 0.05	Gaussian
B	0.85 ± 0.05	0.00 ± 0.05	Gaussian
I_C	0.45 ± 0.05	0.13 ± 0.05	Gaussian
R_C	0.56 ± 0.05	0.13 ± 0.05	Gaussian
HARPS-N	0.67 ± 0.05	0.086 ± 0.05	Gaussian
$(b+y)/2$	[0.0, 1.0]	[-1.0, 1.0]	Uniform
TESS	[0.0, 1.0]	[-1.0, 1.0]	Uniform

4.7 MODELLING WITH PYORBIT

So far I have described how I have collected the data, gathering them from different archives and I have discussed how I have analysed the data and how I have decided which one to include in my dataset. In each of these cases, I have saved the selected data in a file `.dat`, ready to be used for the modelling. What I still have to explain is how I performed the modelling. In order to carry out the modelling in a robust and reliable Bayesian framework, I took advantage of PyORBIT¹⁰,

¹⁰PyORBIT code is available here: <https://github.com/LucaMalavolta/PyORBIT>

a publicly available code for exoplanet orbital parameters and stellar activity implemented by Malavolta et al. in 2016[14]. In particular, working on the PyORBIT code, there was an already implemented subroutine dedicated to the study of the Rossiter-McLaughlin effect with the classical method, described in the paper of Covino et al. 2013[15]. Hence I decided to also perform a modelling of my data using the already implemented RM classical method, since this analysis has never been applied on the dataset that I have presented here. Then I uploaded the codes that I have written to implement the RRM and the RMR techniques in the subroutines of the PyORBIT code, so that I could select them when providing the inputs related to the model that should be used by the code in order to study the RM effect.

In this way I have been able to perform three different modelling of the RM effect using the same dataset. To do that, I had to prepare the input `.yaml` files for PyORBIT specifying for each data: the name of the file; the kind, if photometric or spectroscopic; and the models to be used. In the case of the photometric data, in the model I have specified that I wanted to apply the quadratic limb darkening law, using for each filter the appropriate coefficients, (described in Section 4.6) and in the case of the light curves from the literature I have also included a normalization factor. For all the spectroscopic data I have specified that I wanted to use the radial velocity model, and for those where the effect was present, I selected also the model of the Rossiter-McLaughlin effect that I intended to use. This selection allowed me to produce the three different versions of the modelling, namely the standard RM, the Reloaded RM, and the RM Revolutions.

Then I had to give as input also the planetary and stellar parameters. For the planet I used a circular orbit model, specifying the boundaries on the orbital period, on the semi-amplitude of the RV curve, on the time of conjunction and on the eccentricity. For the star, instead, I set Gaussian priors on the mass, on the radius, on the density and on the rotation period.

Finally I fixed the length of the emcee chain to 10^5 steps, with a burn-in phase of 2×10^4 steps and I set the number of the walkers to 4 times the number of the parameters. The results of this analysis are presented in the next chapter.

5

Results

In this chapter I present the results obtained starting from the full dataset that I have described in Chapter 4. In Section 5.1 I discuss the results obtained using the Standard RM method, in Section 5.2 the results that I have obtained with the RRM and RMR analysis including both the differential rotation α and the convective contribution v_{conv} , in Section 5.3 I present the results of the RRM and RMR analysis performed again excluding α and v_{conv} from the fitted parameters, and in Section 5.4 I compare the results of the different analysis.

5.1 STANDARD ROSSITER-MCLAUGHLIN

As I have explained in the previous chapter, in the first analysis I have used the model of the standard RM effect already implemented in the PyORBIT code to fit my dataset. Since part of the data are not of public access and other are gathered from archives of different instruments, including for the first time the recently released light curves of TESS, this analysis can not only be useful to make a comparison with the other two techniques, but also provides new and accurate estimates for the parameters of the system. I report in Table 5.1 the parameters with relative best fit values, obtained as the median of the fitted distribution, and error associated to them, obtained as discrete difference between the median value and the 16 and 84 percentiles. I note that the estimated value of the radius of the planet that I have obtained starting from the light curves of TESS is the most accurate obtained so far. In Figure 5.1 I have displayed the distributions of the parameters obtained from the fit. As it can be seen, the histogram of the

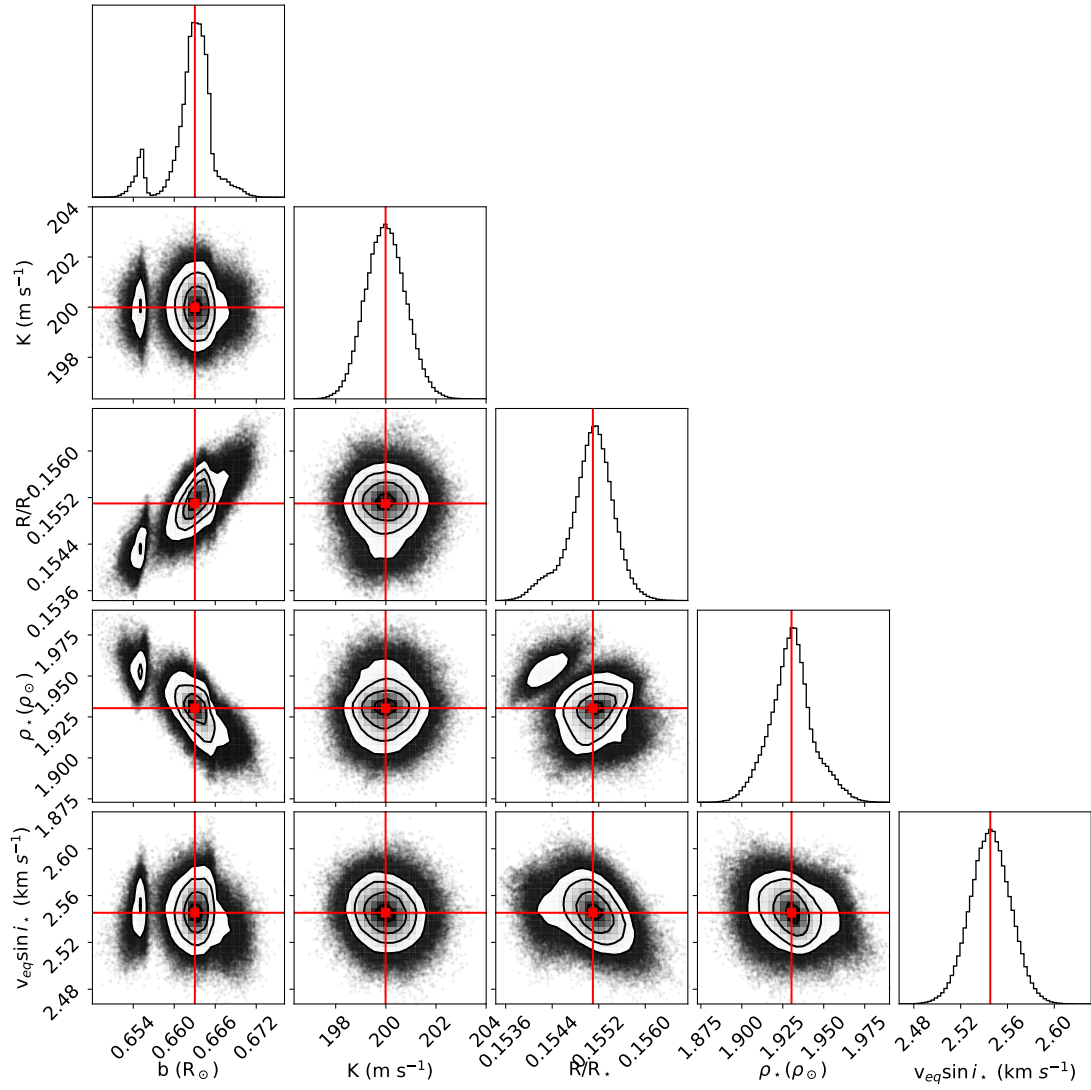


Figure 5.1: This is the corner plot obtained using the results of the fit with the standard RM method.

impact parameter b shows a double peaked shape, indicating that the fit has found two possible solutions, one of which is more probable. The histograms for the semi-amplitude of the RV curve and for the $v_{eq} \sin i_*$ have instead a well defined Gaussian shape, telling that these two parameters have been correctly fitted.

Table 5.1: MCMC observational results from the Standard RM analysis of the HD189733 system. Parameters that are preceded by * are the derived parameters obtained from the posteriors samples.

Parameter	Value	Units
$v_{eq} \sin i_*$	$2.55^{+0.02}_{-0.02}$	km s^{-1}
ρ_*	$1.930^{+0.012}_{-0.013}$	ρ_{\odot}
$ld_{C1,TESS}$	$0.480^{+0.045}_{-0.047}$	
$ld_{C2,TESS}$	$0.086^{+0.071}_{-0.066}$	
$ld_{C1,HARPSN}$	$0.260^{+0.034}_{-0.034}$	
$ld_{C2,HARPSN}$	$0.527^{+0.041}_{-0.040}$	
R_p	$0.1551^{+0.0003}_{-0.0004}$	R_*
λ	$0.02^{+0.22}_{-0.22}$	deg
b	$0.663^{+0.002}_{-0.003}$	R_*
K	$199.99^{+0.82}_{-0.79}$	m s^{-1}
T_C	$2459770.4104(51 \pm 13)$	d
P_p	$2.2185749(49 \pm 24)$	d
* a/R_*	$8.909^{+0.019}_{-0.020}$	
* i_p	$85.732^{+0.024}_{-0.020}$	deg
* M_p	$1.116^{+0.044}_{-0.045}$	M_J
* R_p	$1.141^{+0.027}_{-0.027}$	R_J

5.2 RELOADED AND REVOLUTIONS FIRST ANALYSIS

In this section I present the results that I have obtained applying the RRM and the RMR techniques. In performing these two analysis I have included in the fitted parameters both the differential rotation and the convective velocity contribution, as I have explained in Chapter 2 and Chapter 3, where I have described how I have implemented these two techniques. In Table 5.2 and in Table 5.3 I have reported the MCMC results that I have obtained from the two analysis. I have decided to split them in two separate tables, the first of which reports the parameters that are more specifically related to the analysis of the RM effect, including also the derived true 3D spin-orbit angle, while the second reports other parameters that have been fitted by PyORBIT, including some derived planetary parameters obtained from the posteriors

samples. The parameters that I have reported in Table 5.2 assume different values in the two

Table 5.2: MCMC observational results for HD189733 and the derived 3D spin-orbit obliquity. First row is for the Reloaded RM and second row is for the RM Revolutions. The two coefficients c_1 and c_2 here reported are those of the second order polynomial that have been used to fit the convective velocity contribution.

v_{eq} (km s ⁻¹)	i_* (°)	α	λ (°)	c_1 (km s ⁻¹)	c_2 (km s ⁻¹)	ψ (°)
$3.88^{+0.16}_{-0.28}$	$72.88^{+24.06}_{-12.88}$	$0.69^{+0.25}_{-0.49}$	$-4.48^{+0.86}_{-0.81}$	$4.76^{+0.18}_{-0.31}$	$-3.87^{+0.31}_{-0.21}$	$17.41^{+10.89}_{-9.43}$
$3.62^{+0.06}_{-0.09}$	$84.30^{+0.92}_{-0.96}$	$0.95^{+0.04}_{-0.08}$	$0.24^{+0.09}_{-0.11}$	$0.19^{+0.19}_{-0.13}$	$-0.17^{+0.09}_{-0.14}$	$2.48^{+0.95}_{-0.90}$

Table 5.3: Other MCMC observational results from the RRM and from the RMR analysis of the HD189733 system. The derived parameters obtained from the posteriors samples are preceded by *.

Parameter	Value Reloaded	Value Revolutions	Units
$v_{eq} \sin i_*$	$3.53^{+0.27}_{-0.22}$	$3.60^{+0.07}_{-0.09}$	km s ⁻¹
ρ_*	$1.928^{+0.012}_{-0.012}$	$2.185^{+0.025}_{-0.022}$	ρ_{\odot}
P_*	$9.95^{+0.76}_{-0.49}$	$10.63^{+0.35}_{-0.32}$	d
R_*	$0.761^{+0.018}_{-0.018}$	$0.759^{+0.018}_{-0.018}$	R_{\odot}
$ld_{C1,TESS}$	$0.552^{+0.043}_{-0.046}$	$0.723^{+0.010}_{-0.010}$	
$ld_{C2,TESS}$	$0.033^{+0.067}_{-0.063}$	$0.277^{+0.010}_{-0.011}$	
$ld_{C1,HARPSN}$	$0.672^{+0.041}_{-0.045}$	$0.552^{+0.040}_{-0.040}$	
$ld_{C2,HARPSN}$	$0.862^{+0.045}_{-0.046}$	$0.760^{+0.043}_{-0.043}$	
R_p	$0.1558^{+0.0003}_{-0.0004}$	$0.1443^{+0.0002}_{-0.0003}$	R_*
b	$0.667^{+0.002}_{-0.003}$	$0.524^{+0.005}_{-0.005}$	R_*
K	$201.6^{+1.8}_{-1.7}$	$201.6^{+1.8}_{-1.7}$	m s ⁻¹
T_C	2459770.4104(52 ± 13)	2459770.4106(52 ± 10)	d
P_p	2.2185749(50 ± 26)	2.2185748(81 ± 26)	d
* a/R_*	$8.905^{+0.019}_{-0.019}$	$9.285^{+0.035}_{-0.031}$	
* i_p	$85.704^{+0.024}_{-0.023}$	$86.765^{+0.046}_{-0.041}$	deg
* M_p	$1.164^{+0.055}_{-0.054}$	$1.259^{+0.061}_{-0.060}$	M_J
* R_p	$1.154^{+0.027}_{-0.027}$	$1.066^{+0.025}_{-0.025}$	R_J

analysis. To better visualise this difference, I have used the distribution of values fitted with the two methods to obtain the two-colors corner plot of Figure 5.2. From the corner plot is easy to see that the differential rotation parameter assumes a large range of possible values in the case of the RRM method (purple), indicating that it is not well constrained, while in the case of the RMR method (green) the distribution is very close to the maximum boundary value of 1. The other parameters have in general a better defined distribution. This is particularly true

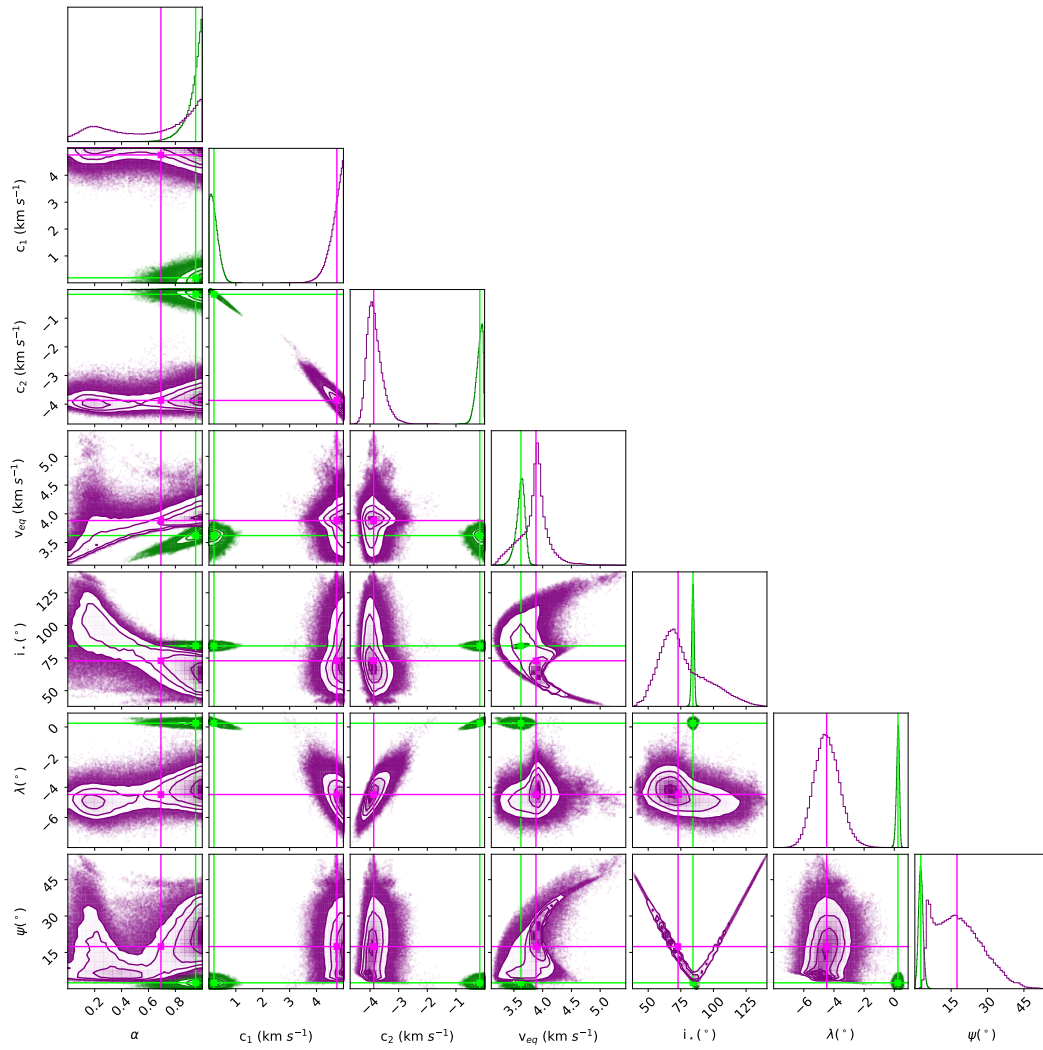


Figure 5.2: Corner plot showing with distinct colors the differences between the values obtained from the two methods. Purple indicates the Reloaded RM distributions, while green indicates those obtained from the RM Revolutions. The i_* degeneracy is still present in the RRM case. No compatibility is present between the convective coefficients fitted in the two cases and α in unconstrained.

in the case of the RMR method, for which the values are all distributed close to their median value, even if they are far from the corresponding median value of the distributions obtained with the RRM method. The degeneracy of the i_* value, of which I have already discussed in Chapter 2, is still present in the case of the RRM technique, while it seems to be lifted in the case of the RMR technique, probably because all the values are concentrated close to the median. The distribution of the values obtained for the λ angle assumes a Gaussian shape in the case of the RRM analysis, while it is more peaked in the case of the RMR analysis, but the median values associated to them assume opposite signs. Finally, since the median values of the ψ angle distributions obtained with the two methods differ by $\sim 15^\circ$, these two estimates are not compatible with each other. Still, there is a compatibility between the value of ψ obtained by modelling this dataset with the RRM technique and those that I have reported in Table 2.4 and Table 3.2, obtained fitting only the HARPS data with both methods. Lastly, I note that the impact parameter b and the scaled planetary radius R_p/R_* from the RMR analysis are inconsistent with those obtained with the standard RM analysis, the RRM analysis, and in general with the values reported in the literature using independent datasets and modelling tools. This unexpected outcome is casting several doubts on the reliability of the analysis with the RMR approach, at least when both differential rotation and the convective coefficients are involved.

Table 5.4: MCMC results of the fitted slope and intercept for the contrast (C) and for the FWHM obtained from the RMR method.

Instrument	Mask	Parameter	Value
HARPS	G2	C_m	$0.164^{+0.007}_{-0.007}$
HARPS	G2	C_q	$0.424^{+0.005}_{-0.005}$
HARPS	G2	fwhm_m	$-0.233^{+0.097}_{-0.095}$
HARPS	G2	fwhm_q	$6.995^{+0.072}_{-0.074}$
HARPS	K5	C_m	$0.073^{+0.007}_{-0.007}$
HARPS	K5	C_q	$0.381^{+0.005}_{-0.005}$
HARPS	K5	fwhm_m	$0.21^{+0.11}_{-0.11}$
HARPS	K5	fwhm_q	$5.974^{+0.08}_{-0.08}$
HARPS-N	K5	C_m	$0.107^{+0.004}_{-0.004}$
HARPS-N	K5	C_q	$0.367^{+0.003}_{-0.003}$
HARPS-N	K5	fwhm_m	$-0.326^{+0.054}_{-0.054}$
HARPS-N	K5	fwhm_q	$6.501^{+0.041}_{-0.041}$

In Table 5.4 I have reported the results obtained by fitting the slopes and the intercepts of the contrast and of the FWHM with a first order polynomial, providing also information on

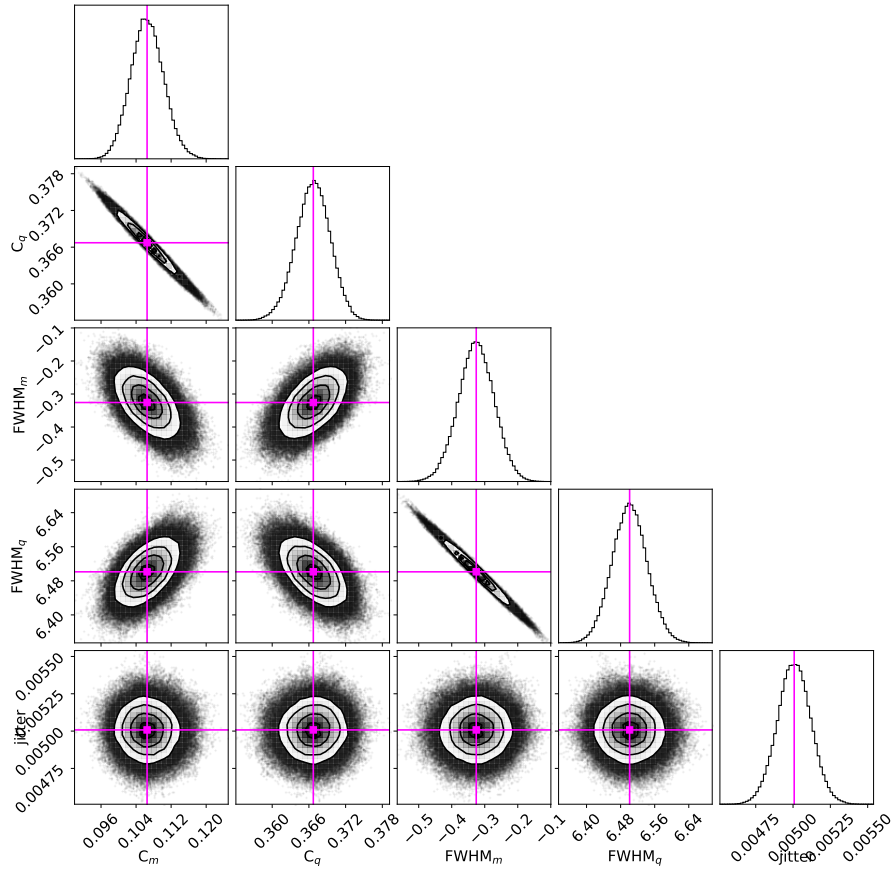


Figure 5.3: Example of corner plot obtained from the fitted slope and intercept of the parameters contrast and FWHM of the stellar spectral lines observed with HARPS-N using the K5 filtering mask.

the instrument and the filtering mask to which they correspond. To have also a visual feedback of the quantities reported in Table 5.4 I have displayed in Figure 5.3 an example of the corner plot that I have obtained. The diagonal histograms of the plot show that all the parameters have been correctly fitted by the model, since the values obtained are distributed according to a Gaussian shape. There are no unexpected features in the panels and is clear the correlation of the slope and intercept of each parameter, as is expected in the case of a linear trend. This corner plot is also confirming that almost no information is contained in the depth and in the width of the stellar spectral lines, represented by the contrast and the FWHM parameters. Therefore almost all the information is extracted from the radial velocity, which is the centroid of the stellar spectral line.

5.3 RELOADED AND REVOLUTIONS SECOND ANALYSIS

Here I present the results that I have obtained from the second analysis that I have performed with both the RRM and the RMR methods excluding from the fit the parameter related to the differential rotation, α , and the two coefficients related to the convective velocity, c_1 and c_2 . I have decided to exclude these effects as their modelling produces inconsistent results with either different datasets or different techniques, and I suspect that my dataset is not able to properly constrain the associated parameters. In Table 5.5 and in Table 5.6 I have reported all the results of the fitted parameters. I note how the fact of having excluded both the effects of the stellar

Table 5.5: MCMC observational results for HD189733 and the derived 3D spin-orbit obliquity. First row is for the Reloaded RM and second row is for the RM Revolutions. Parameters that have not been included in the fit are indicated with /.

$v_{eq} \sin i_*$ (km s ⁻¹)	i_* (°)	α	λ (°)	c_1	c_2	ψ (°)
$3.141^{+0.034}_{-0.032}$	$103.23^{+18.82}_{-38.75}$	/	$-0.37^{+0.32}_{-0.32}$	/	/	$24.64^{+12.47}_{-12.00}$
$3.088^{+0.011}_{-0.012}$	$97.58^{+22.27}_{-35.13}$	/	$-0.13^{+0.11}_{-0.12}$	/	/	$23.76^{+11.85}_{-11.57}$

differential rotation and of the convective blueshift from the modelling has produced results that, differently from the first analysis are more similar with each other. First of all, the impact parameters and the scaled planetary radius from the RMR analysis are now consistent with all the other analysis. Secondly, there is a consistency in the estimated values of the ψ angle, which results $\sim (24 \pm 12)^\circ$ in both cases, while in the previous analysis there was a difference of $\sim 15^\circ$ between the median values obtained applying the RRM and the RMR method.

However the values of ψ that I got as result of this second analysis are substantially larger than those obtained in the previous analysis and are much similar to that obtained in the RMR analysis of the HARPS data including both α and v_{conv} , that I have reported in the Table 3.2. To better visualise the results, I have also produced the corner plot displayed in Figure 5.4. I have used different colors to distinguish the results obtained with the two methods. The first thing that I note is the double Gaussian distribution in the histogram of the i_* parameter. This outcome is not surprising, as it is related to the fact that I am not able to distinguish if the planet is transiting above or below the stellar equator, as already observed in Chapter 2. In this analysis the stellar spin angle is not derived from the the stellar differential rotation α and equatorial velocity v_{eq} as in the previous analysis, but is obtained combining the distributions

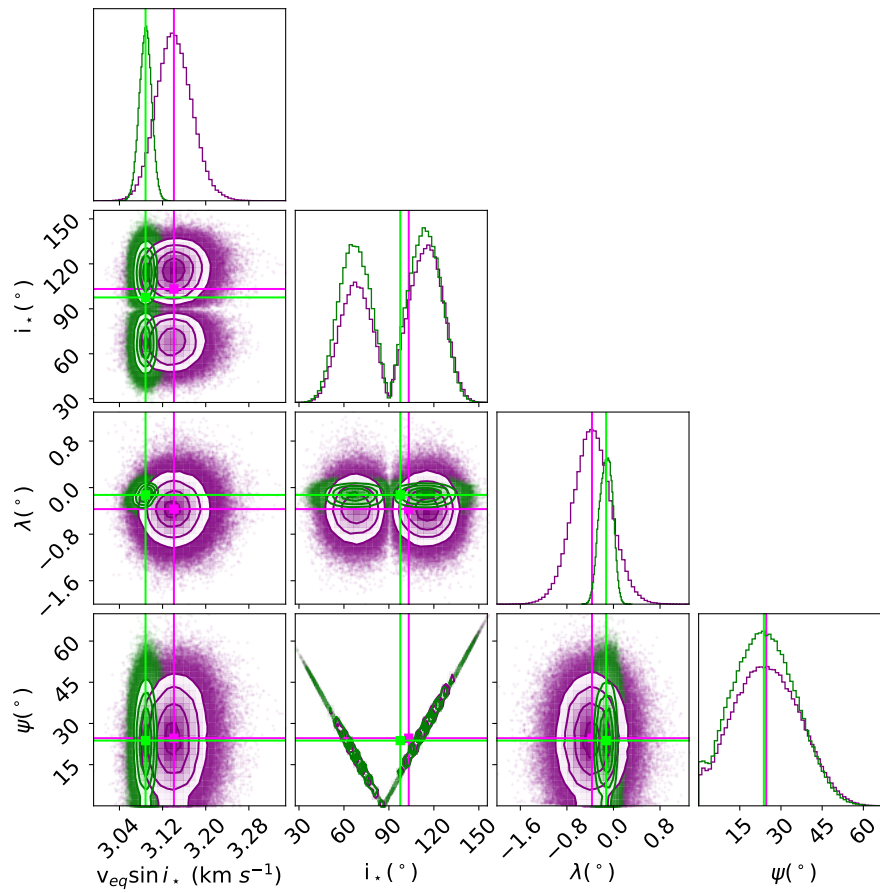


Figure 5.4: Corner plot showing with distinct colors the differences between the values obtained from the two methods. Purple indicates the Reloaded RM distributions, while green indicates those obtained from the RM Revolutions.

of values of the stellar rotation period P_* and radius R_* with that of the $v_{eq} \sin i_*$ as

$$i_* = \arcsin \left(v \sin i_* \cdot \frac{P_*}{2\pi R_*} \right). \quad (5.1)$$

To perform this computation I have used the goniometric functions of the numpy package. When I checked the results I found that the arcsin function implemented in numpy had excluded from the computation all the values for which the argument $\theta = (v \sin i_* \cdot \frac{P_*}{2\pi R_*})$ was larger than 1. This makes sense from the mathematical point of view, but represents a problem, because part of the values which instead have a physical meaning are discarded. To overcome this problem, I wrote a Python script where I have selected all the values of θ larger than 1 and I have subtracted the constant value of 2 from them. With this arrangement, all the values of θ have been moved inside the interval of $[-1, 1]$, where the arcsin function is defined. The operation that I have performed has allowed me to retrieve also the otherwise discarded values of i_* , which are responsible for the second Gaussian distribution which median is larger than 90° . Therefore here I have proved again the presence of the aforementioned i_* degeneracy, of which the authors of the papers have not provided any description.

Table 5.6: Other MCMC observational results from the RRM and from the RMR analysis of the HD189733 system. The derived parameters obtained from the posteriors samples are preceded by *.

Parameter	Value Reloaded	Value Revolutions	Units
ρ_*	$1.928^{+0.012}_{-0.013}$	$1.925^{+0.013}_{-0.013}$	ρ_\odot
$ld_{C1,TESS}$	$0.462^{+0.038}_{-0.039}$	$0.469^{+0.089}_{-0.110}$	
$ld_{C2,TESS}$	$0.116^{+0.054}_{-0.053}$	$0.09^{+0.20}_{-0.13}$	
$ld_{C1,HARPSN}$	$0.603^{+0.041}_{-0.042}$	$0.494^{+0.037}_{-0.038}$	
$ld_{C2,HARPSN}$	$0.805^{+0.046}_{-0.045}$	$0.686^{+0.042}_{-0.042}$	
R_p	$0.1549^{+0.0003}_{-0.0003}$	$0.1552^{+0.0001}_{-0.0001}$	R_*
b	$0.662^{+0.002}_{-0.003}$	$0.663^{+0.005}_{-0.008}$	R_*
K	$201.5^{+1.7}_{-1.8}$	$201.6^{+1.7}_{-1.8}$	m s^{-1}
T_C	$2459770.4104(55 \pm 13)$	$2459770.4104(48 \pm 13)$	d
P_p	$2.2185750(09 \pm 21)$	$2.2185748(95 \pm 36)$	d
* a/R_*	$8.906^{+0.019}_{-0.019}$	$8.901^{+0.020}_{-0.020}$	
* i_p	$85.737^{+0.023}_{-0.023}$	$85.730^{+0.020}_{-0.020}$	deg
* M_p	$1.124^{+0.045}_{-0.046}$	$1.124^{+0.046}_{-0.046}$	M_J
* R_p	$1.140^{+0.027}_{-0.027}$	$1.140^{+0.028}_{-0.028}$	R_J

In Figure 5.5 I have also plotted the estimated value of i_* obtained from the first analysis

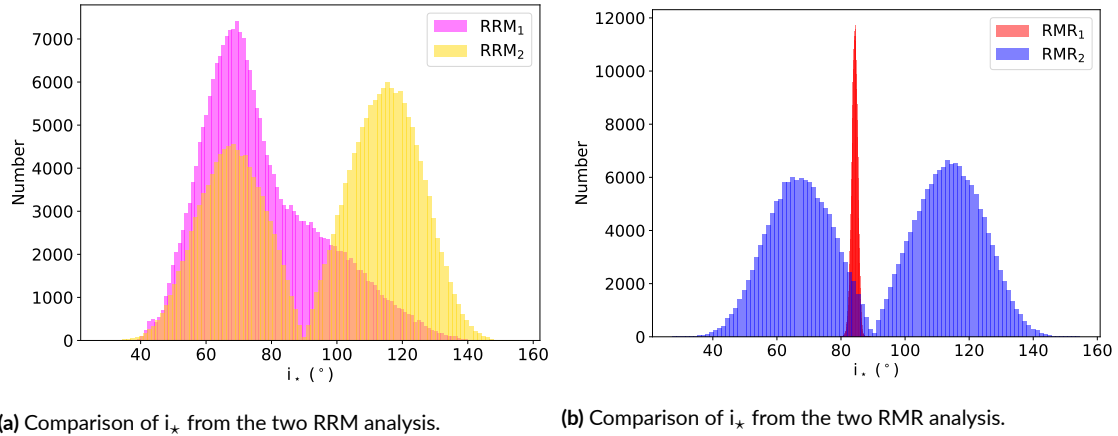


Figure 5.5: These plots show the comparison between the estimated values of i_* obtained from the two analysis. In Figure 5.5a are displayed the distributions of values obtained with the RRM method, while in Figure 5.5b those obtained with the RMR method.

against that obtained from the second analysis for both the RRM and the RMR methods. I note that in both cases there is a clear difference between the distributions obtained in the first and in the second analysis, with the second analysis characterised by a double Gaussian profile with median value symmetric with respect to 90° and with a slightly larger probability for the distribution on the right. The fact that values larger than 90° have a larger probability finds a confirm in the results of the analysis performed in Chapter 2 and in Chapter 3 using only HARPS data. This is interesting, because I would have not find a single i_* value larger than 90° without the operation on $\theta > 1$, and I can thus say that my intuition on the problem related to the domain of definition of the arcsin function indeed was correct.

In Table 5.6 I have included other results that I have obtained from the MCMC analysis with both methods. In particular in this table I have also reported the derived parameters obtained from the posterior samples. Among these values I note the planetary radius *R_p , which estimate is slightly larger in the case of the RRM method than in the RMR method, although compatible within the errors. Lastly, in Table 5.7 I have reported the results of the fitted slope and intercept for both the contrast and the FWHM obtained from this second RMR analysis. In order to have also a visual feedback of these quantities, in Figure 5.6 I have displayed an example of the corner plot that I have obtained starting from their values. The diagonal histograms of the plot show that all the parameters have been correctly fitted by the model, since the values obtained are distributed according to a Gaussian shape. From the other panels is possible to recognise the correlation between the slope and intercept of the fitted contrast and FWHM,

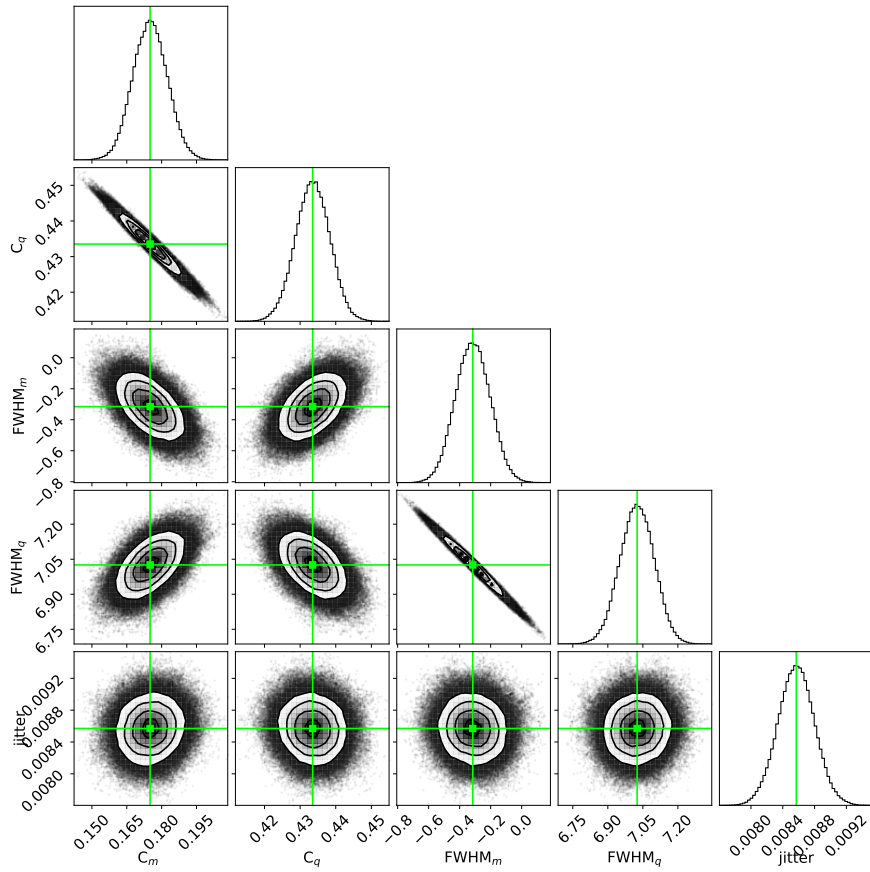


Figure 5.6: Example of corner plot obtained from the fitted slope and intercept of the parameters contrast and FWHM of the stellar spectral lines observed with HARPS using the G2 filtering mask.

Table 5.7: MCMC results of the fitted slope and intercept for the contrast (C) and for the FWHM obtained from the RMR method.

Instrument	Mask	Parameter	Value
HARPS	G2	C_m	$0.175^{+0.008}_{-0.007}$
HARPS	G2	C_q	$0.434^{+0.005}_{-0.005}$
HARPS	G2	fwhm_m	$-0.320^{+0.110}_{-0.110}$
HARPS	G2	fwhm_q	$7.026^{+0.073}_{-0.074}$
HARPS	K5	C_m	$0.082^{+0.007}_{-0.007}$
HARPS	K5	C_q	$0.383^{+0.005}_{-0.005}$
HARPS	K5	fwhm_m	$0.15^{+0.12}_{-0.12}$
HARPS	K5	fwhm_q	$6.03^{+0.08}_{-0.08}$
HARPS-N	K5	C_m	$0.117^{+0.004}_{-0.004}$
HARPS-N	K5	C_q	$0.371^{+0.003}_{-0.003}$
HARPS-N	K5	fwhm_m	$-0.346^{+0.060}_{-0.060}$
HARPS-N	K5	fwhm_q	$6.481^{+0.039}_{-0.039}$

confirming the aforementioned linear trend. No other relevant features are present neither in this case. This allows me to say that indeed most of the information of the system comes from the centroids of the stellar lines, which are related to the radial velocity, while the contrast and FWHM are not adding much information.

5.4 COMPARISON OF THE RESULTS

In Table 5.8 I have reported again the results that I have presented in the previous sections. Each

Table 5.8: MCMC observational results of all the analysis. Each row corresponds to a different analysis; **first:** standard RM method, **second:** 1st analysis with RRM method, **third:** 1st analysis with RMR method, **fourth:** 2nd analysis with RRM method, and **fifth:** 2nd analysis with RMR method.

$v_{eq} \sin i_*$	i_*	α	λ	c_1	c_2	ψ
$2.55^{+0.02}_{-0.02}$	/	/	$0.02^{+0.22}_{-0.22}$	/	/	/
$3.53^{+0.27}_{-0.22}$	$72.88^{+24.06}_{-12.88}$	$0.69^{+0.25}_{-0.49}$	$-4.48^{+0.86}_{-0.81}$	$4.76^{+0.18}_{-0.31}$	$-3.87^{+0.31}_{-0.21}$	$17.41^{+10.89}_{-9.43}$
$3.60^{+0.07}_{-0.09}$	$84.30^{+0.92}_{-0.96}$	$0.95^{+0.04}_{-0.08}$	$0.24^{+0.09}_{-0.11}$	$0.19^{+0.19}_{-0.13}$	$-0.17^{+0.09}_{-0.14}$	$2.48^{+0.95}_{-0.90}$
$3.14^{+0.03}_{-0.03}$	$103.23^{+18.82}_{-38.75}$	/	$-0.37^{+0.32}_{-0.32}$	/	/	$24.64^{+12.47}_{-12.00}$
$3.09^{+0.01}_{-0.01}$	$97.58^{+22.27}_{-35.13}$	/	$-0.13^{+0.11}_{-0.12}$	/	/	$23.76^{+11.85}_{-11.57}$
(km s ⁻¹)	(°)		(°)	(km s ⁻¹)	(km s ⁻¹)	(°)

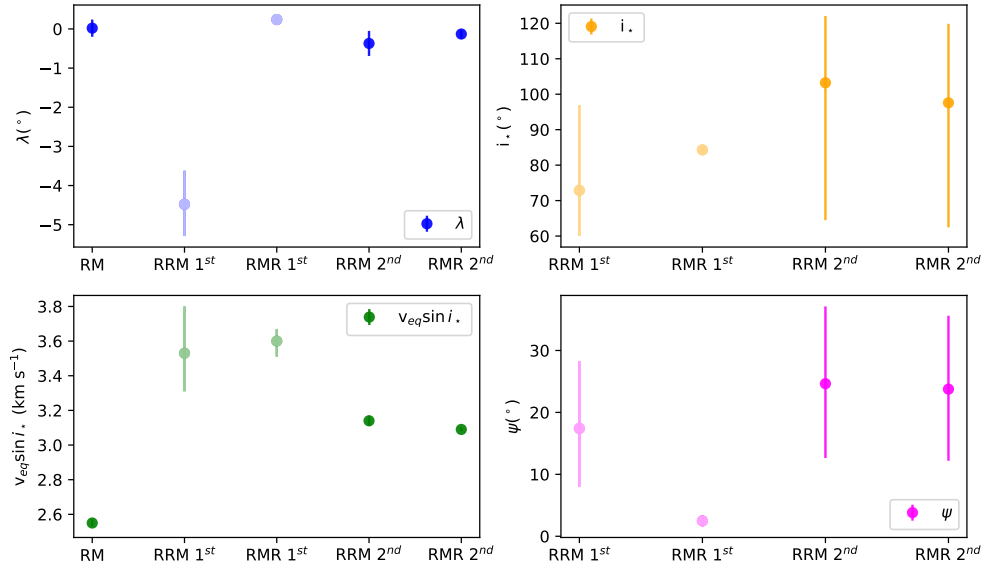


Figure 5.7: Comparison of the estimates reported in Table 5.8. Different colors are used for different parameters. The labels of the x-axis are referring to the methods (standard RM, RRM and RMR) and to the analysis (1st and 2nd). Faint colors are used to indicate the unreliable values obtained in the first analysis with both the RRM and the RMR method.

row of the table corresponds to a different analysis. From a first look, it is clear that the results that I have obtained substantially change from one method to the other. To better display this differences, I decided to plot the estimated values all together in Figure 5.7. In particular, in the plot I have included the 5 estimates of λ and $v_{eq} \sin i_*$ and the 4 estimates of i_* and ψ .

The two plots on the right are confirming that the first analysis performed with the RMR method is not reliable, as the error bars of both i_* and ψ are unrealistically small compared with the other analysis, including the RMR itself under different assumptions and is clear that the value of ψ obtained with this analysis is not compatible with the other three, which instead are compatible with each other. The estimated i_* are instead compatible, but this is mostly because of the very large error-bars associated to the measures. The upper left plot is showing that the value of λ obtained from the first analysis with the RRM method is an outlier, and is not compatible with the others, which are also characterised by smaller error-bars. Finally, the lower right plot, shows that in the case in which $v_{eq} \sin i_*$ is a fitted quantity of the MCMC analysis, than the estimates are more accurate (RM and second analysis with both RRM and RMR) and in general have a smaller median value, while they have a broader distribution and a larger median value in the case in which they are derived parameters (first analysis with RRM and RMR).

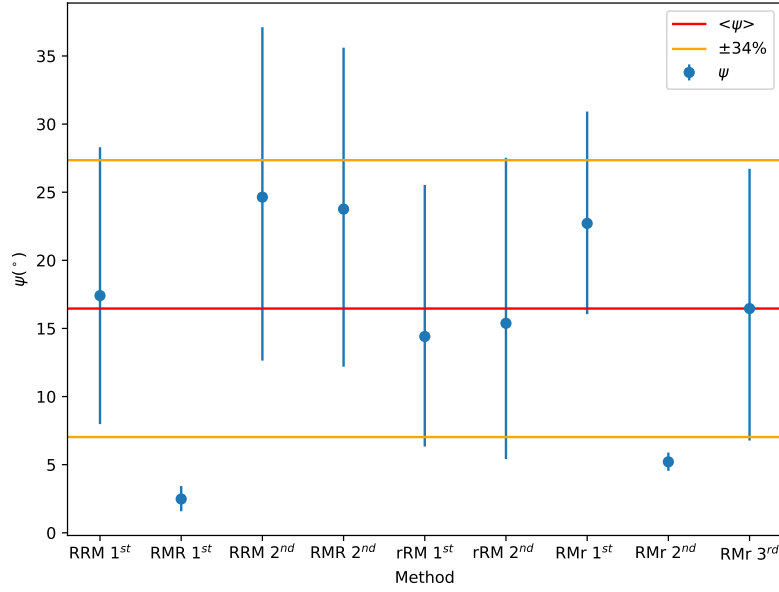


Figure 5.8: Comparison of all the 9 estimated values of the true 3D spin-orbit angle ψ . Each point in the plot corresponds to the result of a different analysis. In the x-axis are reported the acronyms of the analysis. In particular, rRM and RMR represent respectively the results of the Reloaded RM and of the RM Revolutions analysis applied only to the HARPS data, reported in Table 2.4 and Table 3.2. Red and orange horizontal lines are indicating the median and the 16 and 84 percentile.

Since the power of the two techniques that I have implemented is that of measuring the true 3D spin-orbit angle ψ , I have decided to compare all the estimates of this angle that I have obtained in my work, by plotting their values all together in Figure 5.8. This plot shows that except for the two isolated cases of the first analysis performed on the entire dataset using the RMR method (RMR 1st), and the second analysis performed only on the HARPS data using the RMR method (RMR 2nd), the estimates are compatible with each other. Computing the median of the 9 ψ values that I have found, my best estimate for the 3D spin-orbit angle is $16.46^{+10.89}_{-9.47}$ °. The result reported in Cegla et al. 2016[3] was $\psi = \sim 7^{+12}_{-4}$ °, so less than half of mine in terms of median value, but thanks to the very large error associated to them, the two estimates are still compatible. Moreover, in Winn et al. 2007[12] the authors explain that they have determined an upper bound on the ψ angle of 27° with 95% confidence. So my estimate falls in between the result obtained by Cegla et al. 2016 and the upper bound found by Winn et al. 2007.

In Table 5.9 I have merged all the other results already presented in this chapter, reporting the information on the method and on the analysis to which they are referred. From this table is possible to see that the results obtained with the RMR method during the first analysis

represent an outlier case. In particular, the estimate of the impact parameter b obtained in this case is much smaller than those obtained in the other analysis. A smaller value is also obtained for the ratio of planet radius to stellar radius R_p/R_* and for the radius of the planet. The opposite trend is followed by the stellar density ρ_* , by the orbital inclination i_p , by the mass of the planet and by the ratio of semi-major axis to planet radius a/R_* . The results obtained in the other analysis are instead compatible with each other. The fact that analysis performed with different methods and imposing different conditions produce results that are compatible with each other, allows me to say that in the isolate case of the 1st RMR analysis something went wrong during the modelling, probably due to some systematic error which is currently under investigation.

Table 5.9: Comparison of the results obtained with the different methods. Derived parameters obtained from the posterior samples are preceded by *.

Parameter	Standard RM	1 st RRM	1 st RMR	2 nd RRM	2 nd RMR
ρ_* (ρ_\odot)	$1.930^{+0.012}_{-0.013}$	$1.928^{+0.012}_{-0.012}$	$2.185^{+0.025}_{-0.022}$	$1.928^{+0.012}_{-0.013}$	$1.925^{+0.013}_{-0.013}$
$ld_{C1,TESS}$	$0.480^{+0.045}_{-0.047}$	$0.552^{+0.043}_{-0.046}$	$0.723^{+0.010}_{-0.010}$	$0.462^{+0.038}_{-0.039}$	$0.469^{+0.089}_{-0.110}$
$ld_{C2,TESS}$	$0.086^{+0.071}_{-0.066}$	$0.033^{+0.067}_{-0.063}$	$0.277^{+0.010}_{-0.011}$	$0.116^{+0.054}_{-0.053}$	$0.09^{+0.20}_{-0.13}$
$ld_{C1,HARPSN}$	$0.260^{+0.034}_{-0.034}$	$0.672^{+0.041}_{-0.045}$	$0.552^{+0.040}_{-0.040}$	$0.603^{+0.041}_{-0.042}$	$0.494^{+0.037}_{-0.038}$
$ld_{C2,HARPSN}$	$0.527^{+0.041}_{-0.040}$	$0.862^{+0.045}_{-0.046}$	$0.760^{+0.043}_{-0.043}$	$0.805^{+0.046}_{-0.045}$	$0.686^{+0.042}_{-0.042}$
R_p/R_*	$0.1551^{+0.0003}_{-0.0004}$	$0.1558^{+0.0003}_{-0.0004}$	$0.1443^{+0.0002}_{-0.0003}$	$0.1549^{+0.0003}_{-0.0003}$	$0.1552^{+0.0001}_{-0.0001}$
$b (R_*)$	$0.663^{+0.002}_{-0.003}$	$0.667^{+0.002}_{-0.003}$	$0.524^{+0.005}_{-0.005}$	$0.662^{+0.002}_{-0.003}$	$0.663^{+0.005}_{-0.008}$
$K (m s^{-1})$	$199.99^{+0.82}_{-0.79}$	$201.6^{+1.8}_{-1.7}$	$201.6^{+1.8}_{-1.7}$	$201.5^{+1.7}_{-1.8}$	$201.6^{+1.7}_{-1.8}$
* a/R_*	$8.909^{+0.019}_{-0.020}$	$8.905^{+0.019}_{-0.019}$	$9.285^{+0.035}_{-0.031}$	$8.906^{+0.019}_{-0.019}$	$8.901^{+0.020}_{-0.020}$
* $i_p (^\circ)$	$85.732^{+0.024}_{-0.020}$	$85.704^{+0.024}_{-0.023}$	$86.765^{+0.046}_{-0.041}$	$85.737^{+0.023}_{-0.023}$	$85.730^{+0.020}_{-0.020}$
* $M_p (M_J)$	$1.116^{+0.044}_{-0.045}$	$1.164^{+0.055}_{-0.054}$	$1.259^{+0.061}_{-0.060}$	$1.124^{+0.045}_{-0.046}$	$1.124^{+0.046}_{-0.046}$
* $R_p (R_J)$	$1.141^{+0.027}_{-0.027}$	$1.154^{+0.027}_{-0.027}$	$1.066^{+0.025}_{-0.025}$	$1.140^{+0.027}_{-0.027}$	$1.140^{+0.028}_{-0.028}$

6

Conclusion

In this Master Thesis I have presented a new implementation of the revolutionary method proposed by Cegla et al. 2016[3] and by Bourrier et al. 2021[2] which allows the measurement of the true 3D spin-orbit angle ψ with unprecedented accuracy. I have then focused my attention to HD189733b, a Jupiter-like exoplanet with a period of 2.2 days orbiting a K2 star. This exoplanet is a golden target for exoplanetary atmosphere studies, due to the brightness of its host star (magnitude $V=7.6$) and the extreme conditions undergoing on its outer layer. The analysis of the atmosphere relies on accurate characterization of the planetary and orbital characteristics, hence the importance of measuring the geometry of the planetary system.

Since the authors of the paper have not released their code, in order to reproduce the model presented by Cegla et al 2016, called Reloaded Rossiter-McLaughlin (RRM) technique, I had to rebuild the mathematical framework and the various steps required for the data handling and the data analysis, using the same HARPS data on HD189733 they used in their analysis aiming to get the same results. I have been able to reproduce the model and I have discovered the presence of a degeneracy in the i_* angle, of which the authors of the paper did not provide any information in their paper. Since in my analysis I have fitted the same parameters, with the same priors and boundaries described in the paper, I wanted to go deeper in understanding the reason why I found a degeneracy in the i_* angle values. Given that the RM effect is symmetric with respect to the stellar equatorial plane, by keeping all the parameters of the system fixed and changing only the stellar inclination angle, I have been able to obtain the same identical value of ψ starting from two completely different values of i_* . I can not exclude the presence of any

systematic error in my implementation of the code, but the presence of this degeneracy could be the reason why my estimate of the ψ angle ($\sim 15_{-10}^{+12}$ °) results larger than the one reported in the paper ($\sim 7_{-4}^{+12}$ °), even if they still are compatible thanks to the large value of the error associated to them. Moreover, my estimate is well below the upper bound on the ψ angle, which is of 27° with 95% confidence, as reported in Winn et al. 2007[12].

Subsequently, I have implemented the recent improvement proposed by Bourrier et al. 2021, dubbed Rossiter-McLaughlin effect Revolutions (RMR), which further expands the RRM by simultaneously modelling all the in-transit cross correlation functions through a Bayesian approach, enabling the measurement of the ψ angle of small exoplanets even when the classical RM signal is undetectable. Also in this case I had to write a new code to reproduce this technique, since the authors did not release their code. To do that, I have taken advantage of the code that I wrote for the RRM technique and I have used the same HARPS data of the previous analysis. In the modelling I have included both the contribution of the stellar differential rotation and of the convective blueshift, obtaining different results, despite the fact of having used the same data and model of the RRM analysis. I tried to exclude the convective contribution or the stellar differential rotation, obtaining other unexpected results and suggesting that both effects cannot be constrained properly with this technique. In the RMR modelling I have also fitted the contrast and the FWHM of the stellar spectral lines with a first order polynomial. The fit has properly worked, producing well defined Gaussian shaped distributions of values for the slope and the intercept of these two parameters. From this fact I discovered that indeed most of the information of the system that I have obtained is extracted from the radial velocity measurements, which are the expression of the centroids of the stellar lines.

After validating the mathematical framework and the data analysis steps of my implementation of the RRM and the RMR techniques, I have used the free access PyORBIT code to perform a combined modelling of photometric data spanning over fifteen years, high precision radial velocity data from the literature, and eight in-transit spectroscopic time series, in a robust and reliable Bayesian framework. In my dataset I have included also light curves coming from two sectors of TESS (41 and 54), and I have used these data to determine the radius of the planet, $R_p = (1.141 \pm 0.027) R_J$, which indeed is the most precise radius measurement of this planet so far. With the high precision radial velocity data that I have gathered from the literature I have been able to determine also a new estimate of the mass of the planet $M_p = 1.116_{-0.045}^{+0.044} M_J$. Together with the HARPS data that I had already analysed, I have included in the dataset also unpublished spectroscopic time series over four nights of observations obtained in the context of the GAPS program using the ultra-stable HARPS-N spectrograph at the TNG. I have

performed many different analysis, imposing different conditions and using three models for the RM effect, adding to the RRM and RMR methods also the standard model already implemented in PyORBIT. Contrarily to what I expected, the results obtained applying the RRM and RMR techniques to this new dataset are inconsistent with those obtained when using only the HARPS data. In particular, including in the dataset also the HARPS-N data, which are virtually identical (or even better) data, I have obtained diverging values for the convective coefficients and a large value (close to the maximum boundary of 1) for the stellar differential rotation. This fact cast a shadow on the robustness of the already published results and, considering that the results change in a consistent way depending on the dataset that I used, I can conclude that neither the RRM nor the RMR technique allowed me to obtain reliable information on the stellar differential rotation and on the centre-to-limb convective blueshift variations, differently from what is reported in the papers of Cegla et al. 2016[3] and Bourrier et al. 2021[2]. I can not exclude any possible error in my implementation of the methods, even if I have verified that my model applied to the dataset presented in Chapter 4 has reproduced the effect of the differential rotation and of the convective blueshift described in Cegla et al. 2016[6] and Hathaway et al. 2015[4]. Moreover, when using only the HARPS data, I have been able to reproduce the results presented in Cegla et al. 2016[3], with the necessary caveats, and there is not a reason to think that the problem is related to the HARPS-N data, given the similarity between the two instruments and since the CCF treatment has been identical. In order to include the differential rotation in the dataset gathered from the papers, the shear parameter has to be measured in a independent way, for example using spectropolarimetry, as is described in Fares et al. 2010[16], while to treat the centre-to-limb convective blueshift, a possible solution could be that of using synthetic spectra computed as a function of the limb angle, similarly to what is shown in Czesla et al. 2015[17]. I note that Bourrier et al. 2022[18] and Bourrier et al. 2023[19] did not include these two effects in their analysis of 15 exoplanets using the RMR technique, probably because they have encountered the same problem that I found when trying to fit α and v_{conv} .

As an alternative solution to the problematic treatment of differential rotation and convective blue-shift, I resorted to the projected rotational velocity of the star, measured from my data, and the knowledge of the rotational period of the star, which can be easily obtained from ground and space based photometry, to characterize the 3D spin-orbit geometry of the star-planet system. Although the advanced techniques for the analysis of the Rossiter-McLaughlin effect discussed in this Master Thesis still need additional development regarding some detailed effects involved in the modelling, new perspective are opening for many exoplanets with in-

transit spectroscopic observations. As the system architecture and orbital properties of exoplanets are shaped during the first hundreds of millions of years of their life, assessing the true spin-orbit angle of young star-planet systems would be of extreme importance to strongly constrain the dynamical evolution of planets and discriminate between different formation scenarios. For this reason I intend to further extend the RRM and RMR techniques to determine the obliquity of young stars, which are characterised by short rotation period (on the order of a few days) and consequently strong magnetic activity, resulting in the prominent presence of active regions, which are characterised by different temperatures and are responsible for the brightness variation and the spectral line deformation. With the RRM and RMR techniques I have the possibility to explore the stellar surface properties while being occulted by the planet, so I intend to use the consistent effort to characterise stellar activity across several stellar rotation periods to build a framework which allows me to model the effect of stellar activity during a transit, hence enabling the determination of ψ also for young objects. The outcome of this project is expected to advance not only the field of planetary formation and evolution, but also to improve the atmospheric characterization of exoplanets in the presence of stellar activity.

References

- [1] A. H. M. J. Triaud, *The Rossiter–McLaughlin Effect in Exoplanet Research*. Cham: Springer International Publishing, 2018, pp. 1375–1401. [Online]. Available: https://doi.org/10.1007/978-3-319-55333-7_2
- [2] V. Bourrier, C. Lovis, M. Cretignier, R. Allart, X. Dumusque, J. B. Delisle, A. Deline, S. G. Sousa, V. Adibekyan, Y. Alibert, S. C. C. Barros, F. Borsa, S. Cristiani, O. Demangeon, D. Ehrenreich, P. Figueira, J. I. González Hernández, M. Lendl, J. Lillo-Box, G. Lo Curto, P. Di Marcantonio, C. J. A. P. Martins, D. Mégevand, A. Mehner, G. Micela, P. Molaro, M. Oshagh, E. Palle, F. Pepe, E. Poretti, R. Rebolo, N. C. Santos, G. Scandariato, J. V. Seidel, A. Sozzetti, A. Suárez Mascareño, and M. R. Zapatero Osorio, “The Rossiter-McLaughlin effect revolutions: an ultra-short period planet and a warm mini-Neptune on perpendicular orbits,” *Astronomy and Astrophysics*, vol. 654, p. A152, Oct. 2021. [Online]. Available: <https://doi.org/10.1051/0004-6361/202141527>
- [3] H. M. Cegla, C. Lovis, V. Bourrier, B. Beeck, C. A. Watson, and F. Pepe, “The Rossiter-McLaughlin effect reloaded: Probing the 3D spin-orbit geometry, differential stellar rotation, and the spatially-resolved stellar spectrum of star-planet systems,” *Astronomy and Astrophysics*, vol. 588, p. A127, Apr. 2016. [Online]. Available: <https://doi.org/10.1051/0004-6361/201527794>
- [4] D. H. Hathaway, T. Teil, A. A. Norton, and I. Kitiashvili, “The sun’s photospheric convection spectrum,” *The Astrophysical Journal*, vol. 811, no. 2, p. 105, sep 2015. [Online]. Available: <https://dx.doi.org/10.1088/0004-637X/811/2/105>
- [5] D. Foreman-Mackey, D. W. Hogg, D. Lang, and J. Goodman, “emcee: The mcmc hammer,” *Publications of the Astronomical Society of the Pacific*, vol. 125, no. 925, p. 306, feb 2013. [Online]. Available: <https://dx.doi.org/10.1086/670067>
- [6] H. M. Cegla, M. Oshagh, C. A. Watson, P. Figueira, N. C. Santos, and S. Shelyag, “Modelling the rossiter–mclaughlin effect: impact of the convective centre-to-limb

- variations in the stellar photosphere,” *The Astrophysical Journal*, vol. 819, no. 1, p. 67, feb 2016. [Online]. Available: <https://dx.doi.org/10.3847/0004-637X/819/1/67>
- [7] M. Hippke, T. J. David, G. D. Mulders, and R. Heller, “Wotan: Comprehensive time-series detrending in python,” *The Astronomical Journal*, vol. 158, no. 4, p. 143, sep 2019. [Online]. Available: <https://dx.doi.org/10.3847/1538-3881/ab3984>
- [8] Bouchy, F., Udry, S., Mayor, M., Moutou, C., Pont, F., Iribarne, N., Da Silva, R., Ilovaisky, S., Queloz, D., Santos, N. C., Ségransan, D., and Zucker, S., “Elodie metallicity-biased search for transiting hot jupiters - ii. a very hot jupiter transiting the bright k star hd189733,” *Astronomy and Astrophysics*, vol. 444, no. 1, pp. L15–L19, dec 2005. [Online]. Available: <https://doi.org/10.1051/0004-6361:200500201>
- [9] J. N. Winn, J. A. Johnson, G. W. Marcy, R. P. Butler, S. S. Vogt, G. W. Henry, A. Roussanova, M. J. Holman, K. Enya, N. Narita, Y. Suto, and E. L. Turner, “Measurement of the spin-orbit alignment in the exoplanetary system hd189733,” *The Astrophysical Journal*, vol. 653, no. 1, p. L69, nov 2006. [Online]. Available: <https://dx.doi.org/10.1086/510528>
- [10] Boisse, I., Moutou, C., Vidal-Madjar, A., Bouchy, F., Pont, F., Hébrard, G., Bonfils, X., Croll, B., Delfosse, X., Desort, M., Forveille, T., Lagrange, A.-M., Loeillet, B., Lovis, C., Matthews, J. M., Mayor, M., Pepe, F., Perrier, C., Queloz, D., Rowe, J. F., Santos, N. C., Ségransan, D., and Udry, S., “Stellar activity of planetary host star hd189733,” *Astronomy and Astrophysics*, vol. 495, no. 3, pp. 959–966, mar 2009. [Online]. Available: <https://doi.org/10.1051/0004-6361:200810648>
- [11] G. A. Bakos, H. Knutson, F. Pont, C. Moutou, D. Charbonneau, A. Shporer, F. Bouchy, M. Everett, C. Hergenrother, D. W. Latham, M. Mayor, T. Mazeh, R. W. Noyes, D. Queloz, A. Pál, and S. Udry, “Refined parameters of the planet orbiting hd 189733,” *The Astrophysical Journal*, vol. 650, no. 2, pp. 1160–1171, oct 2006. [Online]. Available: <https://dx.doi.org/10.1086/506316>
- [12] J. N. Winn, M. J. Holman, G. W. Henry, A. Roussanova, K. Enya, Y. Yoshii, A. Shporer, T. Mazeh, J. A. Johnson, N. Narita, and Y. Suto, “The transit light curve project. v. system parameters and stellar rotation period of hd 189733,” *The Astronomical Journal*, vol. 133, no. 4, p. 1828, mar 2007. [Online]. Available: <https://dx.doi.org/10.1086/512159>

- [13] T.-O. Husser, S. Wende-von Berg, S. Dreizler, D. Homeier, A. Reiners, T. Barman, and P. H. Hauschildt, “Astrophysics A new extensive library of PHOENIX stellar atmospheres,” *Astronomy and Astrophysics*, vol. 553, p. A6, 2013.
- [14] Malavolta, L., Nascimbeni, V., Piotto, G., Quinn, S. N., Borsato, L., Granata, V., Bonomo, A. S., Marzari, F., Bedin, L. R., Rainer, M., Desidera, S., Lanza, A. F., Poretti, E., Sozzetti, A., White, R. J., Latham, D. W., Cunial, A., Libralato, M., Nardiello, D., Boccato, C., Claudi, R. U., Cosentino, R., Covino, E., Gratton, R., Maggio, A., Micela, G., Molinari, E., Pagano, I., Smareglia, R., Affer, L., Andreuzzi, G., Aparicio, A., Benatti, S., Bignamini, A., Borsa, F., Damasso, M., Di Fabrizio, L., Harutyunyan, A., Esposito, M., Fiorenzano, A. F. M., Gandolfi, D., Giacobbe, P., González Hernández, J. I., Maldonado, J., Masiero, S., Molinaro, M., Pedani, M., and Scandariato, G., “The gaps programme with harps-n at tng - xi. pr1 in m the first multi-planet system in an open cluster,” *Astronomy and Astrophysics*, vol. 588, p. A118, apr 2016. [Online]. Available: <https://doi.org/10.1051/0004-6361/201527933>
- [15] Covino, E., Esposito, M., Barbieri, M., Mancini, L., Nascimbeni, V., Claudi, R., Desidera, S., Gratton, R., Lanza, A. F., Sozzetti, A., Biazzo, K., Affer, L., Gandolfi, D., Munari, U., Pagano, I., Bonomo, A. S., Collier Cameron, A., Hébrard, G., Maggio, A., Messina, S., Micela, G., Molinari, E., Pepe, F., Piotto, G., Ribas, I., Santos, N. C., Southworth, J., Shkolnik, E., Triaud, A. H. M. J., Bedin, L., Benatti, S., Boccato, C., Bonavita, M., Borsa, F., Borsato, L., Brown, D., Carolo, E., Ciceri, S., Cosentino, R., Damasso, M., Faedi, F., Martínez Fiorenzano, A. F., Latham, D. W., Lovis, C., Mordasini, C., Nikolov, N., Poretti, E., Rainer, M., Rebolo López, R., Scandariato, G., Silvotti, R., Smareglia, R., Alcalá, J. M., Cunial, A., Di Fabrizio, L., Di Mauro, M. P., Giacobbe, P., Granata, V., Harutyunyan, A., Knapic, C., Lattanzi, M., Leto, G., Lodato, G., Malavolta, L., Marzari, F., Molinaro, M., Nardiello, D., Pedani, M., Prisinzano, L., and Turrini, D., “The gaps programme with harps-n at tng - i. observations of the rossiter-mclaughlin effect and characterisation of the transiting system qatar-1,” *Astronomy and Astrophysics*, vol. 554, p. A28, Jun. 2013. [Online]. Available: <https://doi.org/10.1051/0004-6361/201321298>
- [16] R. Fares, J. F. Donati, C. Moutou, M. M. Jardine, J. M. Grießmeier, P. Zarka, E. L. Shkolnik, D. Bohlender, C. Catala, and A. Collier Cameron, “Searching for star-planet interactions within the magnetosphere of HD189733,” *Monthly Notices of the Royal*

- Astronomical Society*, vol. 406, no. 1, pp. 409–419, Jul. 2010. [Online]. Available: <https://doi.org/10.1111/j.1365-2966.2010.16715.x>
- [17] Czesla, S., Klocová, T., Khalafinejad, S., Wolter, U., and Schmitt, J. H. M. M., “The center-to-limb variation across the fraunhofer lines of hd 189733 - sampling the stellar spectrum using a transiting planet,” *Astronomy and Astrophysics*, vol. 582, p. A51, Oct. 2015. [Online]. Available: <https://doi.org/10.1051/0004-6361/201526386>
- [18] Bourrier, V., Zapatero Osorio, M. R., Allart, R., Attia, O., Cretignier, M., Dumusque, X., Lovis, C., Adibekyan, V., Borsa, F., Figueira, P., Hernández, J. I. González, Mehner, A., Santos, N. C., Schmidt, T., Seidel, J. V., Sozzetti, A., Alibert, Y., Casasayas-Barris, N., Ehrenreich, D., Lo Curto, G., Martins, C. J. A. P., Di Marcantonio, P., Mégevand, D., Nunes, N. J., Palle, E., Poretti, E., and Sousa, S. G., “The polar orbit of the warm neptune gj 436b seen with vlt/espresso,” *Astronomy and Astrophysics*, vol. 663, p. A160, Jul. 2022. [Online]. Available: <https://doi.org/10.1051/0004-6361/202142559>
- [19] V. Bourrier, O. Attia, M. Mallonn, A. Marret, M. Lendl, P. C. König, A. Krenn, M. Cretignier, R. Allart, G. Henry, E. Bryant, A. Leleu, L. Nielsen, G. Hebrard, N. Hara, D. Ehrenreich, J. Seidel, L. dos Santos, C. Lovis, D. Bayliss, H. M. Cegla, X. Dumusque, I. Boisse, A. Boucher, F. Bouchy, F. Pepe, B. Lavie, J. Rey Cerda, D. Ségransan, S. Udry, and T. Vrignaud, “DREAM. I. Orbital architecture orrery,” *Astronomy and Astrophysics*, vol. 669, p. A63, Jan. 2023. [Online]. Available: <https://doi.org/10.1051/0004-6361/202245004>

Ringraziamenti

Alla fine di questa Tesi, mi sembra doveroso dedicare uno spazio per ringraziare tutte le persone che, con il loro supporto, mi hanno aiutato in questo meraviglioso percorso di approfondimento delle conoscenze acquisite durante gli anni universitari.

Un sentito ringraziamento va al mio relatore, Luca Malavolta, che ha creduto in me, incoraggiandomi a non mollare nemmeno quando a pochi giorni dalla fine mi ero perso d'animo credendo che non ce l'avrei fatta. Grazie per avermi accompagnato lungo il percorso impegnativo di questa tesi, rendendosi sempre disponibile a chiarire ogni mio dubbio anche quando mi presentavo all'improvviso nel suo ufficio senza preavviso. Grazie per tutto il tempo che mi ha dedicato, rimandando persino i suoi impegni per dare la precedenza alla soluzione dei miei problemi, anche al costo di perderci intere giornate. Grazie davvero, perchè mi ha fatto appassionare ancora di più a questo mestiere.

Non posso non ringraziare le due persone che hanno avuto più influenza nel mio percorso educativo: i miei genitori. Mamma e papà: grazie per avermi permesso di inseguire il mio sogno, dandomi la possibilità di studiare senza mai chiedere nulla in cambio e senza farmi pesare gli anni dedicati al raggiungimento del mio obiettivo.

Grazie al mio amico di sempre Mirco con la M, (perchè se lo scrivi con la C diventa Circo), per le serate passate in allegria anche durante i momenti più difficili di questi anni di università.

Ringrazio Edoardo, per gli innumerevoli consigli ed il preziosissimo aiuto che mi ha dato con Python.

Un ringraziamento speciale ad Emma, la mia Luce, per essere stata stata sempre al mio fianco in questi mesi supportandomi e sopportandomi anche nei momenti più difficili.

Ringrazio infine i miei cari compagni di corso, Caterina, Caregnato e Cecilia, (CCC), per tutto il tempo passato insieme.

Grazie a voi conserverò un bellissimo ricordo di questi anni di università.